# THE EFFECT OF FATIGUE LOADING ON ELECTRICAL IMPEDANCE IN OPEN-HOLE CARBON NANOFIBER-MODIFIED GLASS FIBER/EPOXY COMPOSITES

by

**Ishan Tanay Karnik**

**A Thesis**

*Submitted to the Faculty of Purdue University*
*In Partial Fulfillment of the Requirements for the degree of*

**Master of Science in Aeronautics and Astronautics**

School of Aeronautics & Astronautics

West Lafayette, Indiana

May 2020

# THE PURDUE UNIVERSITY GRADUATE SCHOOL
# STATEMENT OF COMMITTEE APPROVAL

Dr. Tyler Tallman, Chair

    School of Aeronautics and Astronautics

Dr. R. Byron Pipes

    School of Aeronautics and Astronautics

Dr. Michael Sangid

    School of Aeronautics and Astronautics

**Approved by:**

    Dr. Gregory A. Blaisdell

        Head of the Graduate Program

*For my mom & dad*

# ACKNOWLEDGMENTS

First and foremost, I would like to express my deep and sincere gratitude to my thesis advisor, Dr. Tyler Tallman, for providing me with the opportunity to work in TNT laboratories at the School of Aeronautics and Astronautics at Purdue University developing new and exciting research in the novel work with composite conductivity as a means for health monitoring. I am honored I got to work with such an excellent and inspiring advisor. Thank you, Dr. Tallman.

Next, I would like to thank Dr. Christopher Gilpin of the Purdue Life Sciences department for his assistance in operating and obtaining the SEM images. I gratefully thank Dr. Gilpin for his help in obtaining these microstructure images of my test specimens.

Additionally, I would like to thank Dr. Harry H. Hilton from my undergraduate career at the University of Illinois at Urbana-Champaign. For encouraging me to go to graduate school and fostering my interest in aerospace structures and materials, thank you, Dr. Hilton.

Furthermore, I would like to thank Dr. R. Byron Pipes and Dr. Kaushik Roy for helping me out in my first year at Purdue University. With research and general graduate school direction, I was at a loss trying to navigate higher education. Finding my path would have been impossible without their help, and so for that, I thank you, Dr. Pipes and Dr. Roy.

Finally, I would like to thank my parents for being such excellent and accomplished role models, encouraging me to find my own path. I couldn't have done it without your love and support. Thank you.

# TABLE OF CONTENTS

# LIST OF FIGURES

# LIST OF TABLES

# LIST OF ABBREVIATIONS

| | |
|---|---|
| **AC** | alternating current |
| **AE** | acoustic emission |
| **CB** | carbon black |
| **CNF** | carbon nanofiber |
| **CNT** | carbon nanotube |
| **DC** | direct current |
| **EIS** | electrical impedance spectroscopy |
| **FBG** | fiber Bragg gratings |
| **FRC** | fiber reinforced composite |
| **GF** | glass fiber |
| **GFRC** | glass fiber reinforced composite |
| **MWCNT** | multi walled carbon nanotube |
| **PWAS** | piezoelectric wafer active sensors |
| **SHM** | structural health monitoring |
| **SEM** | scanning electron microscope |
| **UTS** | ultimate tensile strength |

# ABSTRACT

Author: Karnik, Ishan. MSAAE
Institution: Purdue University
Degree Received: May 2020
Title: The Effect of Fatigue Loading on Electrical Impedance in Open-Hole Carbon Nanofiber-Modified Glass Fiber/Epoxy Composites.
Committee Chair: Tyler Tallman

Fiber-reinforced composite (FRC) materials are ideal for the aerospace and automotive industries which require high-strength structures with exceptional specific properties. The unfortunate reality is composite materials are susceptible to complex failure modes and difficult-to-predict damage growth as a result of their heterogeneity and anisotropy. Thus, robust structural health monitoring (SHM) for in-operation tracking of damage formation and accumulation is important for these materials. Self-sensing materials are a strong candidate to replace traditional composite SHM because they do not suffer from the disadvantages of point-based sensing. The piezoresistive effect in nanofiller-modified materials is a common approach to material self-sensing. Research to date in piezoresistivity has predominantly focused on the direct current (DC) response of such materials. This is an important limitation because alternating current (AC) has important advantages – it inherently possesses more information (AC data can relate both impedance magnitude and phase to damage), AC effects can be leveraged for improved damage sensitivity, and AC interrogation can reduce power requirements. Therefore, to develop knowledge that will facilitate the transition to AC, this work explores the effect of high-cycle fatigue loading on the AC response of carbon nanofiber (CNF)-modified glass fiber/epoxy laminates. In this study, impedance magnitude and phase angle are measured along the length and through the thickness of composite specimens with an open-hole stress concentration subjected to tension fatigue-loading up to 10 MHz. The collected impedance data is fit to an equivalent circuit model as a function of cycle. These results show that high-cycle fatigue loading does indeed have an appreciable effect on the equivalent circuit behavior of the material. However, clear and definitive trends were not observed thereby suggesting that further research is needed into the basic mechanisms of AC transport in nanocomposites if frequency-dependent transport is to be used to track fatigue loading.

# 1. INTRODUCTION AND MOTIVATION

## 1.1 Introduction to Composite Materials

Fiber-reinforced composite (FRC) materials are widely used in the automotive and aerospace industries for high-performance structures due to their high specific properties. The increasing usage of composites over the past few decades in aerospace can be noted in Figure 1.1.
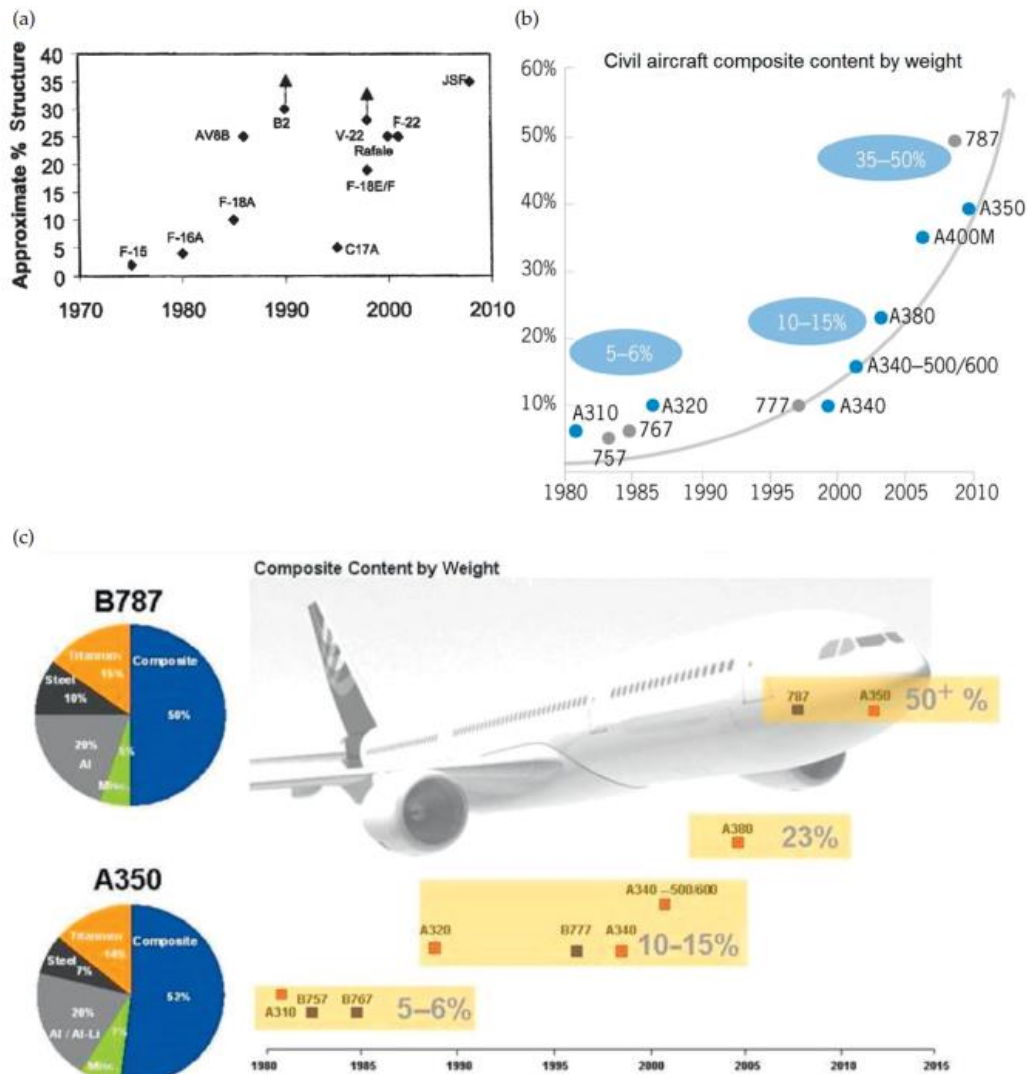


**Figure 1.1:** The increasing usage of composite materials in aircraft structures over the past 50 years. This figure (a) references military usage of composites, (b) demonstrates civil aircraft usage, and (c) shows how industry-leading Boeing and Airbus have been making use of composite materials more and more in their aircraft [1].

Composites are made by combining a reinforcing fiber with a matrix material. The properties of a composite material depend on its constituents. The reinforcing fibers come as either long continuous fibers or short fibers. Common reinforcing fibers include boron fibers, carbon fibers, glass fibers (GFs), and aramid fibers. Boron and carbon fibers offer excellent stiffness and strength while glass and aramid fibers offer high strength with moderate stiffness. Matrix materials are categorized as polymers, ceramics, or metals. There are numerous polymer resins used providing a broad range of properties; these include polyesters, polyimides, thermoplastic polymers, and thermoset resins. Metals and ceramics are typically used for high temperature application composites; they are difficult to process and expensive to make [2].

FRCs are ideal for industrial applications because of the advantages they provide in designer materials, where their desirable material properties (e.g. high strength-to-weight ratio, good tensile strength, and fatigue resistance) benefit the automotive and aerospace industries greatly. These high-performance materials have been used more prominently over the past several decades for these reasons [1]. Composite materials offer plenty of advantages, but their physical and mechanical properties are unlike standard homogenous and isotropic materials (e.g. metals). These materials require special consideration for their nonhomogeneous and anisotropic (generally orthotropic) material characteristics [3]. Their inherent heterogeneity with a fiber phase and matrix phase makes them susceptible to difficult-to-predict damage development and complex failure modes. Damage progresses in composite materials in several ways: matrix cracking, fiber breakage, fiber-matrix debonding, and delamination. The detection of damage can be difficult because much of the damage develops internally in the material and is not outwardly visible; addressing the progression of fatigue damage in FRC materials is an important gap in composite research [4].

Glass fiber reinforced composites (GFRCs) have been studied for a long time; research began as early as the 1940s [3]. Compared to carbon fibers, GFs offer a greater amount of flexibility (providing a higher ultimate strength) and lower cost [5]. The most popular GFs are E-glass (alumninoborosilicate) and S-glass (magnesium aluminosilicate). Typical GF diameters range from 3 to 20 μm. Epoxy resins are generally used as the matrix phase due to their compatibility with all types of fibers [2].

## 1.2    Composite Fatigue

This discussion on FRC fatigue in this thesis is intentionally limited in scope because this work does not delve into how the fatigue damage development occurs. Rather, a brief overview is given to motivate the need for monitoring fatigue-induced damage. Composite materials fatigue as a result of operational loads and environmental factors leading to a general depreciation in strength characteristics. This is a gradual loss in material properties, e.g. stiffness.

FRCs tend to be resistant to through-thickness cracks as the primary damage initiation happens between the laminae interfaces. Cracks can initiate due to fabrication imperfections and propagate as a result of cyclic fatigue loading during normal operation [1]. Crack formation in composites occurs in a variety of forms: in fibers in the axial directions, matrix cracking develops in off-axis plies and external surfaces, as well as local delaminations between plies [6]. In metals, a crack forms then rapidly grows leading to final fracture; in composites microcracks, even visible cracks, grow in ways to relieve stress concentrations on the fibers. They occur throughout the volume of the material, weakening plies, resulting in a decreasing elastic modulus [7]. The typical forms of damage mechanisms in FRCs are delamination, fiber-matrix debonding [4],  fiber breakage, matrix cracking, interfacial shear failure [8], and their interactions. Characterizing fatigue development is crucial to composite structural analysis.
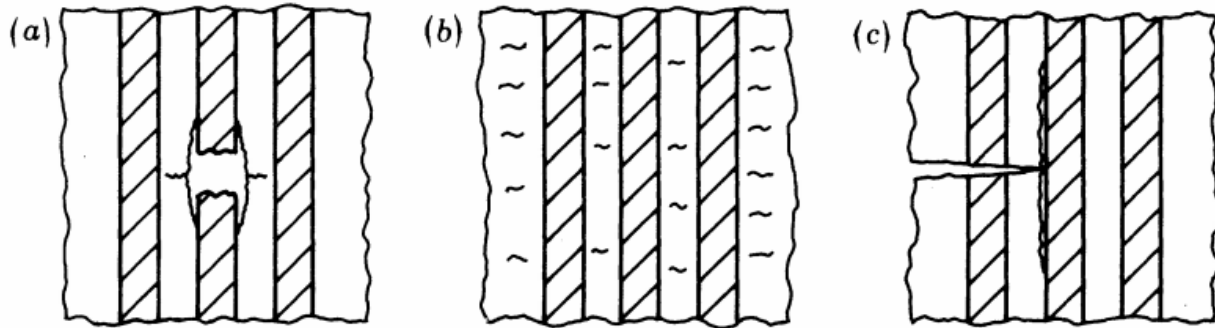


**Figure 1.2:** Fatigue damage mechanisms with the load applied parallel to fibers. This damage develops as (a) fiber breakage (interfacial debonding), (b) matrix cracking, and/or (c) interfacial shear failure [8].

Cyclic fatigue results from repeated loading of a structure. When a structural member is subjected to its standard operating load cycle, the tensile and compressive loads cause the

member to lose strength [4]. As a result of these load cycles, microcracks form in the structure, often in multiple locations. These microcracks are not capable of causing fracture, however, with the repeated cycling these cracks coalesce into more dominant cracks which then grow stably. Once a dominant crack reaches an upper limit, fracture occurs. The fatigue process consists of three steps: crack nucleation, crack growth, and final fracture [9]. A general schematic of this process can be noted in Figure 1.3.
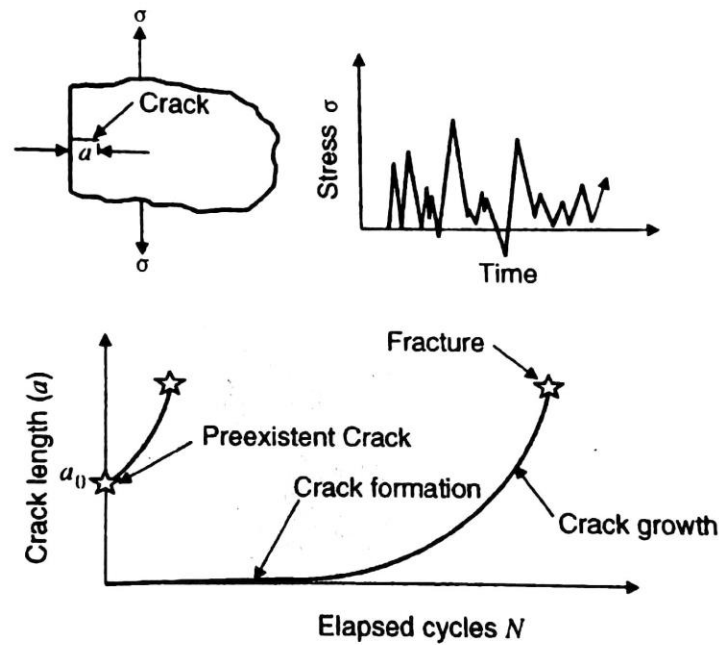


**Figure 1.3:** Fatigue failure mechanisms demonstrating how cracks form and propagate as a result of cyclic loading [9].

Cracks can initiate as a result of transverse ply cracks, splitting in the load direction, delamination, or fiber breaks. Depending on intrinsic brittle natures of fibers and manufacturing variability different parameters affect crack nucleation [10]. Crack propagation in composite laminates typically occurs in between plies. The propagation is therefore affected by fracture processes and propagates in one of the three modes of fracture: the opening, sliding, or tearing mode [3]. The damage development process in FRCs consists of initiation and growth via different fracture modes and complex interactions. The modes are limited to the three, but their effects and long-term behavior depend on material, load, geometry, and environment [4]. Different types of damage interactions related to the percent of life can be noted in Figure 1.4.
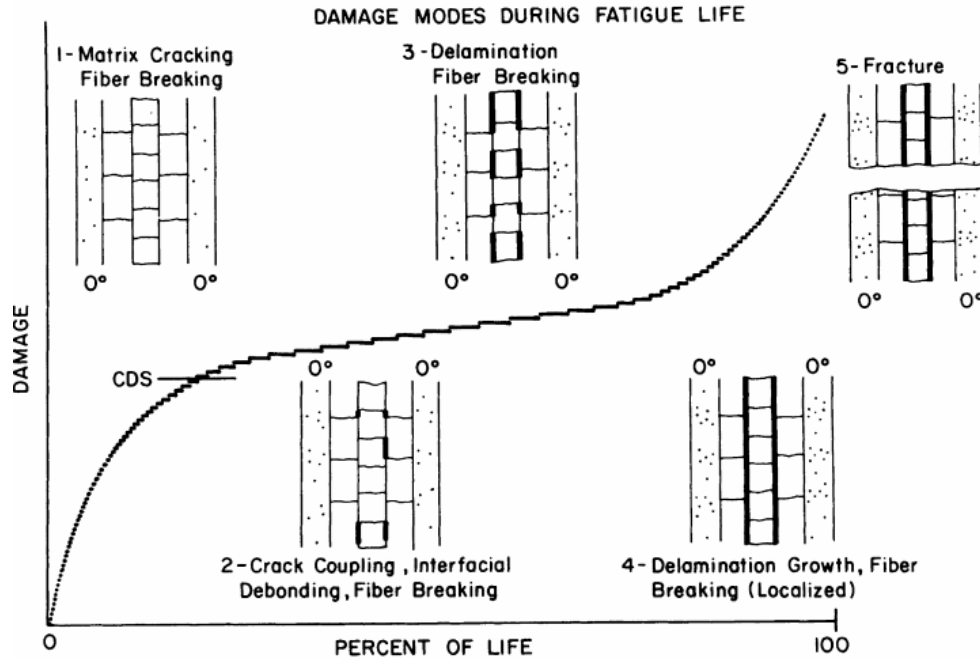
**Figure 1.4:** The matrix and fiber damage modes related to the lifetime of a FRC material [4].

The number of fatigue cycles that lead to failure varies. Fatigue failure depends on the amplitude and mean value of the load, sequence of load application, specimen geometry, and inherent material properties. Other aspects that affect maximum cycles of a specimen are the condition of the surface; rough surfaces, notches, and material impurities change how cracks propagate. Residual stresses in a structure also significantly affect fatigue life. Furthermore, environmental factors play a role in fatigue where things like salt water, moisture, temperature, frequency, and shape of the load cycle all have an impact. Fatigue is a function of small cyclic loads dependent on many parameters, it is important to design for structural fatigue. General design considerations for fatigue are to select proper materials, set low load levels, provide multiple load paths, and regular rigorous inspection [9].

In tension, fatigue interlaminar cracking is generally the first form of damage. This damage extends through the thickness of the plies parallel to fibers within a ply. This form of fracture is not critical in terms of the final fracture; however, it contributes to reducing stiffness and loss in transverse strength [10]. Cyclic loading in FRCs has shown to result in debonding between fiber and matrix interfaces which leads to the initiation of transverse ply cracks [11]. Some examples of cracks propagating in the form of ply cracks and delaminations can be noted in Figure 1.5.
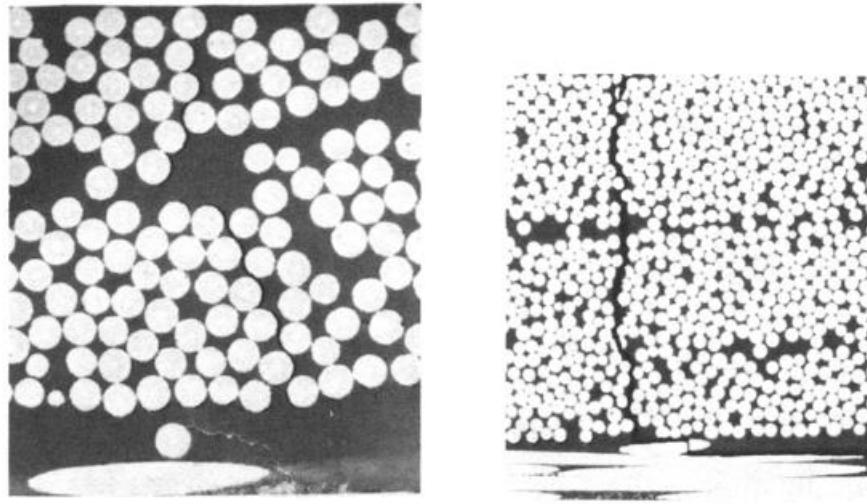
**Figure 1.5:** These images show fatigue crack propagation in FRCs. The image on the left shows a transverse ply crack while the image on the right shows delamination occurring at the intersection of a transverse ply crack and a longitudinal ply in a cross-ply FRC [11].

In fatigue crack growth studies, a constant-amplitude load cycle does not have a thickness dependency (variable stress amplitude applications do have a thickness dependency). Fatigue crack growth nucleates at material imperfections or in high-stress areas. Microcracks are short cracks (length-wise) and physically small. These microcracks nucleate in imperfection regions and tend to propagate independently until adjacent microcracks come near enough to coalesce and produce dominant cracks. These dominant cracks control the final failure. Microcracks grow at rates that exceed those of large cracks tested at similar stress concentration levels [9]. In general, fatigue-life is defined by the lowest fatigue performing material. What this means is that the presence of a transverse fiber severely reduces the performance as the dominant mechanism becomes matrix cracking along these fibers; the limiting aspect of composites is set by the matrix properties [8].

The benefit of including a stress concentration in experimental fatigue testing is that where the material will fail is set. The crack growth is still subject to fatigue criteria, but the presence of the stress concentration establishes the nucleation point. In an open-hole plate, the stress concentration factor for an isotropic material is 3. For orthotropic unidirectional composites, the stress concentration goes up to 9. Plates, where the width and length exceed six-hole diameters,

can be modeled as infinite [3]. Strength reduction can occur sufficiently far away from the hole as a result of widespread matrix cracking, delamination, and irregular fracture modes throughout the plies [4].
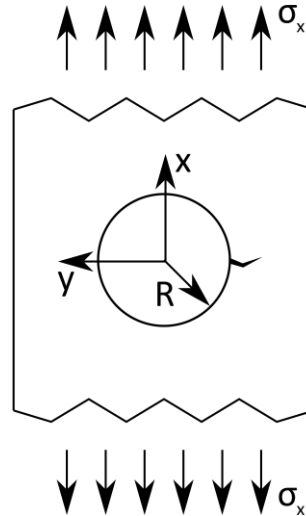


**Figure 1.6:** Crack nucleation can be noted forming on the right side of the hole, at point $(0, -R)$ in Cartesian coordinates. Open-hole stress concentrations range from 3 to 9 and therefore establish the nucleation point of the crack.

Open-hole FRCs under tension fatigue cracks nucleate in the form of branches at either vertex opposite the load direction. These branches do not initiate or propagate concurrently. However, by fracture, the total length of the split branches on either side of the notch is approximately the same [12]. The different forms of these branches can be noted in Figure 1.7.
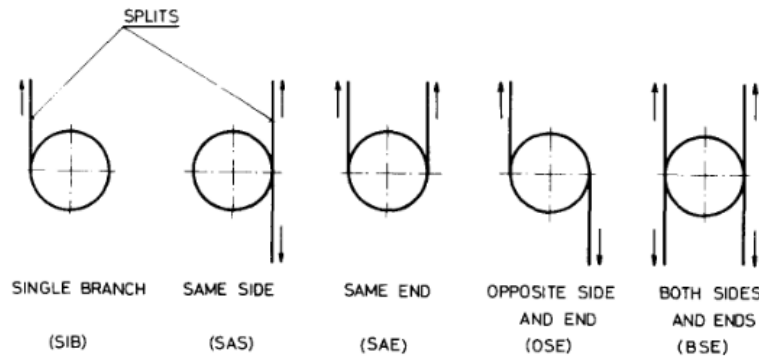


**Figure 1.7:** The different modes of splitting initiation of FRCs subjected to tension fatigue [12].

## 1.3    Structural Health Monitoring

The previous discussion establishes the complexity of composite fatigue. In light of this complexity, there is a need for integrated sensing of damage formation. Structural health monitoring (SHM) is a method of continuous structural integrity monitoring; as damage develops, SHM sensors alert crack propagation (or other forms of damage) is underway [1]. SHM enables real-time monitoring, inspection, and damage detection [13]. There are four characteristics of health monitoring: operational and environmental loads, mechanical damage caused by loading, damage growth, and future performance as a result of damage accumulation [14]. The process involves permanent, continuous, periodic, or periodically continuous recording of structural performance parameters. Commonly monitored parameters include strain, deformation, acceleration, acoustic emissions (AEs), displacement, crack opening, stress, load, temperature, and humidity [15].

Composite materials are less susceptible to catastrophic failure due to fatigue compared to their metallic counterparts. Monitoring how fatigue develops in these heterogeneous, anisotropic materials is important for extending the lifetime of FRC structures. Traditional SHM systems for composite materials come as sensor arrays which are applied externally or internally in a structural body [1]. SHM sensor arrays are permanently placed on the structure for lifetime health monitoring in either a passive (e.g. strain gages) or active manner (e.g. piezoelectric transducers) [16]. An ideal sensor is one that is cost-effective, lightweight, and does not substantially add to cost nor incur significant weight penalties. Depending on where the sensor is placed, it operates in either static or dynamic regions of the physical structure [1]. These sensors come in many forms: piezoelectric transducers, fiber-optic sensors, traditional strain gages, etc. Fatigue sensitive zones, regions where SHM sensors should be placed, are interfaces between composite and adhesives, the surface matrix resin of the composite, and the near-surface plies of the FRC [17].

### 1.3.1    Piezoelectric Transducers

A common method of composite SHM is using piezoelectric wafer active sensors (PWAS). PWAS can be both active sensors and passive sensors. PWAS transducers are made up of piezoceramic wafers which are thin electrically poled materials. Active PWAS use guided Lamb

waves similar to ultrasonic transducers. Passive PWAS monitor AE and detect impact [1]. PWAS couple mechanical and electrical effects (i.e. strain, stress, electrical field, and electrical displacement) through the piezoelectric constitutive relation. To investigate thin-wall structures, PWAS use guided-wave particle motion on the material surface using an in-plane oscillatory voltage through piezoelectric coupling. In the case that PWAS are used as ultrasonic transducers, PWAS use through surface pinching. This 'pinching' registers through strain coupling with the structural surface allowing more efficient transmitting and receiving of guided waves relative to traditional ultrasonic transducers; ultrasonic transducers apply structural vibration through pressure [16].

Four different methods of propagating waves in a thin-wall structure can be noted in Figure 1.8. First, consider the pitch-catch method which is when an electric signal is applied at the transmitter PWAS. This signal is applied via piezoelectric transduction. This elastic wave moves through the structure and is captured by a receiving PWAS. These elastic waves are guided Lamb waves. If the structure is pristine, the received signal will be the same as before; if the structure contains damage the received signal will be altered. Pitch-catch can be used to detect degradation in composites. Next, consider the pulse-echo method, another guided Lamb wave. This method involves a PWAS acting as both the transmitting and receiving transducer. A tone-burst signal applied to the PWAS results in an elastic wave that travels through the structure and reflects at structural boundaries, cracks, and discontinuities. A pristine structure only has reflections at boundaries whereas damage is indicated by different reflections. Another method is the thickness mode. A PWAS transducers thickness mode is excited at higher frequencies than guided Lamb waves, e.g. for a 0.2 mm PWAS the thickness mode operates at 12 MHz whereas the guided-wave modes operate at around 100 kHz. The PWAS transducer operates as a thickness gauge, detecting subsurface damage in the form of cracks parallel to the surface, like delaminations. However, this method suffers from limited proximity as the damage has to be directly present below the PWAS. Finally, PWAS transducers can operate passively receiving elastic waves generated through impacts and by AEs. Placing several PWAS transducers in a network configuration allows a distributed listening system to monitor the development of such damage. The PWAS is self-energized as a result of piezoelectric transduction, so this method can

stay in a dormant and low-energy mode only waking up as a result of these events. Processing the signal can yield the location and amplitude of the impact and/or AE event [16].
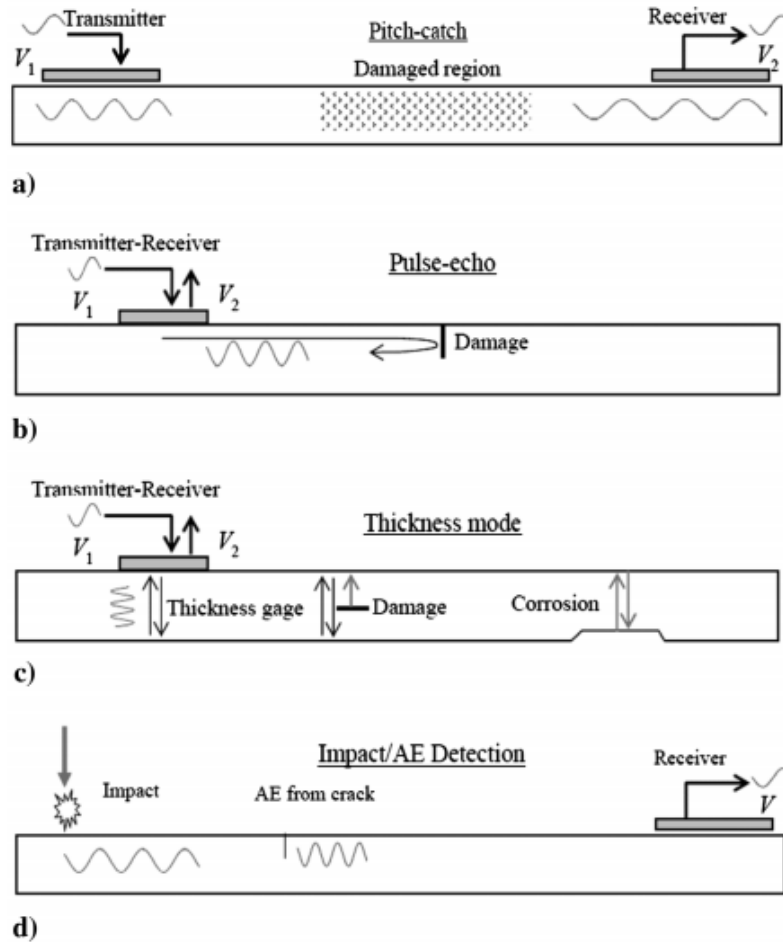


**Figure 1.8:** Propagating waves using PWAS for damage detection in a thin-wall structure. The (a) pitch-catch method, (b) pulse-echo method, (c) thickness mode, and (d) impact/AE detection method can be noted [16].

PWAS typically come as 7 mm squares with a 0.2 mm thickness. PWAS have been used as array networks to detect internal damage in composite materials. In some research, PWAS have been inserted experimentally between composite laminate layers; however, this resulted in structural integrity issues. PWAS materials have successfully been inserted as a layer to passively and actively diagnose damage development in composite materials. One such SMART insertion can be noted in Figure 1.9. The term "SMART" stands for "Stanford Multi-Actuator Receiver Transduction" and is a form of a PWAS resembling a lamina [1].
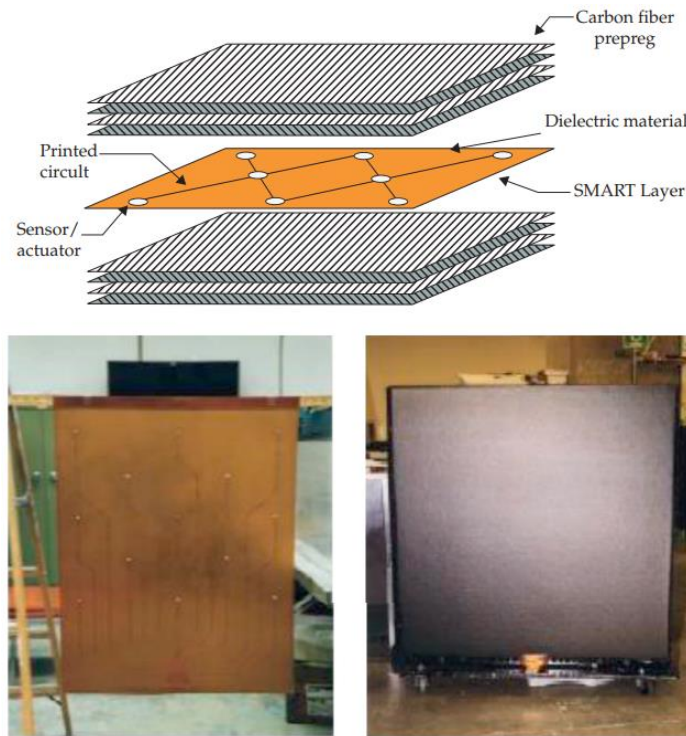
**Figure 1.9:** A 36" × 30" composite laminate with an embedded SMART layer between carbon fiber prepreg layers [1].

PWAS benefit from the direct conversion of electric energy into elastic energy and vice versa. This method has demonstrated its ability to measure a great deal of data in research using only a signal generator, oscilloscope, and a PC, speaking to its simplicity. Effective measurements of impact waves and guided-waves through transmission and reception have been achieved using PWAS as sensor arrays speaking to their robustness for composite SHM. These sensors are used because they are lightweight, inexpensive, and easy to use [1]. PWAS studies have shown a great many benefits to this SHM, however, they do suffer from some key limitations. PWAS need to be firmly coupled to the material to be effective in noting damage. In FRCs, the anisotropy of the material plays a heavy role in the PWAS detection abilities as, for example in one study, the PWAS was able to say there was damage present but unable to identify the type of damage and location through the thickness [18]. In general, PWAS sensor arrays need to be very dense to achieve good sensitivity and localization. One study found that the number of PWAS sensors needed on a 737NG fuselage would incur such a weight penalty (and therefore payload penalty) that the financial cost of the SHM system was an order of magnitude greater than savings provided by continuous inspection [19].

### 1.3.2   Fiber-Optic Sensors

Another common methodology for composite SHM is fiber-optic sensing. Fiber-optic sensors come in three forms: point sensors, long-gauge sensors, and distributed sensors. Point sensors include Fabry-Perot interferometers and fiber Bragg gratings (FBG). Long-gauge sensors consist of SOFO interferometric sensors. Distributed sensors include Raman scattering and Brillouin scattering sensors [15].

Fiber-optic sensors utilize internal reflection in an optical fiber to monitor structural changes [1]. This basic premise is described in Figure 1.10. A common method for optical FRC SHM is FBG. A FBG resides in the core of an optical fiber, extending over a limited length. FBGs are permanent, periodic perturbations of a refractive index exposed along the length of the fiber. This periodic structure acts as a filter for light traveling along the fiber, where the reflecting light as a predetermined range of wavelengths is centered on a peak wavelength value. The basic geometry and premise of FBG sensors can be noted in Figure 1.11. External forces like strain, pressure, and temperature change the grating period and effective refractive index. These are high-resolution systems with high absolute accuracy [20].
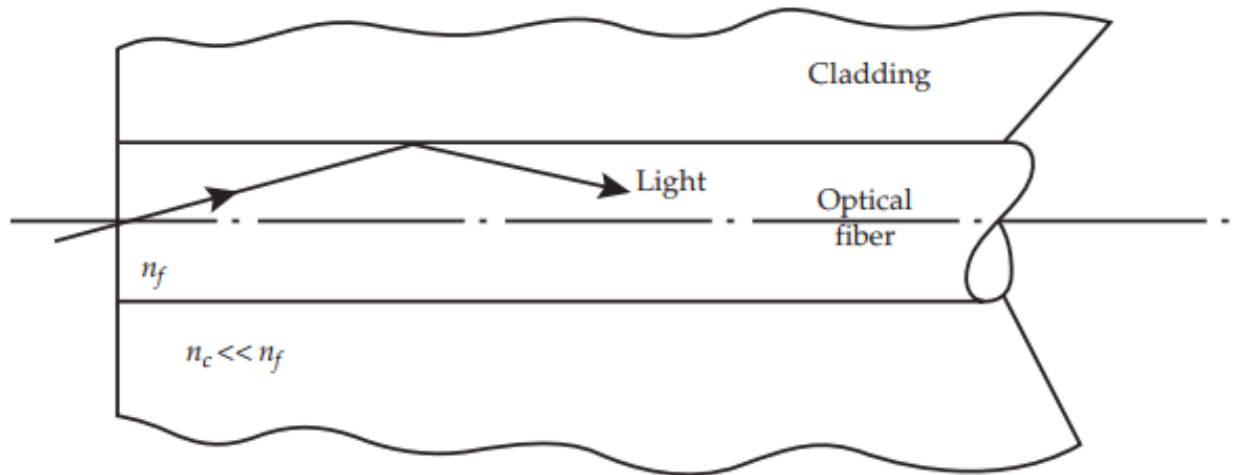


**Figure 1.10:** Light guiding properties of optical fibers. These phenomena are a result of total internal reflection between cladding and core refractive indices where $n_{\text{cladding}} < n_{\text{medium}} < n_{\text{core}}$ [1].
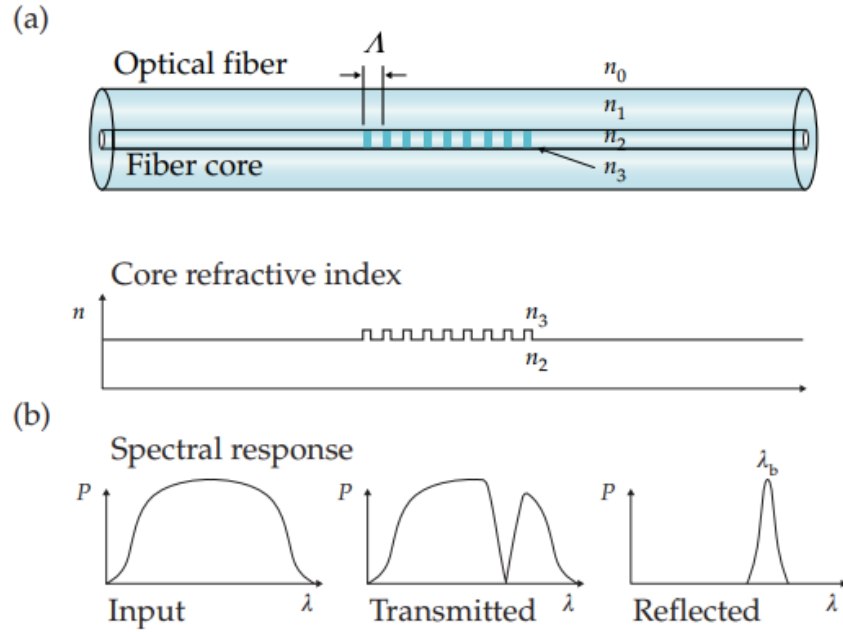
**Figure 1.11:** FBG optical sensors are described here. The basic (a) principles of an FBG can be noted as well as the (b) details showing how the notch affects transmission and reflection [1].

Fiber-optic sensors can be embedded into the composite laminate similar to PWAS layers. Instead of representing laminae, they are embedded into the fiber phase. A representative image of this can be noted in Figure 1.12, where the large fibers in the center of the image are the fiber-optic sensors.



Optical fiber at 0° to carbon fiber          Optical fiber at 30° to carbon fiber
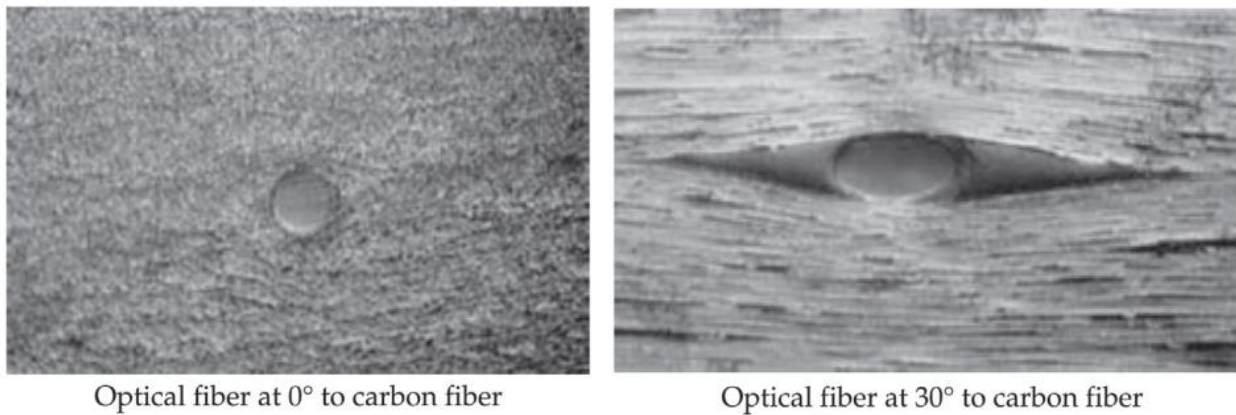
**Figure 1.12:** Embedded fiber-optic sensors in composite laminates in the fiber-reinforcing alignment direction as well as $30^o$ to the fiber direction [1]. The right image shows a considerable stress concentration due to the off-axis alignment of the fiber-optic sensor.

Fiber-optic SHM provides numerous advantages. This method of SHM is unaffected by electromagnetic interference, resistant to corrosion, multiplexable, as well as their ability to be directly embedded in the fiber phase of the composite material. Fiber embedding is a cautious advantage because a typical optical fiber diameter falls in the range of 120 to 250 μm whereas E-glass fibers fall in the range of 3 to 20 μm. This discrepancy results in discontinuities, presenting stress concentrations in the material [1]. They are very accurate and highly reliable SHM systems. However, fiber-optic sensors tend to be very expensive and delicate – they are easily damaged. Further, they require a power source as light needs to be run through the fiber [14]. Lastly, fiber-optic sensors require expensive optics-to-electronics converters thereby adding substantial cost to their use.

### 1.3.3   Conventional Strain Gages

Strain gages are widely used in experimental stress analysis for their simple application. Strain gages are discrete, point sensors classified as short-gauge sensors [15]. With a sufficient strain gage array, a strain gage closer to the damage shows a decrease in measured strain relative to one further away [17]. Strain gage arrays are applied to a variety of composite structures. A strain gage arrangement is composed of a wire (or foil), thin plastic, and electrical leads; a strain gages geometry can be noted in Figure 1.13.
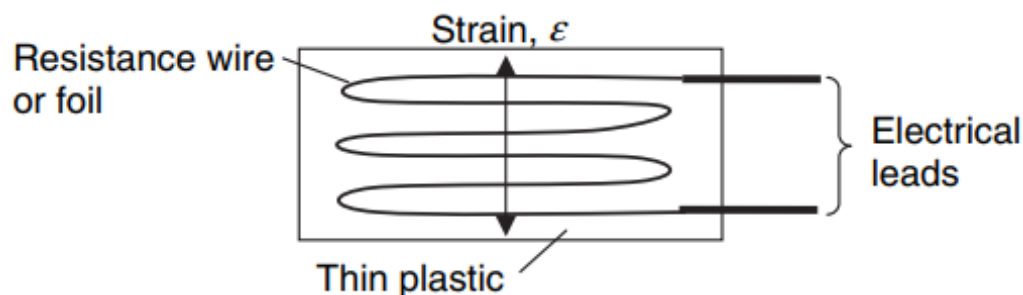


**Figure 1.13:** Strain gage geometry. Resistance changes between the electrical leads can be interpreted as strain changes via a Wheatstone bridge arrangement [14].

Strain gages make use of relative resistance changes in a Wheatstone bridge arrangement to characterize strain. This arrangement can be noted in Figure 1.14. The Wheatstone bridge operates by balancing the bridge to zero voltage among opposing nodes. An adjustable resistance is used to calibrate the bridge. Depending on how much adjustment is required to bring the

bridge to zero indicates how much strain has changed the resistance across the bridge. They operate in both direct current (DC) and alternating current (AC) modes – in AC the capacitive and inductive effects are negligible at low frequencies for strain gages [1]. Strain gages are very precise instruments. Strain gages are sensitive to both mechanical and electrical properties. This strain change can be a result of geometric changes (e.g. Poisson effects) or as a result of piezoresistive effects electrical materials exhibit [14]. Strain gages are sensitive to resistance changes from tensile forces and compressive forces. An array of strain gages at differing angles is needed as strain gages are insensitive to lateral forces. They operate well in both static and dynamic regions [1].
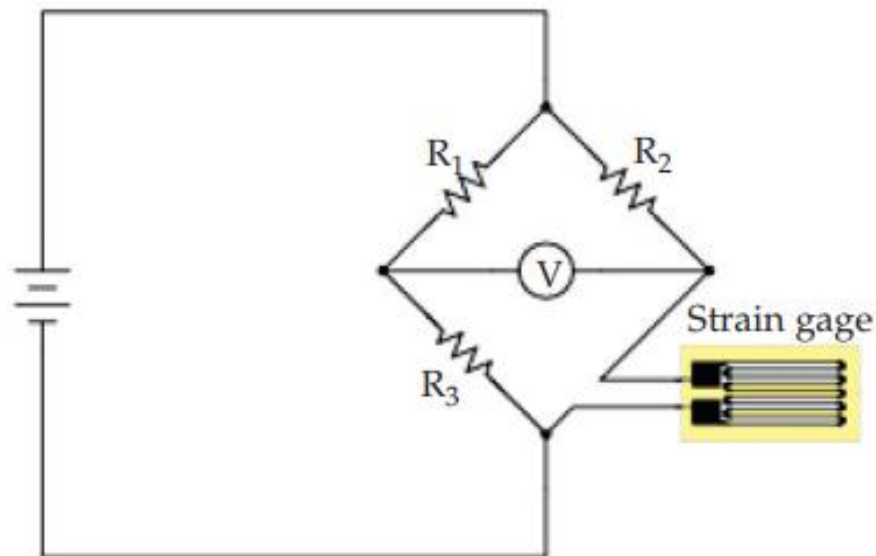


**Figure 1.14:** Quarter-bridge strain gage circuit in a Wheatstone bridge arrangement [1].

For composite materials, strain gages can be attached atop the structure but this requires good adhesion between the gage and composite material for adequate stress analysis. They can also be built into layers of the composite material. Strain gages need wires to run from the two ends to gather data. A special kind of strain gage has been developed for composite application where pins protrude through the material that can be trimmed and soldered creating external connection points for measurement [1]. This special composite material strain gage can be noted in Figure 1.15.
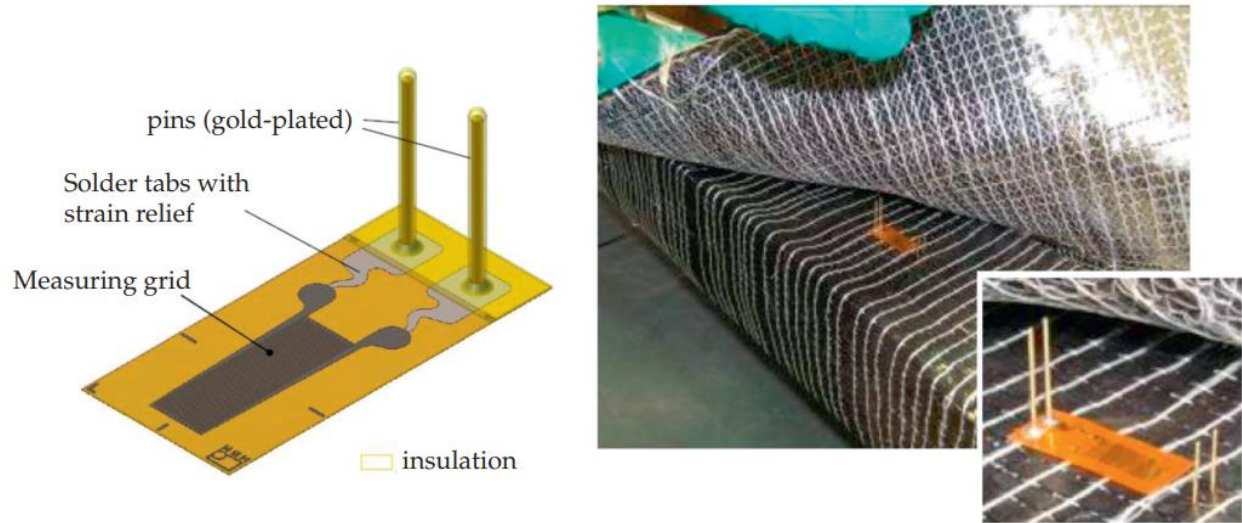
**Figure 1.15:** A special strain gage developed for FRC structures. In this strain gage, the pins (electrodes) protrude through the composite material and can be connected to external wires. An example of this sensor inserted can be noted on the right side of the figure [1].

Strain gages suffer from limited localization, providing only strain readings within a small elastic range on structural materials. Strain gages require wire connections, however, wireless instrumentation options are available [1]. Strain gages suffer from adhesion limitations. Strain gages with poor adhesion have demonstrated anomalous readings and therefore are limited in their benefits for SHM [17]. Strain gages and FBG sensors have shown good agreement in the experimentation of FRC structures [20] [21]. FBG have shown more durability and sensitivity than conventional foil strain gages and are therefore considered more suitable for FRC SHM [20].

# 2.  PIEZORESISTIVITY

With an introduction to composite materials and traditional SHM practices established, this section introduces a novel SHM method: SHM via self-sensing materials. Most often, self-sensing is achieved via the piezoresistive effect (i.e. having deformation and damage-dependent electrical conductivity). This section introduces piezoresistivity in carbon nanofiller modified composite materials, sometimes referred to as nanocomposites, via DC and AC.

## 2.1    An Alternative to Traditional FRC SHM – Piezoresistive Self-Sensing

The problems with the previously mentioned SHM methods can be summarized as: i) by placing a separate sensor onto the material these additional sensors weaken the material and serve as failure initiation sites; ii) sensors improperly adhered to a material provide anomalous data; iii) discrete or point-based sensors suffer from limited localization and damage sufficiently far away from sensors can go undetected. As an alternative, self-sensing materials utilize the *structure-as-a-sensor* concept by leveraging changes in an inherent property of the FRC as an indicator of damage. In piezoresistive materials, this property is electrical conductivity. This means that deformation and damage can be inferred continuously throughout the component via simple and easily multiplexed electrical measurements without the need for embedded sensors. Piezoresistivity is traditionally achieved in insulating materials such as GFRCs by modifying the polymer matrix with conductive nano-to-microscale fillers such as carbon nanotubes (CNTs) or carbon nanofibers (CNFs). An example of piezoresistive-based self-sensing can be noted in Figure 2.1. To use this method for SHM in practice, the integrated circuitry to use this methodology can be placed under a coating on the structure to minimize weight and potential aerodynamic impacts.
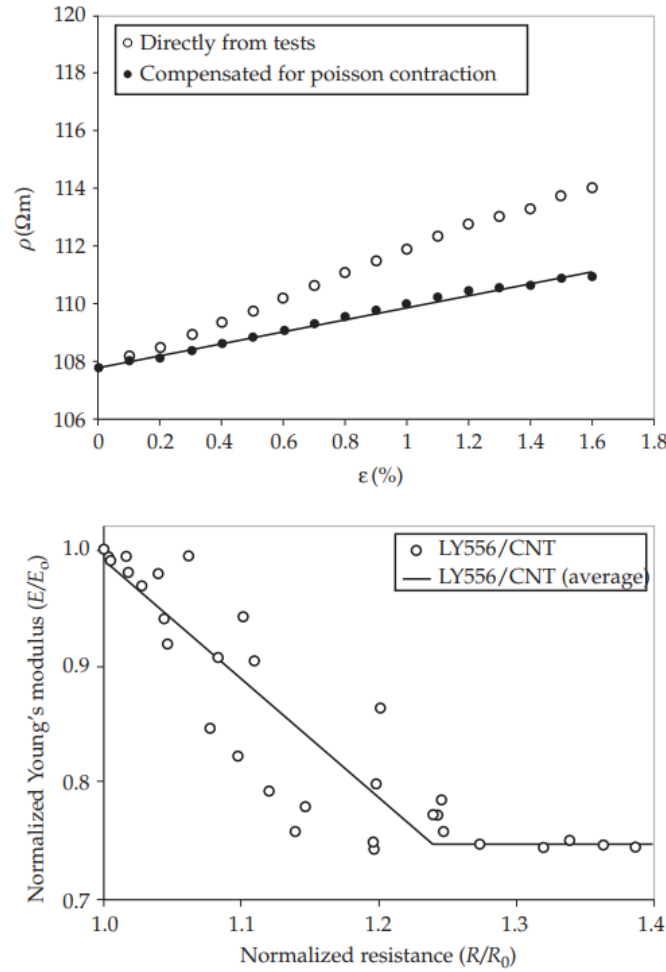
**Figure 2.1:** 0.5 wt.% CNT modification of a GFRC shows a change in resistivity related to strain changes in LY556/CNT. These plots include raw results and Poisson contraction compensated data. The resistance change was correlated to the elastic modulus (stiffness) reduction in the material [1].

### 2.1.1 Mechanism of Conductivity and Piezoresistivity in Nanocomposites

The piezoresistive effect is a relationship between the mechanical state and electrical resistivity. It is similar to the piezoelectric effect in that it relates electrical changes to mechanical stress; however, the key difference is that it relates mechanical changes to electrical resistance rather than electrical potential. Further, unlike piezoelectricity, piezoresistivity is a one-way form of electro-mechanical coupling; there is no reverse piezoresistive effect. Essentially, material deformation and damage result in electrical conductivity changes.

To fathom why nanocomposites are piezoresistive, we first  need an understanding of the mechanism by which these materials are conductive. In nanocomposites, nanofillers serve as the electrical pathways in the otherwise nonconductive GFRC material. That is, sufficiently many nanofillers need to be added to form a percolated or electrically well-connected network through the material. For this reason, ultra-high aspect ratio fillers such as CNTs and CNFs are commonly used because the percolation threshold decreases with increasing aspect ratio. State of the art examples include carbon black (CB) [22] [23] [24] [25] [26] [27], CNFs [24] [28] [29] [30], CNTs both single-walled and multi-walled (MWCNT) [23] [26] [27] [31] [32] [33] [34] [35] [36] [37] [38] [39] [40] [41] [42] [43] [44] [45] [46], as well as combinations of these nanofillers [23] [24] [26]. Piezoresistivity is, therefore, a consequence of either strain altering the connectedness of the nanofiller network or damage severing connections between nanofillers. A scanning electron microscope (SEM) image of a well-connected network of CNFs in a polyurethane matrix is shown in Figure 2.2.
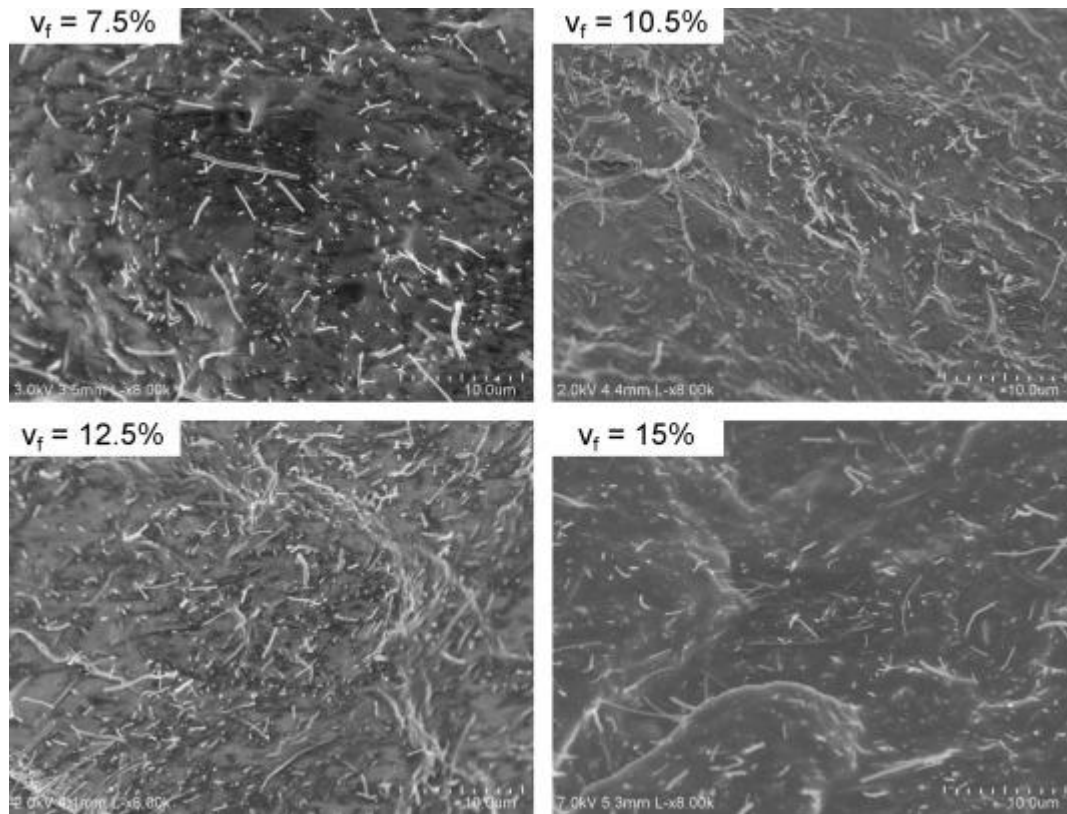


**Figure 2.2:** SEM images of a well-connected CNF network. Note that the pathways through the material are dependent on nanofiller volume fraction. In this figure there is 7.5%, 10.5%, 12.5% and 15% nanofiller volume fraction [29].

For DC transport, this nanofiller network can be envisioned as a collection of resistors belonging to the nanofillers themselves and inter-nanofiller resistors where electrons can quantum mechanically tunnel or jump between sufficiently proximate nanofillers (typically through separations on the order of 1-2 nm) as schematically illustrated in Figure 2.3. This quantum tunneling resistance is well-approximated by Simmon's formula given below in equation (2.1) [47] [48].
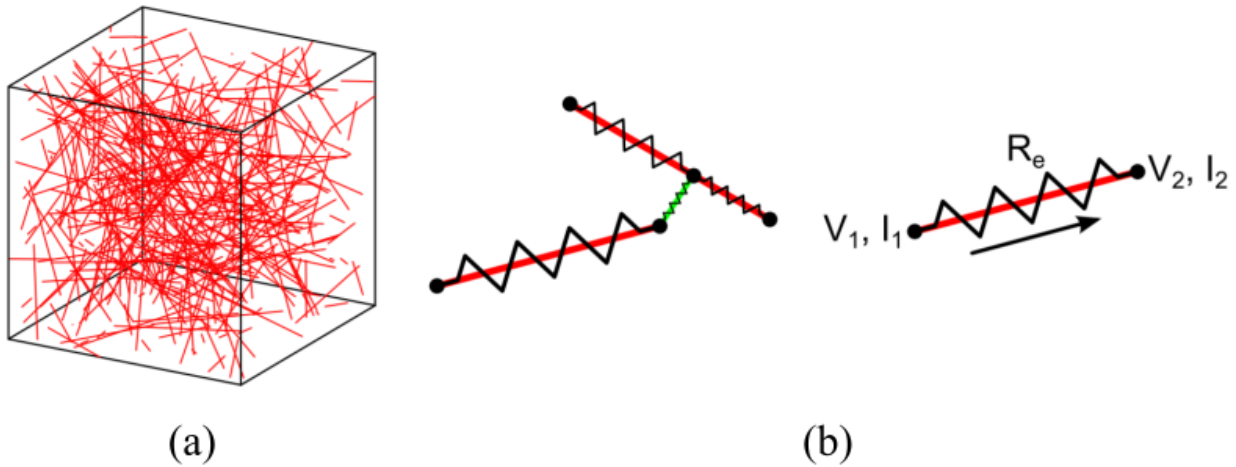


**Figure 2.3:** (a) A randomly distributed 0.4% CNT volume fraction network can be noted. (b) Schematic representation of nanofiller junctions (shown in red) discretized as resistor elements within a tunneling distance (shown in green). The current and voltage across a single nanofiller can be further noted [49].

$$R_{\text{tunnel}} = \frac{h^2 t}{Ae^2 \sqrt{2m\varphi}} \exp\left(\frac{4\pi t}{h}\sqrt{2m\varphi}\right) \qquad (2.1)$$

In this equation, $h$ is Planck's constant, $t$ is the inter-nanofiller distance, $A$ is the overlapping area between the nanofillers, $e$ is the charge of the electron, $m$ is the mass of the electron, and $\varphi$ is the potential barrier height between nanofillers. From this, we can also see that deformation alters the tunneling resistance between neighboring nanofillers thereby also contributing to the piezoresistive effect.

For AC transport, a well-connected network allows for different pathways through the material for imparted current to flow through; these paths range from resistive, capacitive, inductive, to

combinations of these elements [28] [38] [50]. Work done by Tallman and Hassan demonstrated that this network can likewise be discretized into linear circuit elements as shown in Figure 2.4 and Figure 2.5 [28] [50]. A similar analysis of the filler junctions established by Sanli et al. can be noted in Figure 2.6. Sanli et al. extended their description showing that under tensile strain the nanofiller network reorients changing the electrical pathway [38]. This can be noted in Figure 2.7. Again, any disruption in the form of deformation or severance of this well-connected network results in a change in the electrical pathways through the material and giving rise to AC piezoresistivity.
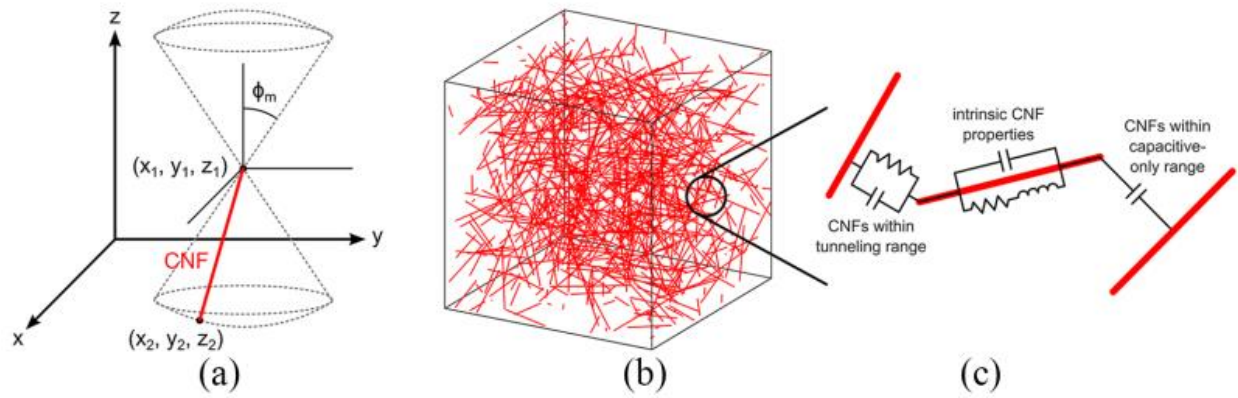


**Figure 2.4:** Modeling process of CNF distribution in nanocomposites. The (a) CNFs are randomly generated within the boundaries of two spherical cones. Then (b) the representative CNF network in a domain is established. The (c) inter-nanofiller junctions can be discretized as AC circuit elements [28].
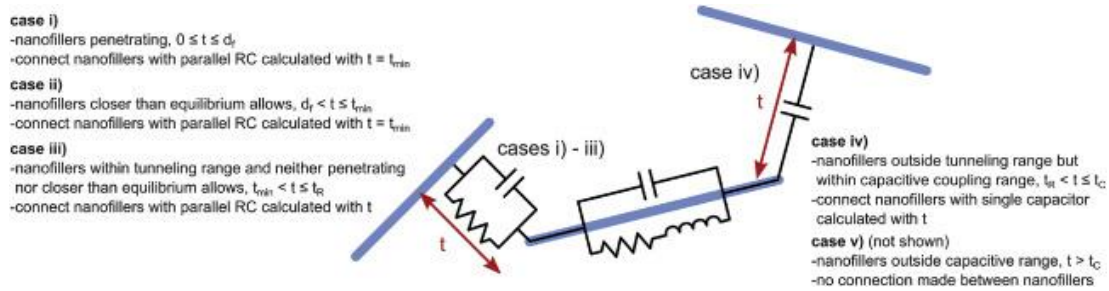


**Figure 2.5:** The different cases present in the inter-nanofiller junctions in a well-dispersed nanofiller modified polymer. Cases i) through iii) model nanofillers via standard electron tunneling represented as a parallel resistor-capacitor. In case iv), the nanofillers are too far apart for standard electron tunneling but are close enough for capacitive coupling between the nanofillers [50].
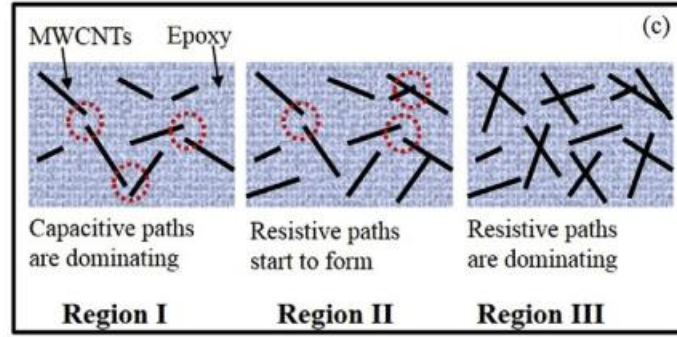
**Figure 2.6:** Formation of conductive pathways as a result of MWCNT proximity. The transport mechanism is heavily dependent on the concentration of MWCNT in that region [38].
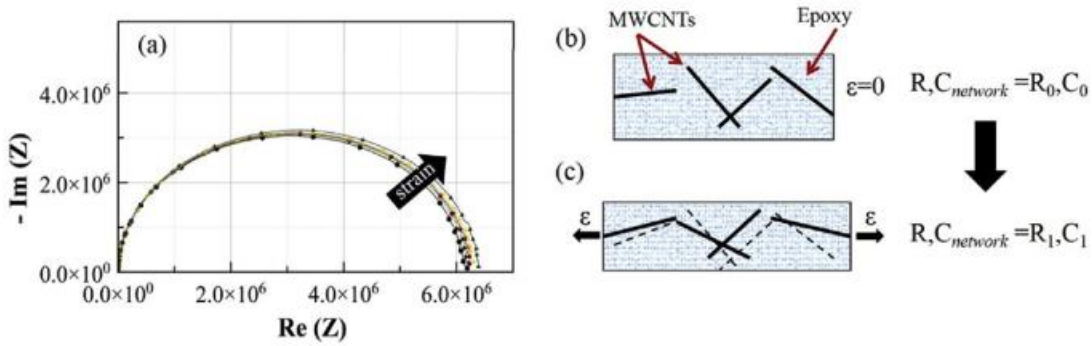


**Figure 2.7:** (a) Nyquist plot of MWCNT-modified epoxy nanocomposite. The equivalent circuit representations change from (b) unloaded state to the (c) tensile strain state [38].

### 2.1.2  Using the Piezoresistive Effect for FRC SHM

Having discussed the basic mechanisms of piezoresistivity, we next turn our attention to its application for SHM. To date, DC methods have been overwhelmingly utilized for piezoresistive SHM. Studies of nanofiller modifications have shown an increase in resistance as damage is imparted onto a specimen [24] [39] [40] [41] [51]. The DC response has also been monitored in low-cycle fatigue loading [39] [41] [52]. For example, Ku-Herrera et al. studied MWCNT-modified GFRC specimens. Their study investigated the effects of quasi-static tension up to failure, where they monitored AE and DC resistance change as compared to strain readings. Ku-Herrera et al. showed that resistance changes can be correlated to AE testing but do not provide a detailed response to nanofiller network change [40]. A plot from their work can be noted in Figure 2.8.
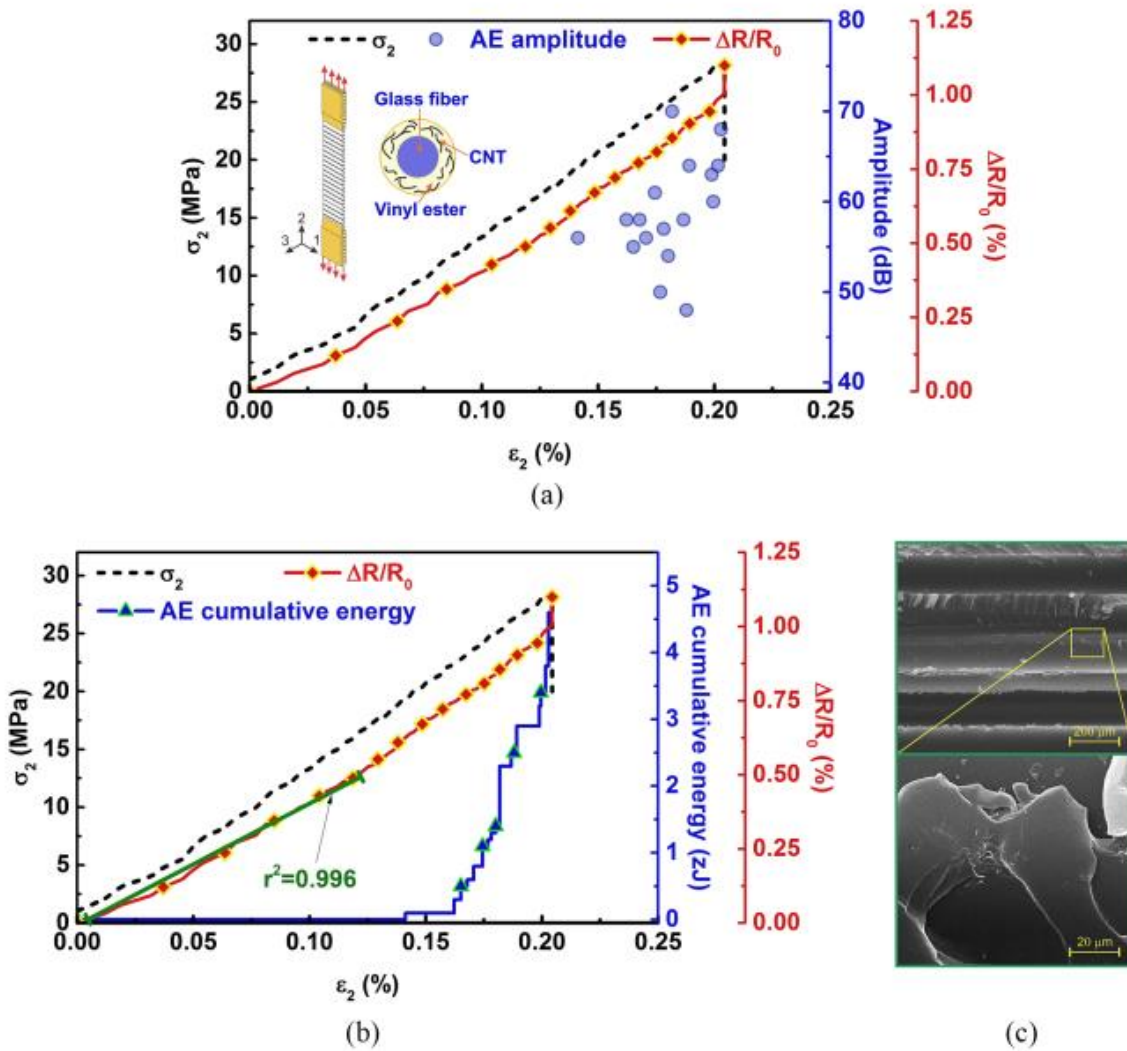
**Figure 2.8:** The mechanical, DC resistance, and AEs of a MWCNT-modified GFRC sample. The (a) stress response, normalized resistance change, and AE can be noted plotted against applied strain, while the (b) acoustic cumulative energy as a function of strain can be noted, as well as (c) an SEM image of the fractured surface [40].

Nofar et al. also studied MWCNT-modified GFRC. Their study investigated low-cycle fatigue loading, monitoring both DC resistance and strain gage readings. Data in their experiment showed an increase in resistance as a function of fatigue. They demonstrated higher DC resistance sensitivity to crack development as compared to strain gage readings [39]. An example plot of their results can be noted in Figure 2.9.
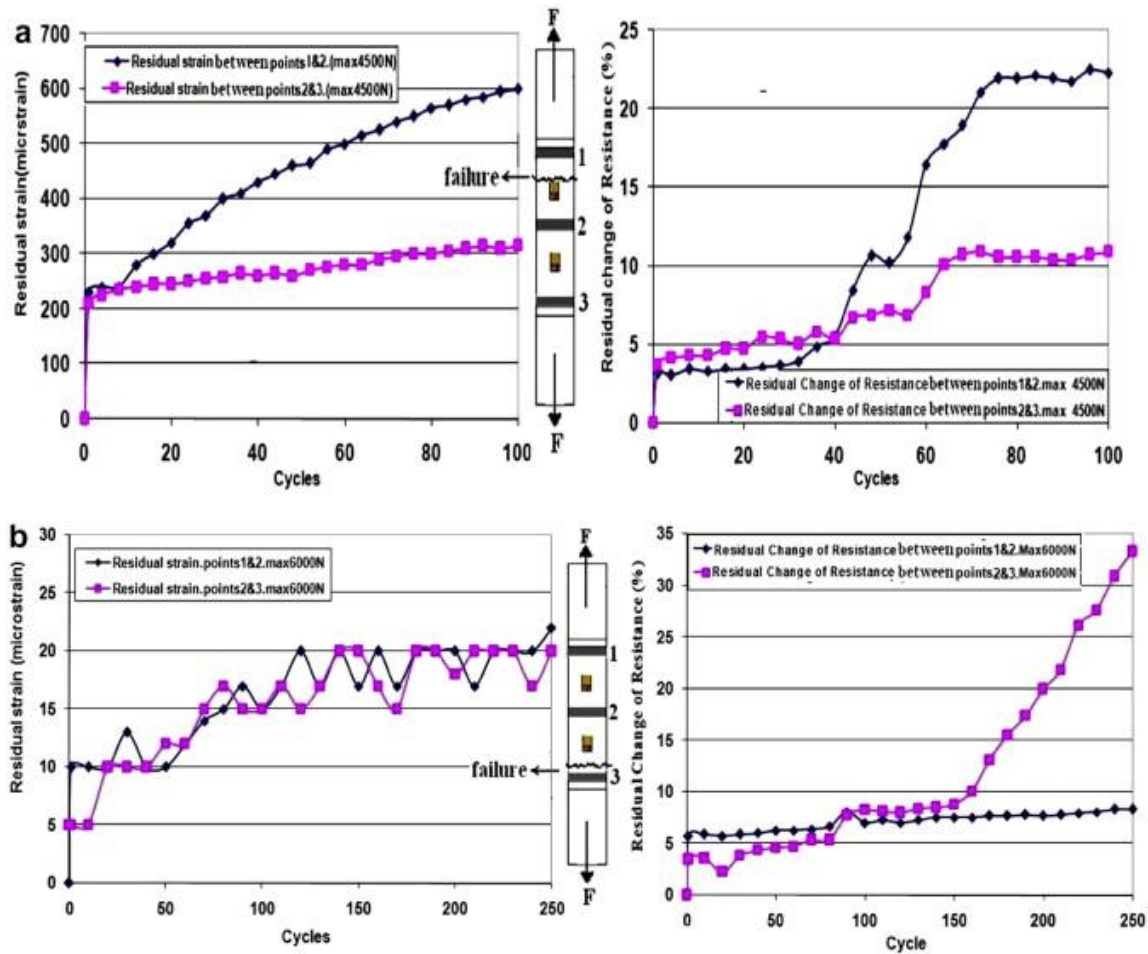
**Figure 2.9:** Residual strain gage change (microstrain) compared to residual change of resistance (%) between two samples and their respective electrode 1 & 2 region (black) and electrode 2 & 3 region (purple). The failure occurred in different regions for the two samples and can be noted in the figure as well [39].

Another investigation of the cyclic loading of nanofiller modified GFRC was performed by Gao et al. Incremental cyclic loading was performed on a CNT-modified laminate. The relative resistance change per unit length of the specimen showed a great deal of sensitivity; permanent resistance change was noted in their specimens as a result of increasing damage. The permanent resistance change indicates the usefulness of this method for SHM [41]. A plot of the incremental cyclic loading compared to the resistance response can be noted in Figure 2.10.
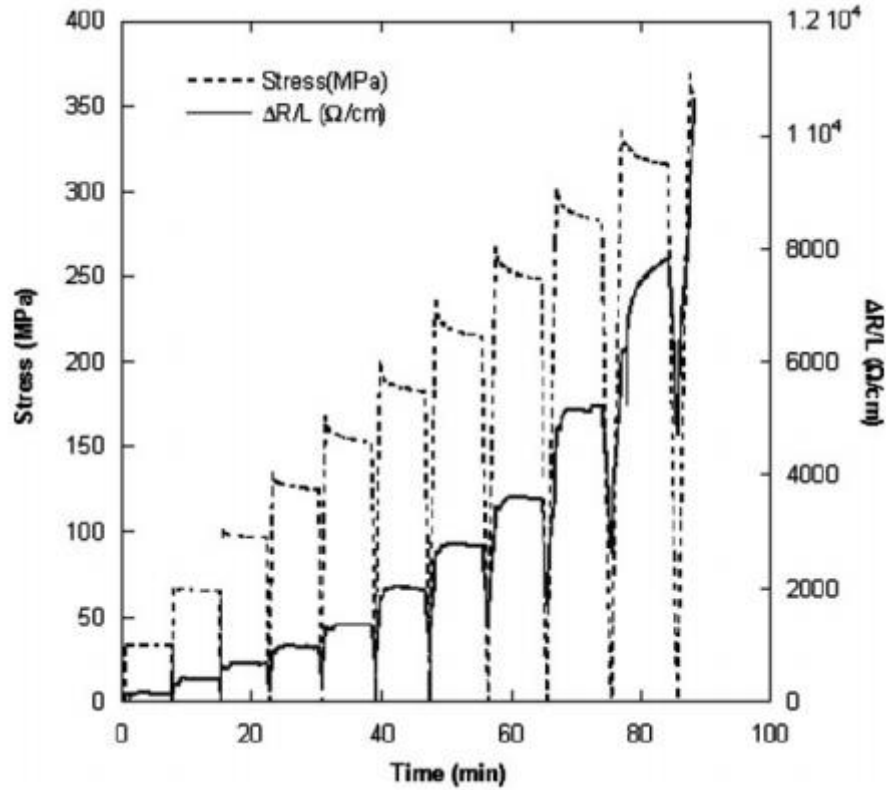
**Figure 2.10:** Incremental cyclic loading of a CNT-modified GFRC. The stress response can be directly compared to the relative resistance per unit length response [41].

The previous methods can be envisioned as 1D conductivity monitoring. That is, a 1D specimen is loaded as simple resistance measurements are taken. A more panoramic methodology uses multiple directions across the specimen to create a conductivity map. With an adequate electrode array, 2D DC characteristics can be leveraged to spatially map damage-induced conductivity. An important development in 2D conductivity monitoring is the usage of electrical impedance tomography (EIT). EIT is the method of characterizing internal conductivity changes using boundary measurements. This method demonstrates conductivity changes spatially through minimally invasive procedures. Tallman et al. demonstrated EIT's resolution on a CNF-modified GFRC with pre-damaged through holes in the specimen. This methodology effectively mapped the conductivity measurements and showed the damage present in the material [25]. A representative damage mapping can be found in Figure 2.11.
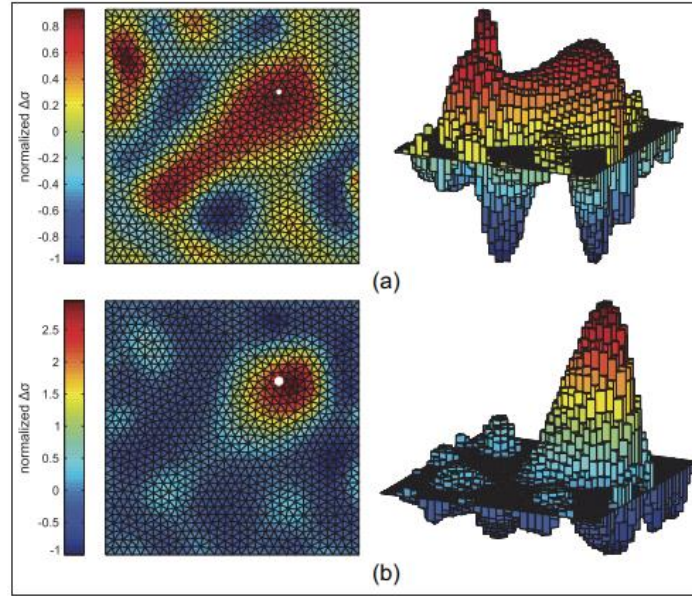
**Figure 2.11:** Damage mapping of small through holes via EIT. The through-holes can be noted as the white circles in the two plates. An (a) EIT reconstruction of a 1.59 mm diameter hole and a (b) 3.18 mm diameter hole can be noted [25].

This EIT modeling has even been extended to structures with different geometry. Notably, Thomas et al. has demonstrated the benefits of EIT on a composite tube. An array of 24 electrodes successfully mapped impact damage onto a cylindrical specimen [22]. A representative figure can be noted in Figure 2.12.
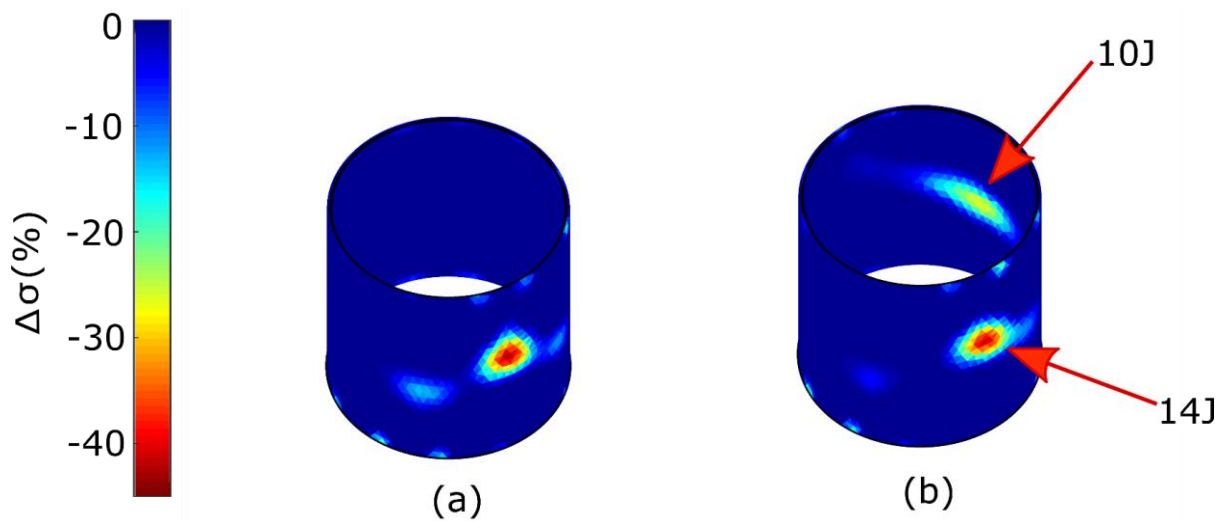


**Figure 2.12:** EIT reconstruction of impact damage on a hollow cylindrical specimen. Impact damage at (a) 14 J and (b) 10 J and 14 J was successfully mapped [22].

These studies lay the groundwork for conductivity monitoring as a field of SHM research. The major benefit of this methodology is that the material itself acts as the sensor and therefore does not require additional sensor attachments. Again, however, work to date has been overwhelmingly focused on DC methods. This is important because prior work has shown that external circuitry can be coupled with the inherent AC response of nanocomposites for improved sensitivity [53]. Further, nanocomposite AC conductivity increases by orders of magnitude at high interrogation frequencies (>1 MHz) thereby substantially reducing power requirements (which may be a limiting factor on large structures with low DC conductivity) [46] [54]. In this light, there is considerable motivation to pursue AC-based piezoresistive SHM.

## 2.2  Equivalent Circuit Modeling

In order to utilize AC methods for FRC SHM, we need to first discuss relevant AC tools. Equivalent circuit modeling utilizes combinations of different circuit parameters such as resistors, capacitors, and inductors to fit experimentally observed impedance data. In essence, we seek some circuit that gives rise to the same AC response as measured from the piezoresistive GFRC. Monitoring changes in equivalent circuit parameters, therefore, provides some insight into damage accumulation. Complex circuit analysis is a useful tool for this where the complex impedance is denoted as $Z = Z' + jZ''$. The modulus of $Z$ is the impedance magnitude, the angle between the real and complex portions ($Z'$ and $Z''$, respectively) is the phase angle, and $j$ is the complex unit.

Resistors, $R$, are measured in Ohms and are purely real impedance, $Z_R$. A resistor's impedance is described in equation (2.2). Resistors have no frequency dependency. Capacitors exhibit a negative inverse relationship with frequency (the voltage lags the current by 90$^\text{o}$). On the other hand, inductors exhibit a positive direct relationship with frequency, where the phase of the current lags the voltage by 90$^\text{o}$. The impedance expressions related to frequency for capacitors, $Z_C$, and inductors, $Z_L$, can be seen in equations (2.3) and (2.4) respectively. In these expressions $C$ refers to the capacitance measured in Farads and $L$ refers to the inductance measured in Henries. The expression $\omega = 2\pi f$ defines the angular frequency where $f$ is frequency in Hz.

$$Z_R = R \tag{2.2}$$

$$Z_C = \frac{1}{j\omega C} = \frac{1}{j2\pi f C} = -\frac{j}{2\pi f C} \tag{2.3}$$

$$Z_L = j\omega L = j2\pi f L \tag{2.4}$$

In the limit as $f \to \infty$, the impedance of the capacitor goes to zero while the impedance of the inductor goes to infinity. AC analysis is greatly aided by Nyquist plots of complex impedance, parametric plots where the real part of complex impedance can be plotted on the $x$-axis and the imaginary part on the $y$-axis. Because of the positive and negative relationships in the imaginary component of impedance, a negative imaginary portion of impedance is indicative of capacitive behavior while a positive imaginary portion is indicative of inductive behavior. The network of randomly distributed nanofillers creates regions of capacitive behavior and inductive behavior. It is important to monitor how the real and imaginary portions of complex impedance change to determine which behavior is the dominant electrical mechanism. This relationship can be noted in a representative Nyquist schematic in Figure 2.13.
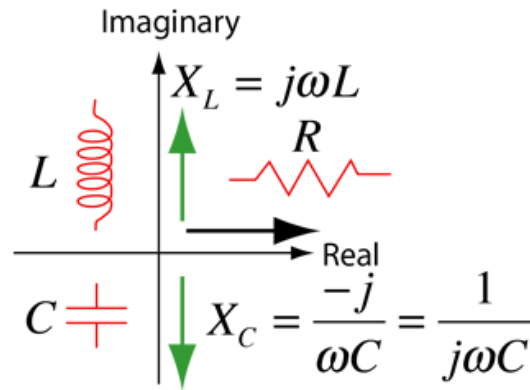


**Figure 2.13:** Complex impedance monitoring for AC circuits. In the complex plane, resistance moves along the real axis while the frequency-dependent components, capacitance and inductance, move along the imaginary axis. Inductors have a positive imaginary component while capacitors have a negative imaginary component [55].

Composite materials with nanofiller-modified polymers always use a parallel resistor-capacitor in the circuit to model the semicircular behavior present in the Nyquist plots [14] [18] [19] [22]. Including a series resistor is an important addition as it defines the bulk resistance of the material [31] [56]. By implementing an equivalent macroscale circuit, ideally, the trends of an equivalent circuit can be used for SHM. As the composite fatigues, the microcracks and coalesced cracks

that form in the matrix phase have associated changes in the equivalent circuit model's parameters. These changes can be used as indicators for SHM.

## 2.3   Prior Work on the AC Response of Piezoresistive Nanocomposites

To date, work on nanocomposite AC has predominantly focused on macroscale effects. AC impedance monitoring has been performed on moisture and thermally-induced damage on composite specimens [31] [35]. Another major example of this AC impedance monitoring is the implementation of an in-situ strain gage using nanofiller modified regions on the material [33] [34] [37] [44]. A common method of AC data analysis is utilizing equivalent macroscale circuit fitting to frequency-response data [31] [35] [36] [37] [38] [56] [57] [58] [59] [60]. Monitoring the equivalent circuit elements as load, damage, and deformation evolve can provide insight into how the material microstructure changes.

A study by Bekas et al. investigated the effects of thermal shock cycles on a nanocomposite. The material they used was a CNT-modified epoxy. The specimens were subjected to 2 h cycles of $30\,^{\circ}C$ and $-30\,^{\circ}C$. The impedance data obtained from the specimens after 0 cycles, 30 cycles, and 70 cycles was fit to an equivalent parallel capacitor-resistor circuit model. The resistance showed an increase and the capacitance decreased as a function of thermal shock damage [35]. This can be noted in Figure 2.14.
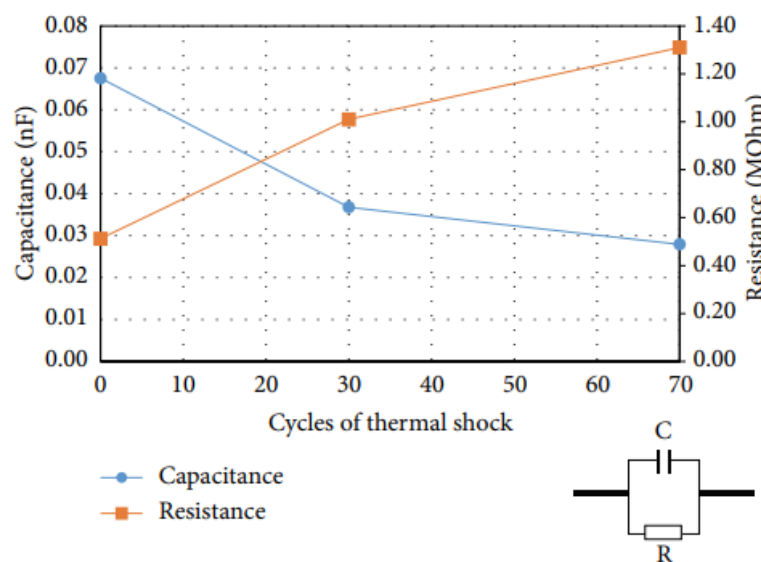


**Figure 2.14:** Equivalent circuit fitting versus 0, 30, and 70 thermal shock cycles [35].

Sanli et al. demonstrated the usefulness of equivalent circuits for nanocomposites in their study. They utilized MWCNT-modified epoxy at 0.3 wt.%, 0.4 wt.%, 0.5 wt.%, 0.75 wt.%, and 1 wt.%. The specimens were then subjected to quasi-static uniaxial tension while also monitoring strain changes (through digital image correlation) to relate it to AC impedance changes. Sanli et al. used a simplified parallel resistor and capacitor model to fit their data. They noted that with increasing weight percentage relative to an increasing strain change, the relative resistance increased less and less. The capacitor showed a similar trend however the relative capacitance decreased less and less. These plots can be noted in Figure 2.15 and Figure 2.16. Sanli et al. further showed that in low-cycle loading the relative resistance profile follows the cyclic strain profile [38].
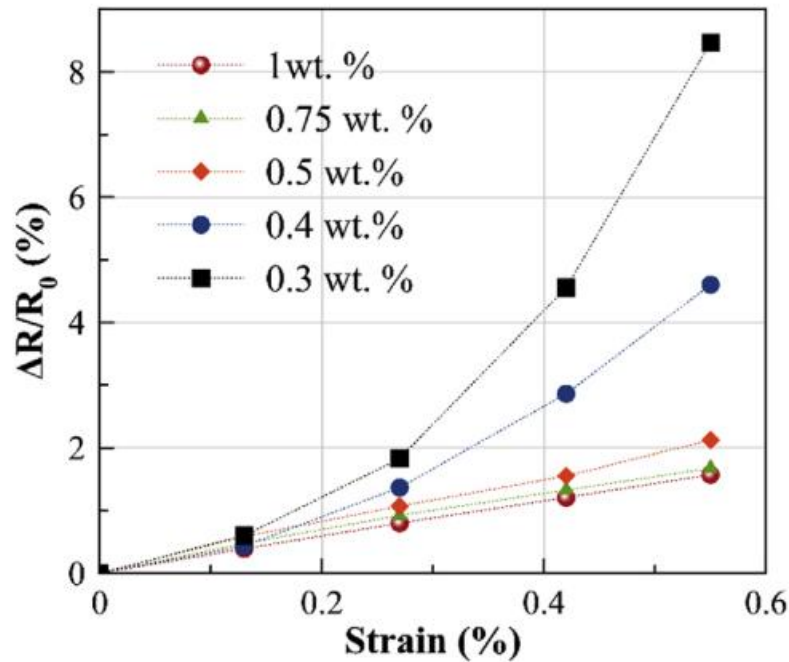


**Figure 2.15:** Relative resistance change of MWCNT-modified epoxy nanocomposite subjected to uniaxial tensile strain at different weight percentages [38].
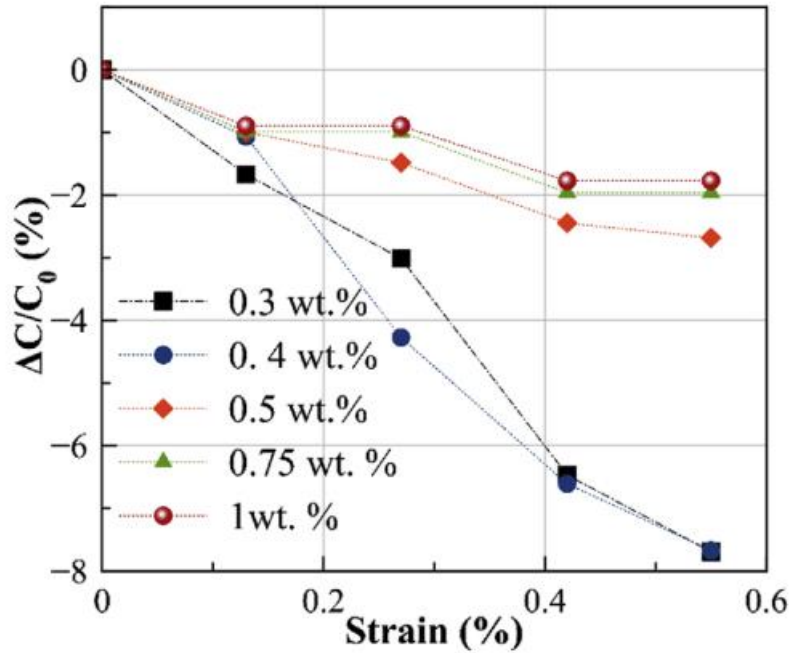
**Figure 2.16:** Relative capacitance change of MWCNT-modified epoxy nanocomposite subjected to uniaxial tensile strain at different weight percentages [38].

A different study by Bekas et al. investigated the effects of hygrothermal exposure to a GFRC modified with MWCNT. The hygrothermal exposure onto the samples was performed with varying lengths of time. The materials were then subjected to a loading-unloading cycle. The specimens were tensile step-loaded by 20% increments up to ultimate tensile strength (UTS). An equivalent circuit fitting routine was performed to model the impedance data. This circuit model was a simple resistor and capacitor in parallel. These parameters as a function of damage can be noted in Figure 2.17 and Figure 2.18. What Bekas et al. have shown is that damage both hygrothermally as well as mechanically results in changes to the equivalent circuit parameters. There is a direct correlation between material degradation and impedance data changes. Equivalent circuit modeling shows that the MWCNT network becomes disrupted; increasing damage results in increasing resistance and decreasing capacitance [31].
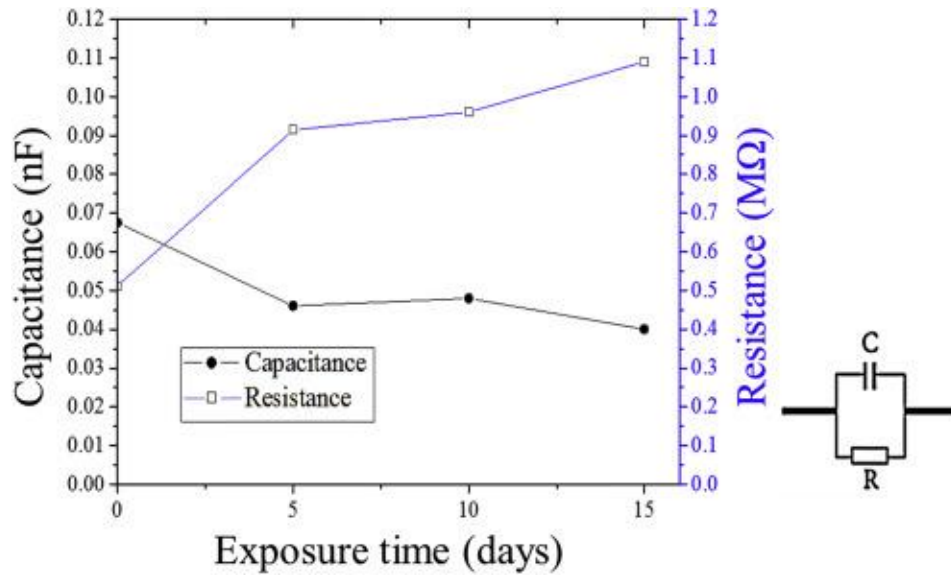
**Figure 2.17:** Equivalent circuit model parameters for hygrothermal damage. The resistance increases and capacitance decrease as a function of damage [31].
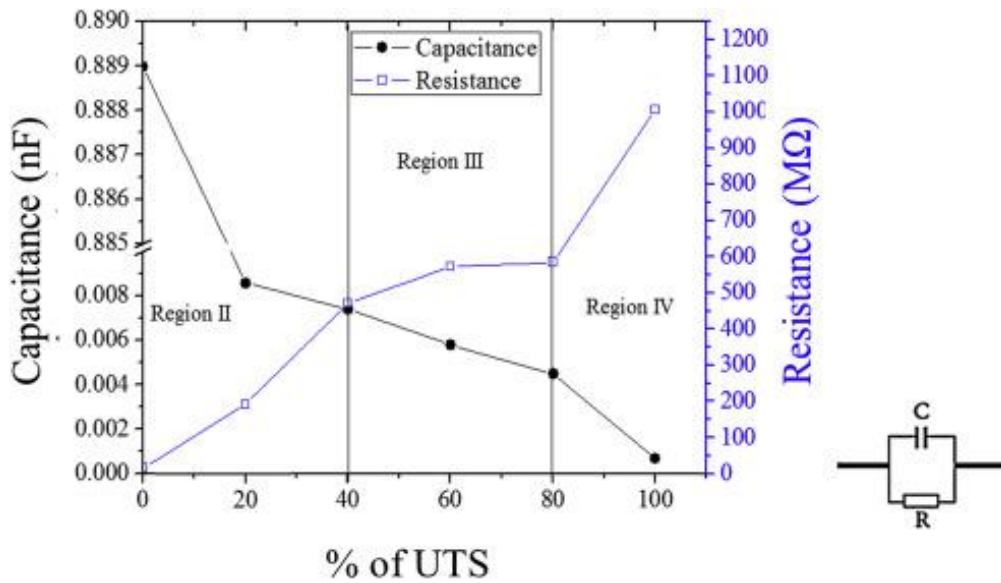


**Figure 2.18:** Equivalent circuit model parameters for mechanical damage. The resistance increases and capacitance decrease as a function of percent of UTS damage. This trend increases more significantly than in Figure 2.17 [31].

Another AC damage study involved cantilever beam fatigue. Sanli et al. embedded MWCNTs via a stencil printer onto a small region of a GFRC laminate. This MWCNT-modified region acted as an in-situ strain gage. This composite laminate was then fatigued in a cantilever beam

set up. During the fatigue loading, the impedance data was recorded and simultaneously fit to an equivalent circuit using a spectrum analyzer tool. In this study, the circuit selected to fit the data is a simplified resistor and capacitor in parallel. Monitoring the imaginary component of complex impedance as well as the corresponding circuit parameters as a function of load can be noted in Figure 2.19. Resistance increases as a function of the load while capacitance decreases, similar to previously discussed studies [33].
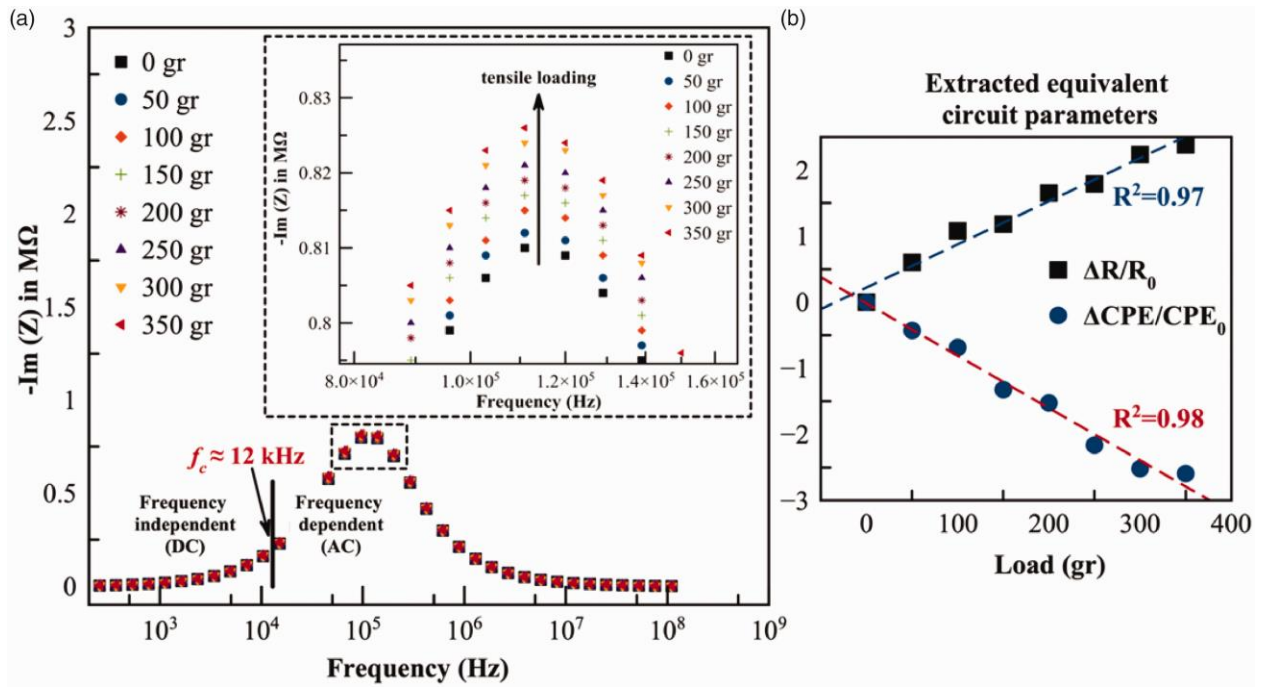


**Figure 2.19:** The change in the (a) imaginary component of complex impedance as a function of interrogation frequency as well as the (b) simplified relative resistor and relative capacitor changes of the sensor [33].

Loyola et al. investigated the effects of uniaxial tension on a GFRC modified with MWCNT. The strain sensitivity of the layers was tested as a function of strain development and circuit parameters were monitored to characterize the development of damage. Their circuit design included the standard parallel resistor-capacitor previously discussed with the inclusion of a series resistor. This data was compared to DC resistance measurements. The equivalent circuit model demonstrated with increasing strain the series resistor and parallel capacitor increased in relative order of magnitude while the parallel resistor decreased. Interestingly, the series resistor

and DC resistance were nearly identical measurements [56]. A comparison of their AC data and the circuit parameter changes as a function of microstrain can be noted in Figure 2.20.
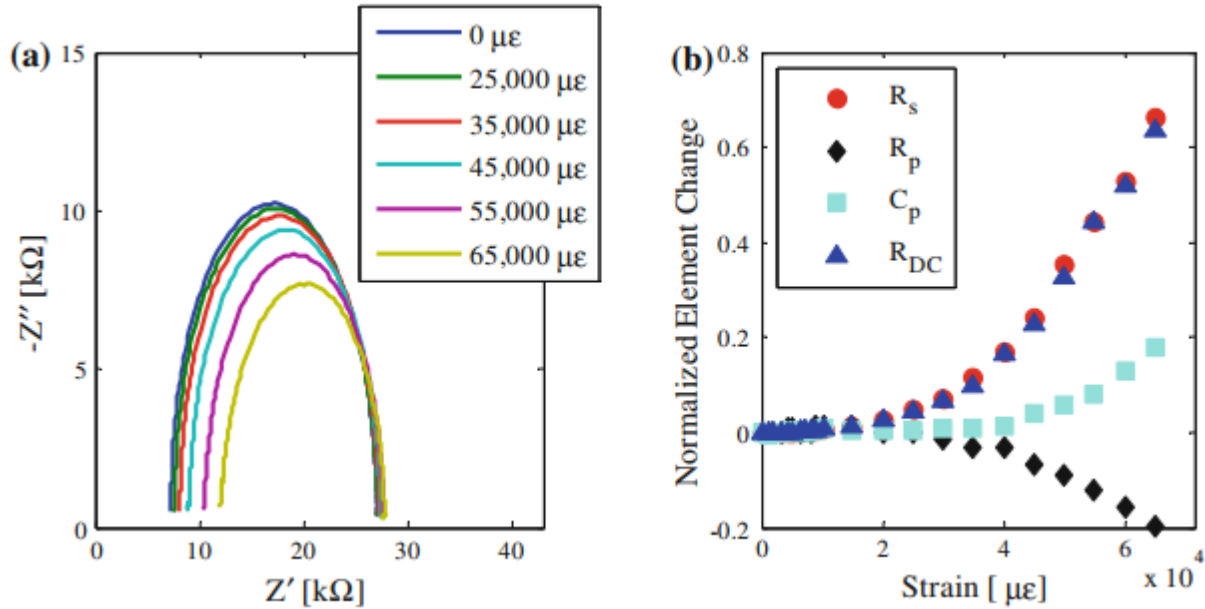


**Figure 2.20:** The (a) AC impedance data plotted parametrically with the real part on the *x*-axis and negative the imaginary part on the *y*-axis can be noted. Further, the (b) circuit parameter evolution as a function of microstrain in the tensile-loaded GFRC with MWCNT-modified polymer can be noted [56].

# 3. PROBLEM STATEMENT & RESEARCH GOAL

## 3.1 Problem Statement

FRCs are increasingly being used due to their excellent specific properties. However, they are also vulnerable to complex and difficult-to-predict failure mechanisms, particularly under high-cycle fatigue loading. SHM is therefore important for these materials, but traditional SHM methods also suffer from important limitations. Piezoresistive-based self-sensing has the potential to overcome these limitations. AC-based piezoresistive self-sensing is especially promising for this because of the potential for improved data density, better sensitivity, and reduced power requirements. Unfortunately, little-to-no work has been done to explore the effect of fatigue-induced damage on AC transport in piezoresistive FRCs.

## 3.2 Research Goal

Motivated by the potential of AC-based self-sensing for FRC SHM, the research goal of this thesis is to develop new basic insights on the AC response of piezoresistive nanofiller-modified GFRCs in response to high-cycle fatigue loading. Specifically, this thesis aims to characterize the AC response of a CNF-modified GFRC in response to tensile fatigue loading with an open-hole stress concentration. By studying GFRC specimens with CNF-modifications, the AC data response as a function of cycles (and damage) can provide insight into how this methodology can be used as a SHM system. Furthermore, a new circuit model is proposed which models pathways in terms of the possible inter-nanofiller junctions within the material. The goal of this study is to characterize the AC response of GFRC with CNF-modified epoxy to cement piezoresistive self-sensing as an alternative to traditional SHM.

# 4. EXPERIMENTAL METHODS

With the background information and motivation established, this chapter goes into the experimental procedure. First, the manufacturing procedure is laid out. Second, the mechanical loading methodology is presented. Finally, the electrical measurement process is discussed.

## 4.1 Manufacturing

### 4.1.1 Dispersion and Layup

GFRC with CNF-modified epoxy material was used for this thesis study. The CNF-modified epoxy was produced using Fibre Glast 2000 epoxy resin and Fibre Glast 2060 epoxy hardener. The CNFs were purchased from Applied Sciences. Applied Sciences pretreats the CNFs at 3000 $^o$C such that they have low iron content with high graphitization. The CNFs are stacked-cone Pyrograf III PR-24-XT-HHT with average diameters of 0.1 μm and lengths ranging from 50 to 200 μm. The resulting surface area is around 41 m$^2$/g (Pyrograf products, Inc., 2011).

This FRC was manufactured via vacuum bag wet layup. Six 10" × 10" layers of GF were cut from Fibre Glast 7725 Bi-directional E-glass. Note these layers are 0$^o$/90$^o$ weaves of GF. A flat 18" × 18" aluminum tool was used for the layup procedure. First, the vacuum bagging layers were prepared. Two 16" × 16" layers of peel ply were cut, along with two 4" × 4" layers for the pressure gauges. A 16" × 16" layer of breather material was cut, as well as four 4" × 4" layers for the pressure gauges. A 16" × 16" layer of release film was cut and an 18" × 18" layer of vacuum bag material was cut.

Three different batches were made with CNFs added at 0.5 wt.%, 1.0 wt.%, and 1.5 wt.% relative to the combined weight of the epoxy resin and hardener. To produce the CNF/epoxy, the CNFs were first weighed and dispersed in 50 g of epoxy resin – the epoxy resin density used for this stoichiometric measurement was 1138.35 kg/m$^3$ (provided by Fibre Glast). The dispersion was facilitated by a combination of surfactant and bath sonication. Triton X-100 surfactant was added at a ratio by weight of 0.76:1 relative to the CNFs. From here, acetone was added at a volume ratio of 2:1 of the epoxy and hardener to the CNFs, epoxy resin, and surfactant to lower the viscosity of the mixture. Before the sonication step, the mixture containing CNFs, epoxy

resin, surfactant, and acetone was placed in a planetary centrifuge mixer for 5 min. Next, the mixture was placed in a bath sonicator for 4 h; the bath sonicator operated at an average power of 35 W at a frequency of 45 kHz. Following the sonication, the mixture was placed on a hot-plate stirrer for 24 h at a temperature of 60 $^o$C. The elevated temperature ensured all acetone evaporated out of the mixture. After sufficient mixing and evaporation, the CNF/epoxy with surfactant mixture was cooled to room temperature. At room temperature, the Fibre Glast 2060 hardener was mixed in at a ratio by weight to the epoxy resin of 27:100. BYK-A 501 air-release agent was then added to the mixture at a ratio by weight in the range 0.1-to-0.5:100 relative to the epoxy resin and hardener. The mixture was degassed for 30 min at room temperature. SEM images of leftover CNF/epoxy mixture can be noted in Figure 4.1. Electrical percolation as low as 0.25 wt.% CNF has been noted in CNF/epoxy (i.e. without reinforcing fiber) using this manufacturing method [61].
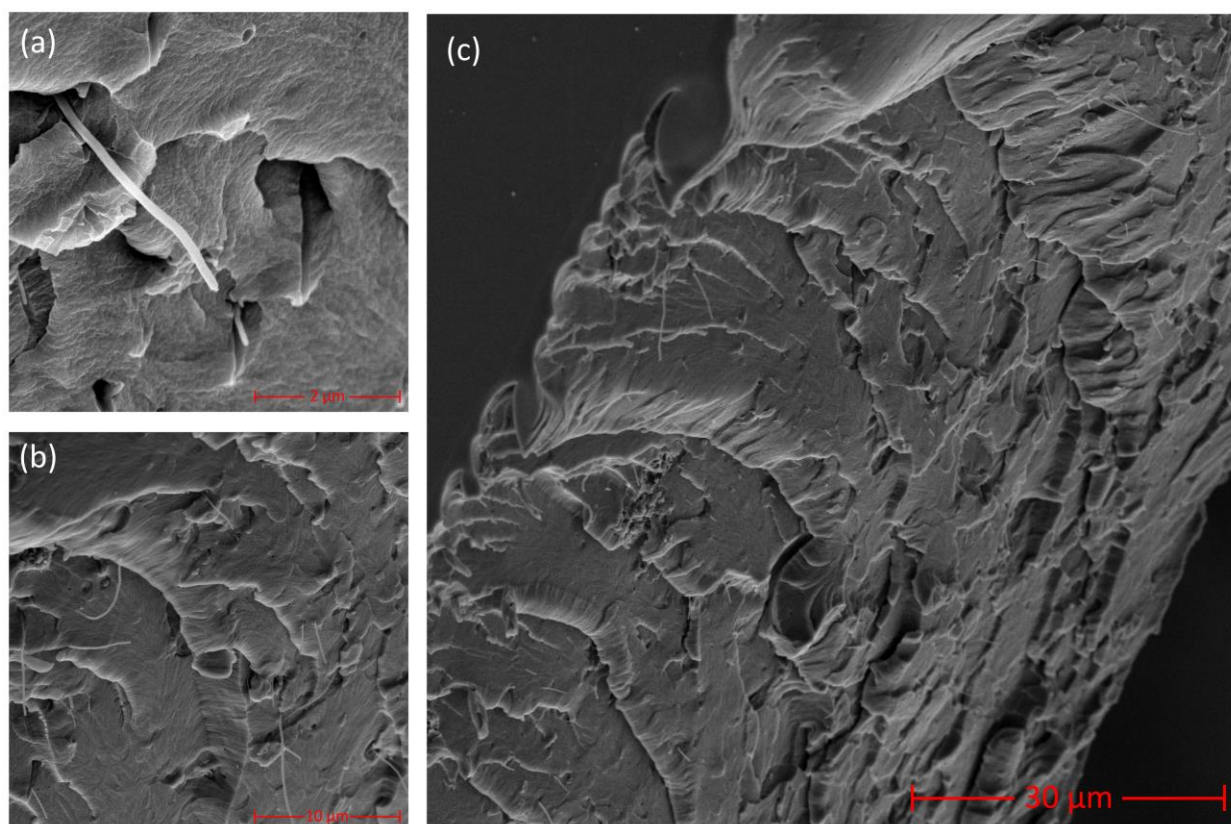


**Figure 4.1:** SEM images of 1.5 wt.% CNF/epoxy mixture fracture surface. In these images (a) a single CNF can be seen protruding from the fracture surface, (b) an outfield view of the CNF/epoxy mixture surface can be seen with CNFs protruding from the surface, and (c) a further zoomed out view can be noted.

During degassing, the tool was prepared for the wet layup procedure. Sealant (tacky) tape was applied to the edges of the aluminum tool. The inner area of the tool was cleaned with acetone. Mold release was applied to the tool thrice in 5 min intervals. Once a mold release layer was established, the release film and a layer of peel ply were placed atop the tool. Once the 30 min degassing finished, a base layer of the CNF/epoxy mixture was placed on the peel ply. From here the CNF/epoxy was impregnated into the GF fabric layer-by-layer using a paintbrush and a squeegee to evenly spread the mixture. Upon completion, the second layer of peel ply and the layer of breather were placed atop the layup. Two 'sandwiches' – 4" × 4" peel ply surrounded by two 4" × 4" breather on either side – were placed on opposite ends of the tool (avoiding the laminate). The pressure gauge bottoms were then placed on these. The vacuum bag was laid over the top of the sealant tape.

A pressure gauge and vacuum pump nozzle were attached through the vacuum bag to the two gauge bottoms. The vacuum pump was turned on and the vacuum in the tool was monitored for leaks. Once the vacuum was confirmed, the tool with the GFRC with CNF-modified epoxy was transferred to the oven. The vacuum stability was then again ensured. The specimen was cured at 60 $^{\circ}$C for 5 h. SEM images of the cured GFRC with the CNF-modified epoxy after fatigue-induced fracture can be noted in Figure 4.2, Figure 4.3, and Figure 4.4.
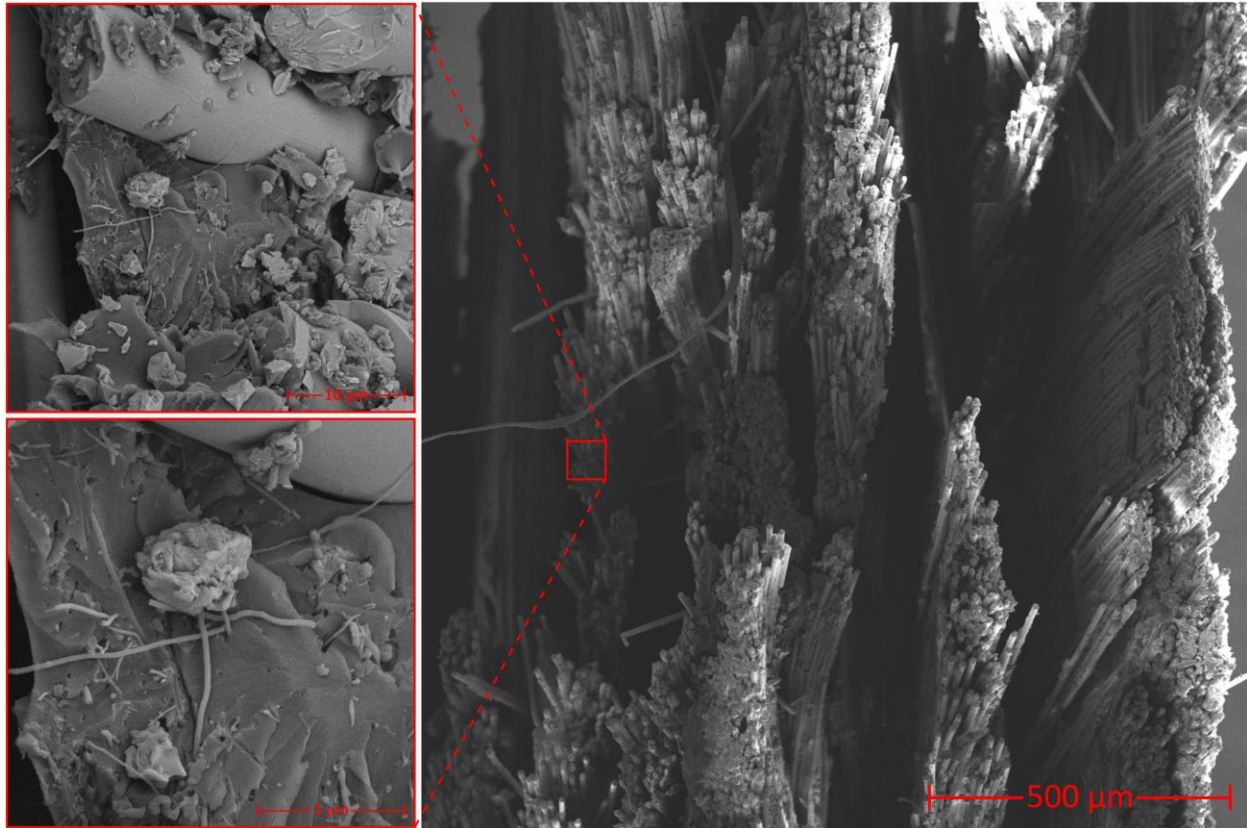
**Figure 4.2:** SEM images of the GFRC with CNF-modified epoxy (at 1.5 wt.%) fracture surface. The 6 weave layers can be noted in the right, larger image. In the upper-right image, GFs can be noted as the large cylinders and the relatively small CNFs can be noted in the left region of the image. The difference in fiber size is well highlighted in this image. The bottom right further zooms in on the epoxy-phase highlighting the CNFs present on the surface of and embedded into the matrix.
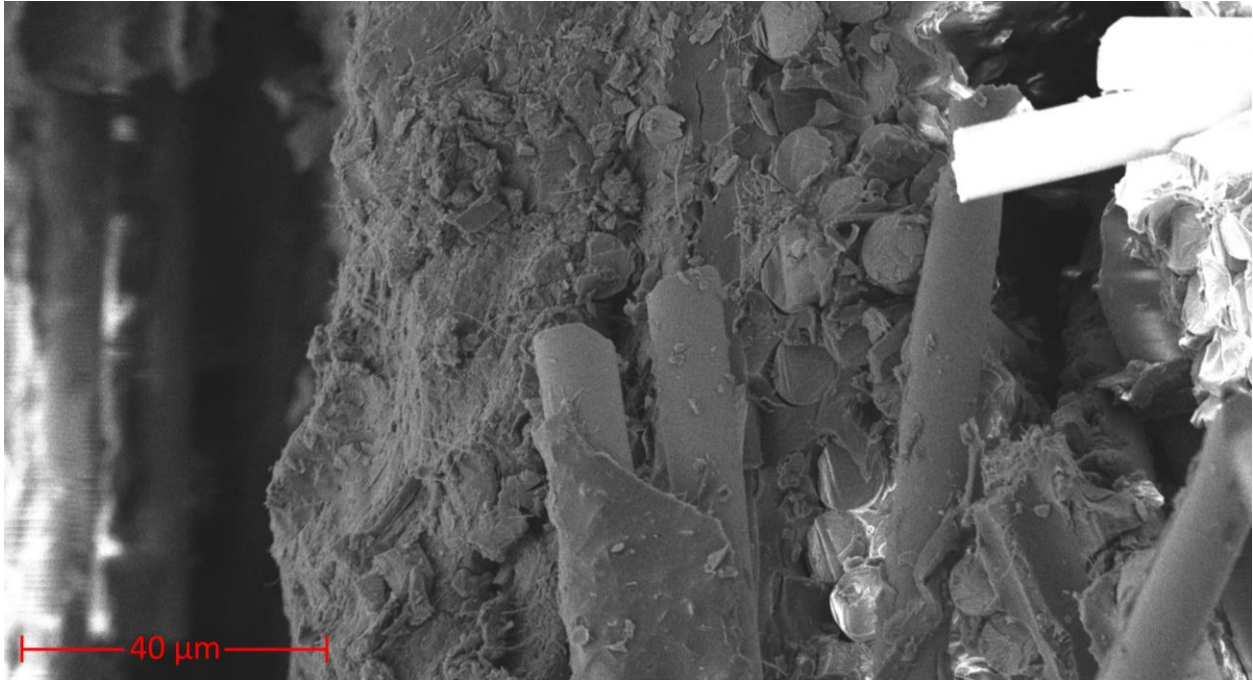
**Figure 4.3:** This SEM image highlights the CNF-modified epoxy phase. Note all of the CNFs present in this surface that fully impregnates the GF weave. This composite material is composed of three major elements: the GFs, the epoxy, and the CNFs.
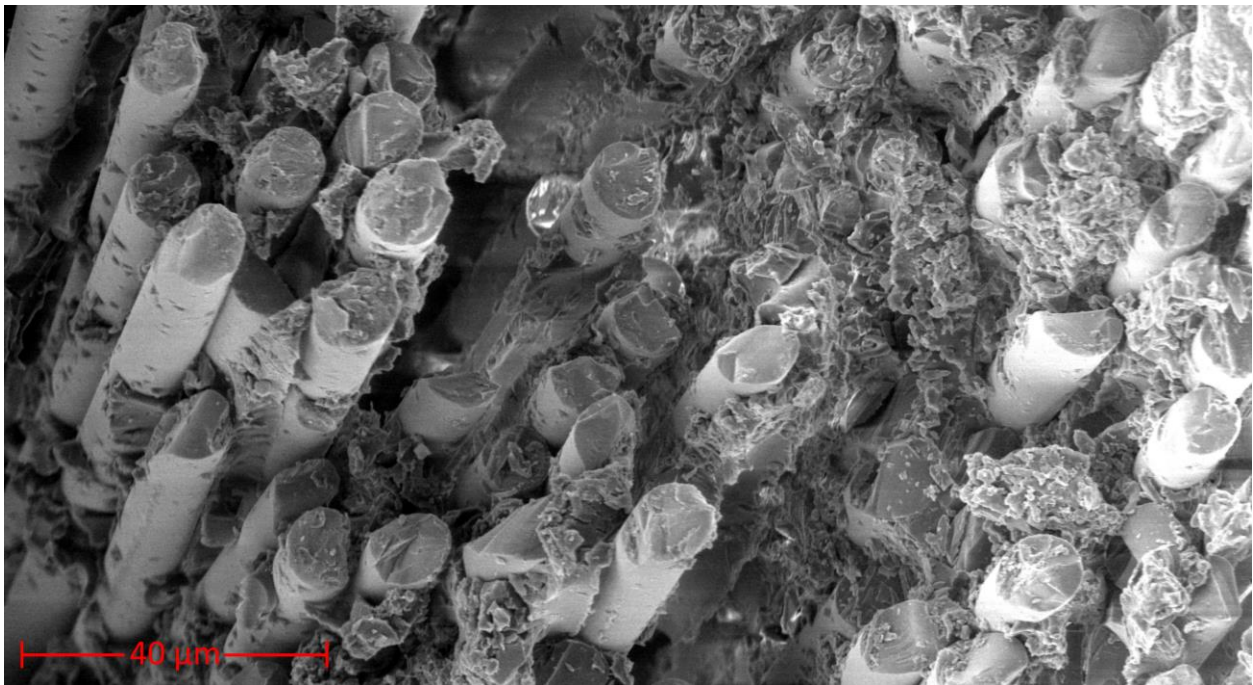


**Figure 4.4:** The GFs fracture surface can be noted in this SEM. Note the uneven epoxy surface present throughout the GF fabric. This epoxy is impregnated with a randomly distributed and well-connected CNF network.

### 4.1.2   Finishing

The cured specimen was sized using a wet ceramic table saw to a 9" × 9" plate. Four strips of 1.5" × 9" nonconductive tab material were sized in the wet ceramic table saw. These strips were attached to the edges of the GFRC with CNF-modified epoxy plate using 3M Scotch-Weld Epoxy Adhesive 3501 B/A Gray. The sample edges were clamped down and the adhesive was allowed to set for 12 h. Once set, the plate with grip tabs was sized to 1.5" wide strips. This amounted to four specimens per plate.

The four test bars were then drilled with a 0.25" drill bit to produce the open-hole. The hole-to-width ratio guidelines from the ASTM D7615/D7615M Open-Hole Fatigue Response of Polymer Matrix Composite Laminates standard were followed where the hole diameter, $D$, had to be less than or equal to $1/5^{th}$ of the specimen width, $w$, $D/w \leq 0.2$. The hole was drilled through the center of the test bars clamped between two spare GFRCs to minimize delamination effects from penetration. Representative post-manufactured specimens can be noted in Figure 4.5 and Figure 4.6. The sample dimensions can be noted in Table 4.1.

**Table 4.1:** Sample dimensions. The 1.0 wt.% CNF samples 1 and 3 hole diameter were not measured and therefore the expected diameter is included (the average does not include these values).

|  | 0.5 wt.% | | | 1.0 wt.% | | | 1.5 wt.% | | | |
| --- | --- | --- | --- | --- | --- | --- | --- | --- | --- | --- |
|  | 1 | 2 | 3 | 1 | 2 | 3 | 1 | 2 | 3 | Average |
| Thickness [$mm$] | 1.31 | 1.28 | 1.31 | 1.25 | 1.27 | 1.26 | 1.23 | 1.23 | 1.25 | **1.26** |
| Width [$mm$] | 38.7 | 39.0 | 39.0 | 38.9 | 38.6 | 38.7 | 39.0 | 39.1 | 38.7 | **38.9** |
| CA [$mm$] | 50.8 | 49.8 | 51.0 | 48.8 | 48.9 | 48.7 | 48.1 | 48.2 | 48.3 | **49.2** |
| Hole Diameter [$mm$] | 6.19 | 6.25 | 6.40 | 6.35 | 6.20 | 6.35 | 6.29 | 6.28 | 6.32 | **6.27** |
| Gauge Length [$cm$] | 13 | 13 | 13 | 16 | 15 | 16 | 16 | 16 | 16 | **14.8** |
| Total Length [$cm$] | 21 | 21 | 21 | 23 | 23 | 23 | 24 | 24 | 24 | **22.4** |

## 4.2    Mechanical Loading

Before fatigue testing, one of the test bars from each CNF weight fraction batch was loaded to failure at 2 mm/min to characterize the UTS. The fatigue experiment was performed following the ASTM D7615/D7615M standard. This experiment used an Instron 8801 (100kN) Fatigue Testing Systems. A sample in the load frame grips can be noted in Figure 4.5. The UTS characterization was used as an initial estimate for the upper limit of strength for determining the fatigue cycle of the other bars. The Instron load frame was used to collect stiffness data during loading.
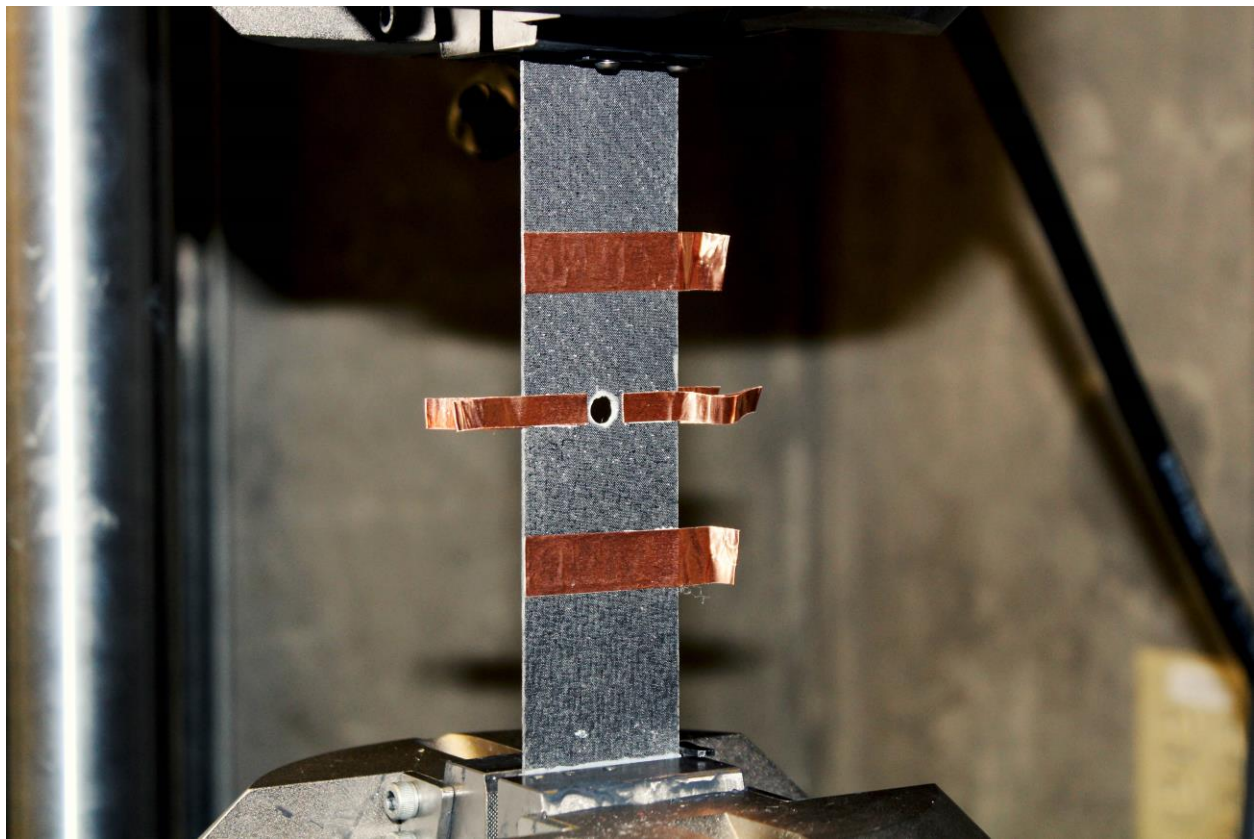


**Figure 4.5:** GFRC with CNF-modified epoxy specimen in load frame grips. The copper tape can be noted at the various AC interrogation points on the specimen. The extra material hanging off the ends of the sample is where the wires with alligator clips connected to the impedance analyzer attach.

The fatigue cycle was performed at 1 Hz to 50% of the UTS. The test was performed at 1 Hz to ensure temperature effects from fatigue were not an issue. The ultimate strength and maximum

load for each of the specimens tested are tabulated in Table 4.2. This experiment was an interrupted tension fatigue cycle. It was interrupted at set intervals per the standard for impedance and stiffness data collection. The test was interrupted after 1, 2, 5, 10, 20, 50, 100, 200, 500, 1,000, 2,000, 5,000, 10,000, 20,000, 50,000, and 100,000 cycles. Data was collected within 15 minutes post interruption, and then the test was continued. All specimens failed before 200,000 cycles.

**Table 4.2:** UTS and the elastic limit for all 3 weight percentages and 3 samples tested per weight fraction.

| | | 0.5 wt.% | 1.0 wt.% | 1.5 wt.% |
|---|---|---|---|---|
| **Elastic Limit** | **Sample 1 [*MPa*]** | 100.7 | 115.5 | 110.7 |
| | **Sample 2 [*MPa*]** | 106.4 | 109.7 | 106.4 |
| | **Sample 3 [*MPa*]** | 102.3 | 119.4 | 99.35 |
| | **Average [*MPa*]** | **103.1** | **114.9** | **105.5** |
| | **UTS [*kN*]** | 11.66 | 11.30 | 11.67 |

## 4.3    Electrical Measurements

Firstly, note that filler alignment was not assessed in the finished specimens as there are certainly effects from resin flow, but because discrete measurements of impedance were taken this was not considered a limitation. AC impedance magnitude and phase angle were measured in three directions through the GFRC with CNF-modified epoxy specimens as shown in Figure 4.6. The electrodes were attached to the specimens using a combination of silver paste and copper tape. Ted Pella, Inc. Pelco Conductive Silver Paint was painted on the surface of the specimens in six different areas. 2.4 cm above and below the hole a 1 cm wide strip of paint was applied across the span of the specimens; this was defined as the 'front' face of the specimen. On the same face, silver paint was applied in a 0.5 cm × 1.0 cm region adjacent to the hole on either side. On the 'back' side, the same 0.5 cm × 1.0 cm regions were painted. Once dried, any excess silver paint was sanded off the sample. Ted Pella, Inc. 3M Copper Conductive Tape was placed atop the silver-painted regions. This made up three interrogation electrodes: through the thickness on either side of the hole and across the length of the specimen through the two strip regions. The

lengthwise interrogation was defined as length 1 while the two through-thickness interrogations were defined as through-thickness 2 and 3.
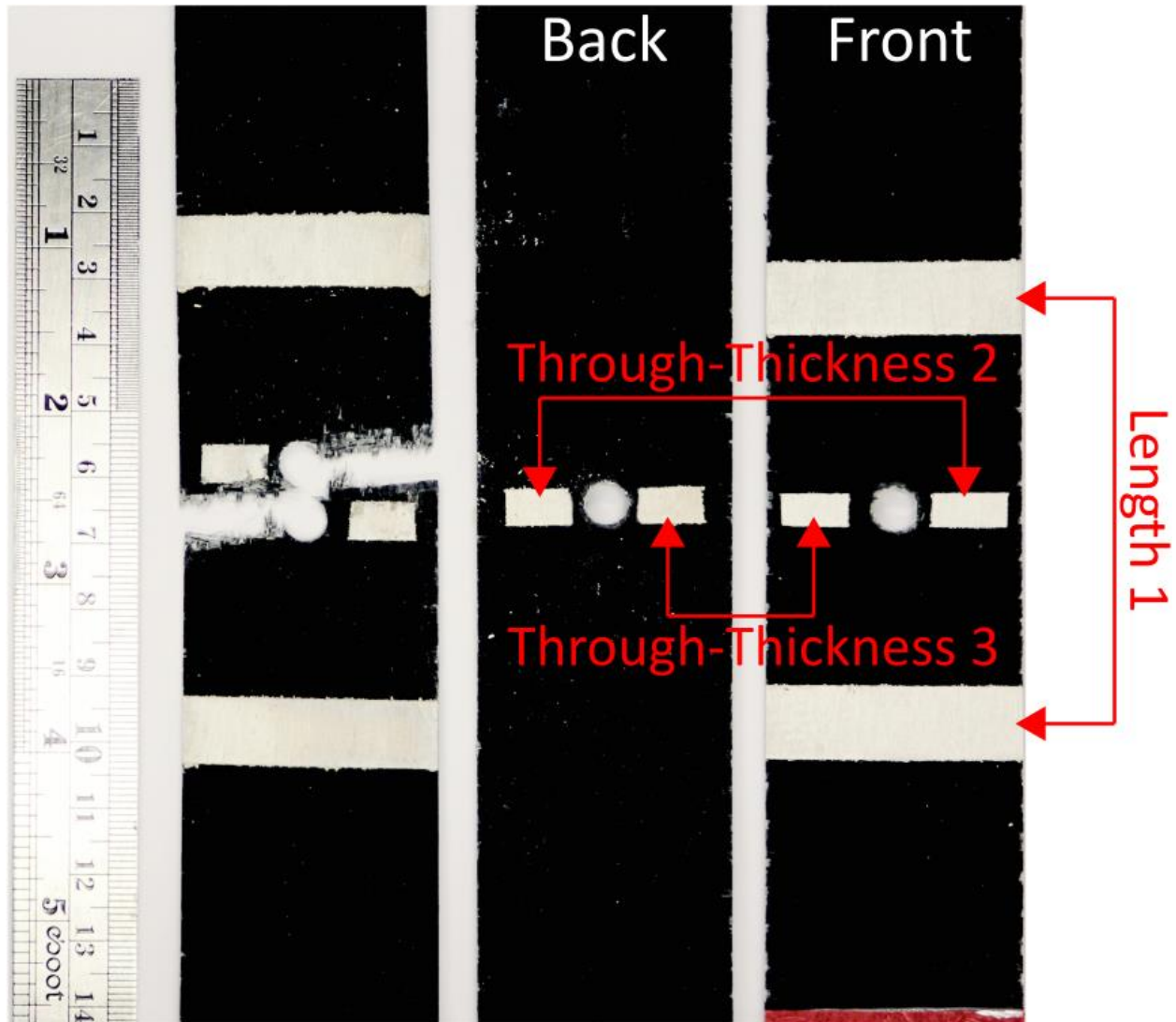


**Figure 4.6:** Instrumented, post-manufactured test specimens with a representative post-failure specimen. The three directions of impedance interrogation are shown in this image. These three AC interrogation directions are as follows: length 1 across the length, through-thickness 2 through one side of the hole, and through-thickness 3 through the other side of the hole. Note that insulating tabs are not present in this image.

Impedance interrogation was performed via a Keysight E4990A Impedance Analyzer sweeping from 20 Hz to 10 MHz. An initial AC interrogation was performed to provide a base standard of the electrical properties present in the material. The impedance analyzer collected the impedance

magnitude and phase angle of the nanocomposite as a function of interrogation frequency. Complex impedance is denoted by the expression $Z = Z' + jZ''$ where $Z$ is impedance and $j$ is the complex unit, $j = \sqrt{-1}$. In this expression, $Z'$ refers to the real part of the impedance and $Z''$ refers to the imaginary part. Equations (4.1) and (4.2) convert the measured impedance magnitude and phase angle into the real and complex portions respectively.

$$Z' = |Z|\cos(\theta) \tag{4.1}$$

$$Z'' = |Z|\sin(\theta) \tag{4.2}$$

# 5. RESULTS & DISCUSSION

Having considered how the materials were manufactured, loaded, and electrical measurements taken, we next consider the fatigue loading impacts on material degradation. This chapter will be organized as follows. First, the mechanical results are shown. Second, the DC results are presented followed by the AC results. Finally, the equivalent circuit process and derived parameters are explained.

## 5.1 Mechanical Results

### 5.1.1 Specimen Failure

The discussion herein presented on specimen failure is simply based on post-failure observations. Since an investigation of the mechanisms and origins of failure was beyond the scope of this thesis work, no definitive conclusions should be drawn from these results. First, the 0.5 wt.% CNF/epoxy samples are considered. Images of the three failed samples can be found in Figure 5.1. More close up images of the three failure sites of the samples (around the hole) can be noted in Figure 5.2.
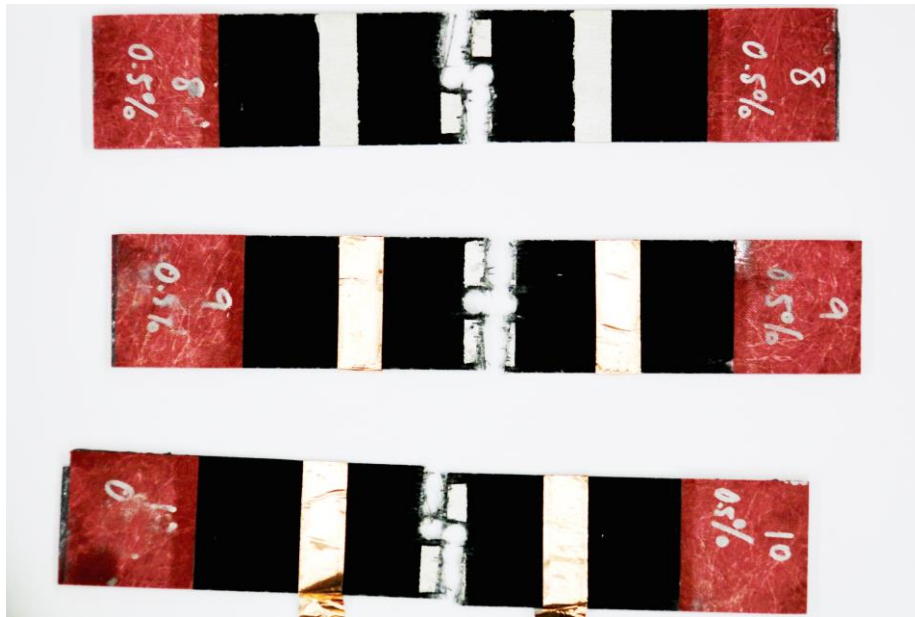


**Figure 5.1:** GFRC with CNF-modified epoxy added at 0.5 wt.%. Sample 1 is the bottom-most sample (labeled 10), while samples 2 and 3 are the top and middle (labeled 8 and 9) in this image.
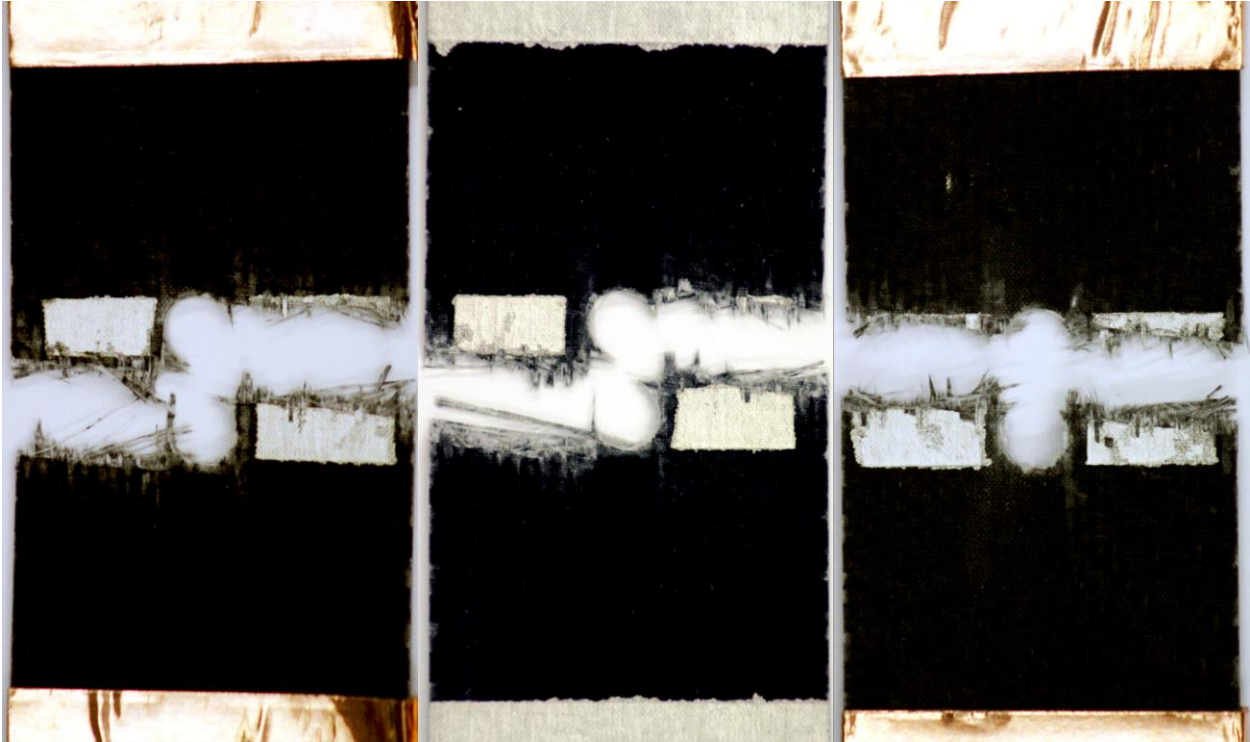
**Figure 5.2:** Close-up image of the 0.5 wt.% CNF sample failure region (around the hole). Samples 1, 2, and 3 can be found going from left to right.

The three 0.5 wt.% CNF samples 1, 2, and 3 failed after 178,279, 66,898, and 83,843 cycles respectively. The first observation made from these samples is that the samples 1 and 2 failed in similar manners. On the other hand, sample 3 failed in one transverse path to the load direction. In Sample 2, a fiber bundle can be seen separated from the weave; whereas sample 1 and sample 2 have fairly similar fracture surfaces. In every failure scenario, the copper tape detached.

Next, the 1.0 wt.% CNF/epoxy samples are considered. Images of the three failed samples can be found in Figure 5.3. More close up images of the three failure sites of the samples can be noted in Figure 5.4.

**Figure 5.3:** GFRC with CNF-modified epoxy added at 1.0 wt.%. Sample 1, 2, and 3 are labeled 10, 12, and 14 respectively.
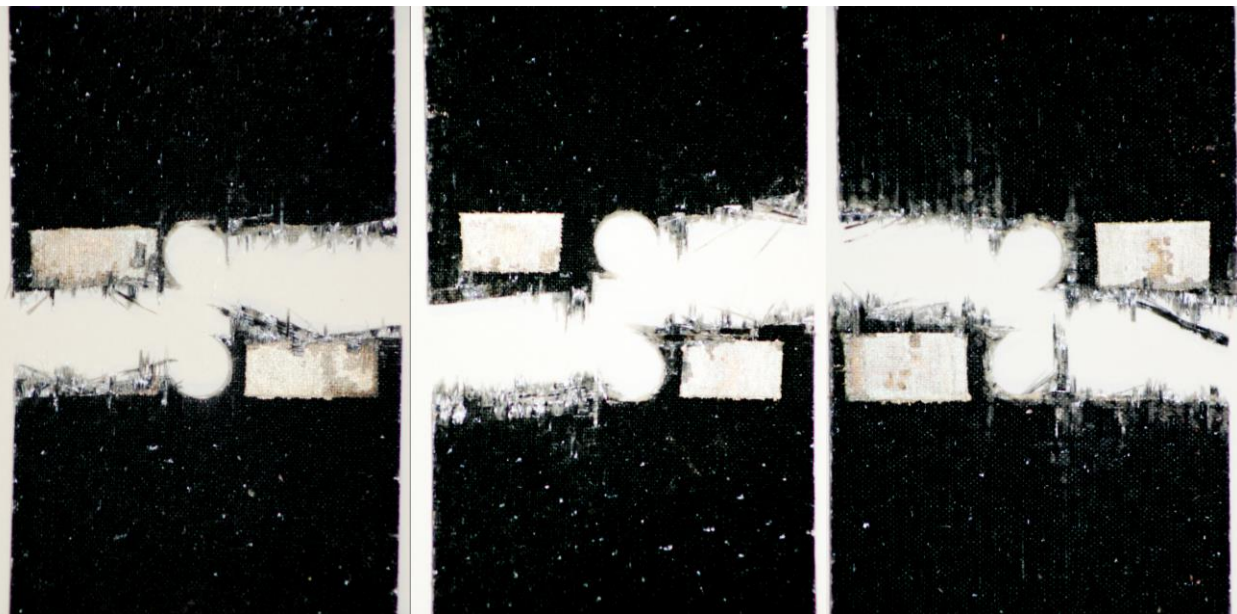


**Figure 5.4:** Close-up image of the 1.0 wt.% CNF sample failure region (around the hole). Samples 1, 2, and 3 can be found going from left to right.

The three 1.0 wt.% CNF samples 1, 2, and 3 failed after 114,600, 147,744, and 84,718 cycles respectively. The post-failure images for all three specimens look similar. A transverse fiber bundle is present in sample 3. As well, in sample 3 an axial fiber bundle remains on the bottom half, likely pulled out from the line adjacent to the hole present right of the hole on the top part.

Finally, the 1.5 wt.% CNF/epoxy samples are considered. Images of the three failed samples can be found in Figure 5.5. More close up images of the three failure sites of the samples can be noted in Figure 5.6.
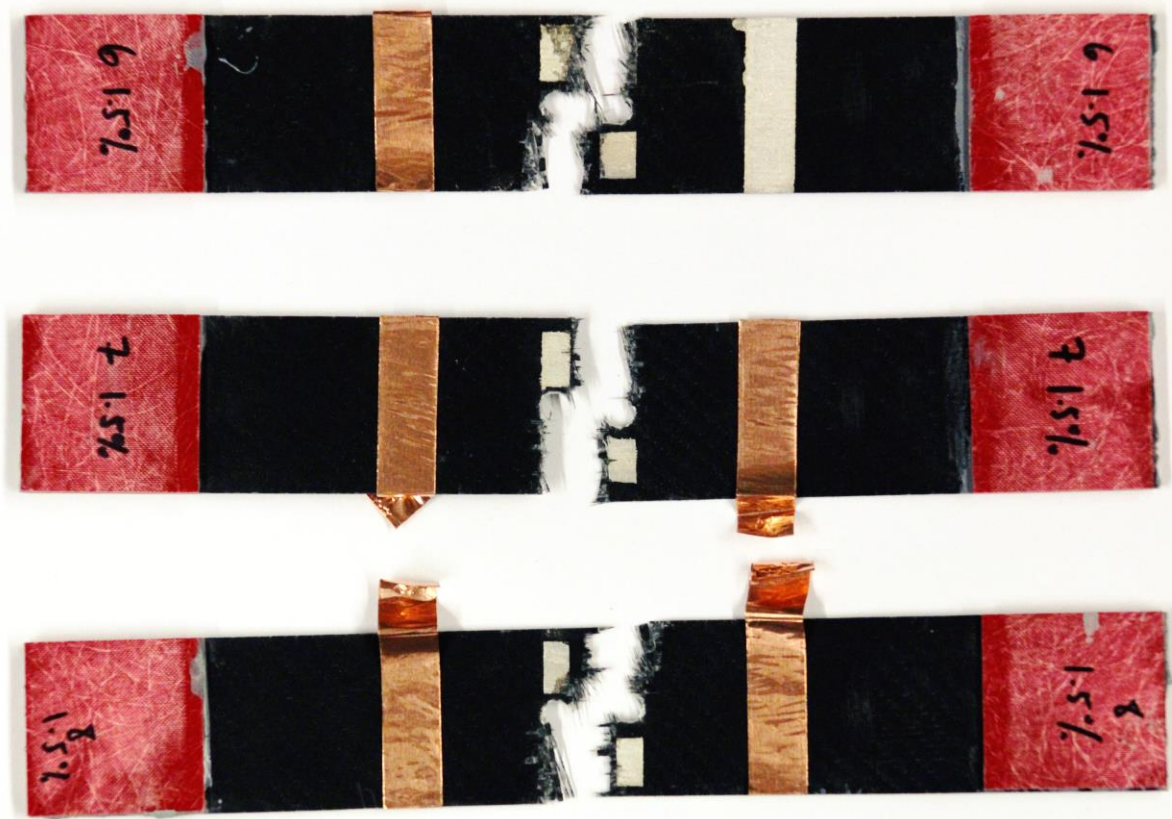


**Figure 5.5:** GFRC with CNF-modified epoxy added at 1.5 wt.%. Sample 1, 2, and 3 are labeled 6, 7, and 8 respectively.
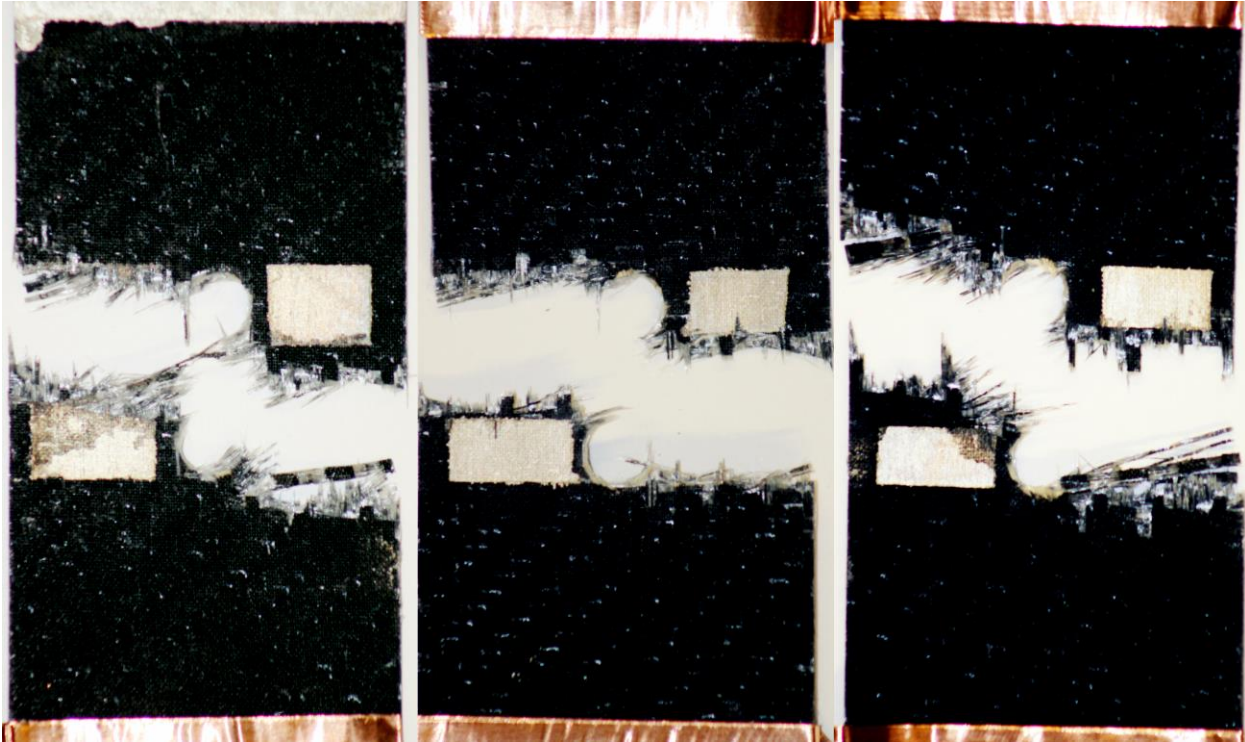
**Figure 5.6:** Close-up image of the 1.5 wt.% CNF sample failure region (around the hole). Samples 1, 2, and 3 can be found going from left to right.

The three 1.5 wt.% CNF samples 1, 2, and 3 failed after 76,346, 92,307, and 141,187 cycles respectively. All three samples appear to have the same post-failure pattern. Samples 1 and 3 failed nearly identically. There are transverse fiber bundles present in both samples 1 and 3. Samples 1 and 3 also seem to have failed 'explosively' as there are many frayed fibers; there is no clear transverse crack path in these failure surfaces. Sample 2 is consistent with previous radially symmetrically failed samples. Interestingly, the post-failure images of 8 out of 9 samples seem to show breakage at the upper and lower $45^o$ points of the hole while the only one showed breakage at both upper $45^o$ points. The cracks in all situations appear to propagate transverse to the load.

### 5.1.2 Stiffness versus Cycle

Stiffness was measured throughout the cycle of the specimens. The elastic modulus was found using the linear region of the stress-strain relationship using the pristine cross-sectional area as per the ASTM standard. The average initial elastic modulus for all of the samples was found to

be 22.73 GPa. The stiffness versus cycle can be found in Figure 5.7. The stiffness data at various stages in the specimen lifetime, as well as percent differences, are tabulated in Table 5.1.
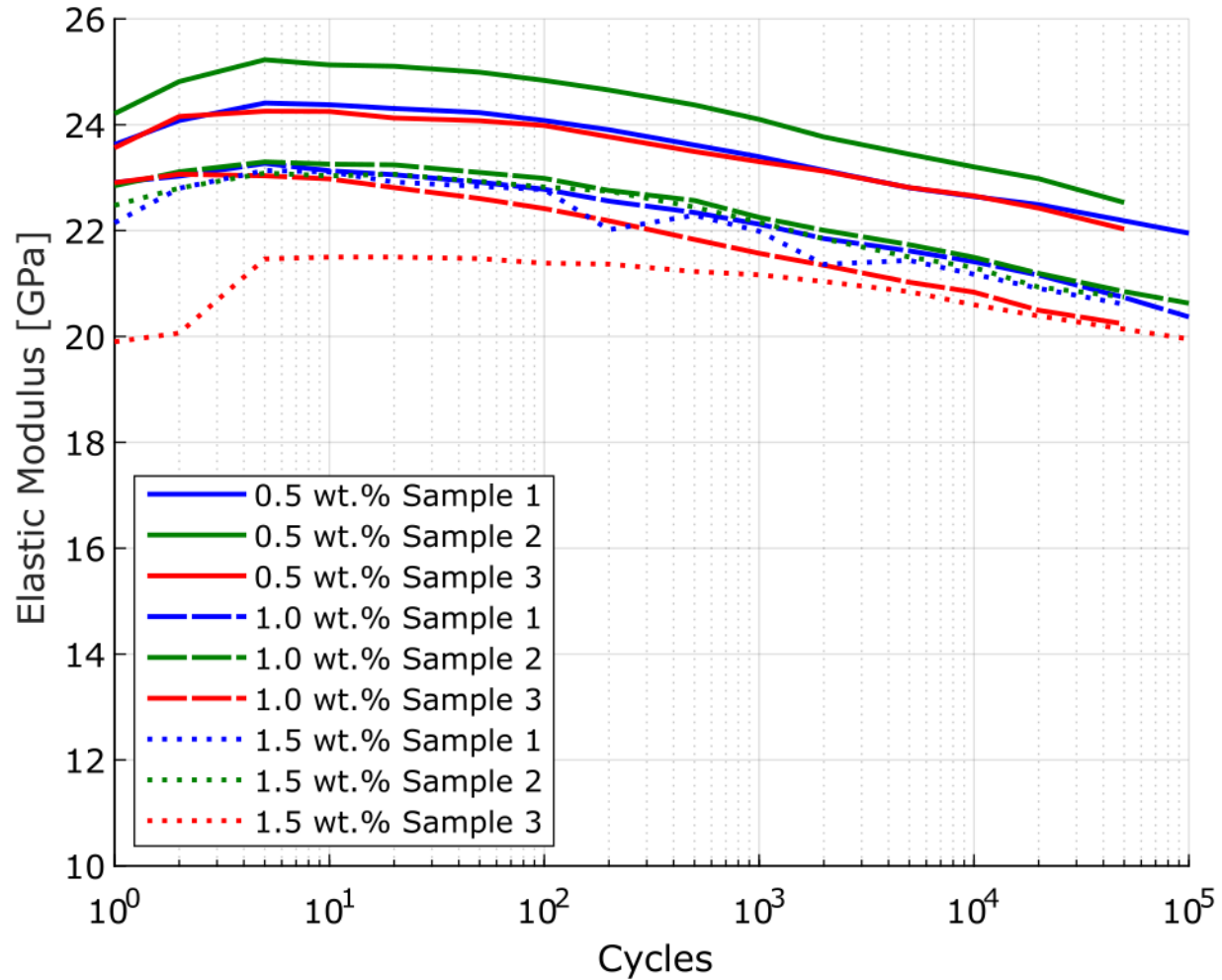


**Figure 5.7:** In this plot stiffness versus the number of tension cycles is shown. The nine samples follow similar trends in their elastic moduli data. The moduli begin at 22.73 GPa and fail around 21.01 GPa. Initial stiffening occurs up to 5 cycles. After the 5$^{th}$ cycle, there is a consistent stiffness drop over the sample lifetime.

**Table 5.1:** Initial elastic modulus, maximum elastic modulus, and final elastic measured elastic modulus are presented here. The percent differences between final modulus relative to initial modulus as well as percent differences between final modulus relative to maximum modulus are included.

| | | $E^{initial}$ [GPa] | $E^{max}$ [GPa] | $E^{final}$ [GPa] | $E^f$ & $E^i$ Difference | $E^f$ & $E^{max}$ Difference |
|---|---|---|---|---|---|---|
| 0.5 wt.% | 1 | 23.63 | 24.41 | 21.95 | 7.359% | 10.61% |
| | 2 | 24.21 | 25.23 | 22.53 | 7.189% | 11.30% |
| | 3 | 23.56 | 24.26 | 22.03 | 6.736% | 9.622% |
| 1.0 wt.% | 1 | 22.91 | 23.27 | 20.37 | 11.73% | 13.29% |
| | 2 | 22.85 | 23.30 | 20.63 | 10.21% | 12.15% |
| | 3 | 22.91 | 23.06 | 20.24 | 12.38% | 13.06% |
| 1.5 wt.% | 1 | 22.15 | 23.14 | 20.61 | 7.192% | 11.55% |
| | 2 | 22.48 | 23.09 | 20.75 | 8.001% | 10.67% |
| | 3 | 19.90 | 21.50 | 19.95 | -0.2616% | 7.470% |
| **Average** | | **22.73** | **23.47** | **21.01** | **7.836%** | **11.08%** |

The stiffness percent difference from initial to final elastic modulus is about 8% while the difference between maximum modulus and final modulus is about 11%. The stiffness drop would be far more substantial it was measured right before failure; for the fatigue of open-hole fiber-reinforced composites, stiffness drops of up to 65% occur during the onset of failure when loaded at 50% of UTS [62].

This stiffening in the GFRC with CNF-modified epoxy material is curious. This is hypothesized to be a consequence of the imprecise nature of manufacturing via hand layup. That is, glass fibers are not perfectly straight or not perfectly aligned with the loading direction after manufacturing. The first few load cycles act to 'straighten' these fibers thereby causing an initial stiffening effect. However, it is emphasized that this is only a hypothesis and was not tested in this work.

## 5.2 DC Response versus Cycle

In addition to AC, DC resistance was measured during the loading history. The DC response data is normalized for each of the weight percentages to observe trends within each weight fraction relative to other datasets. The initial DC resistance is tabulated in Table 5.2. The normalized DC resistance versus cycle plots for the 0.5 wt.%, 1.0 wt.%, and 1.5 wt.% CNF samples can be found in Figure 5.8, Figure 5.9, and Figure 5.10 respectively.

**Table 5.2:** Initial DC resistance values for the following normalized DC response plots.

| | | Length 1 [$\Omega$] | Through-Thickness 2 [$\Omega$] | Through-Thickness 3 [$\Omega$] |
|---|---|---|---|---|
| 0.5 wt.% | Sample 1 | 1.539E+06 | 1.029E+06 | 1.026E+07 |
| | Sample 2 | 2.017E+05 | 1.186E+07 | 8.304E+05 |
| | Sample 3 | 53,050 | 1.689E+05 | 49,370 |
| 1.0 wt.% | Sample 1 | 1,618 | 7,502 | 2,563 |
| | Sample 2 | 2,246 | 15,320 | 14,100 |
| | Sample 3 | 8,175 | 3,822 | 7,381 |
| 1.5 wt.% | Sample 1 | 604.0 | 1,015 | 492.0 |
| | Sample 2 | 1451 | 678.1 | 1492 |
| | Sample 3 | 483.3 | 393.5 | 244.6 |
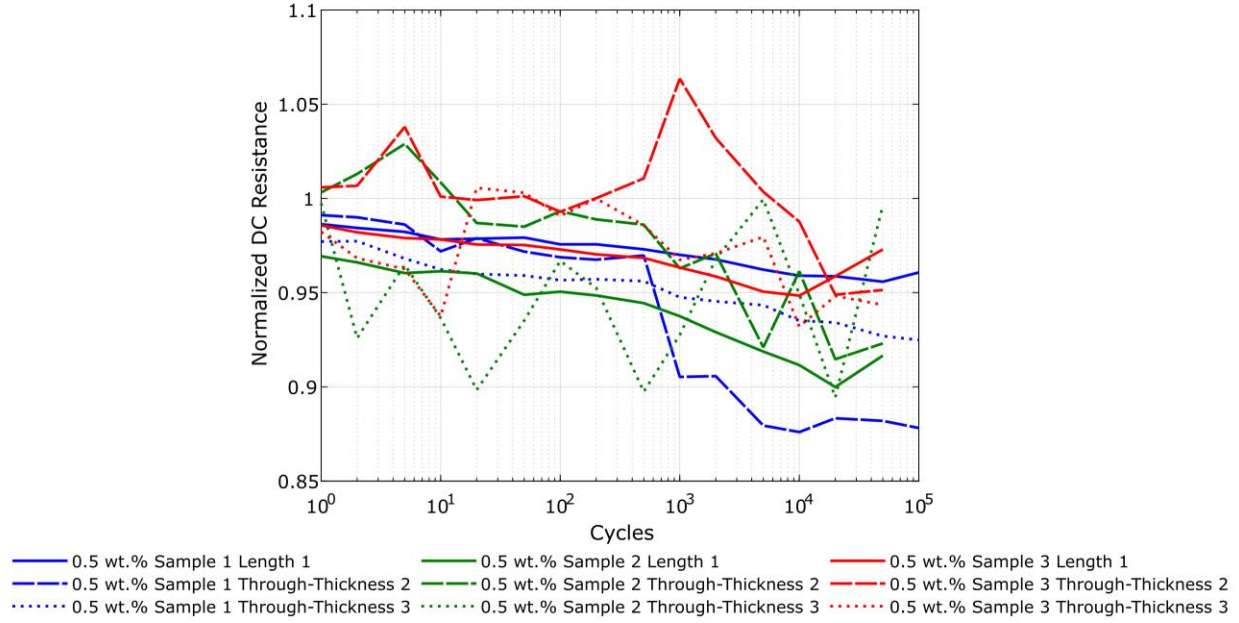
**Figure 5.8:** DC normalized response for the 0.5 wt.% CNF-modified epoxy GFRC specimens. Note that the plotting begins at cycle 1 (cycle 0 is 1.0 for every data point).

In Table 5.2 the 0.5 wt.% CNF specimens have substantially higher initial DC resistance values relative to the other two weight fractions in all interrogation directions – this resistance is one to three orders of magnitude larger than the 1.0 wt.% and 1.5 wt.% CNF values. In Figure 5.8, there is a consistent decreasing trend in the DC response. Viets et al. showed in a low weight percentage (0.3 wt.%) CNT-modified GFRC specimen in impact testing compressive deformation of a percolated particle network resulted in a decrease in electrical resistance characterized by plastic surface deformation; in a higher weight fraction (CB and CNT) the impact testing resulted in an increase in electrical resistance due to matrix cracking [27]. Loyola et al. also demonstrated decreasing resistance in incremental step-tensile loading of MWCNT-modified GFRC specimens due to increasing laminate thickness [56]. Damage severs the nanofiller network causing an increase in resistance; compressive strains result in a decrease in resistance. It is speculated that at the lower weight fraction the compressive strain effect is more pronounced than nanofiller network severance. As the 0.5 wt.% CNF samples near failure their DC resistance drops. There is no substantial drop except in sample 1 through-thickness 2. Next, sample 3 through-thickness 2 provides an ambiguous response with two peaks and on valley present in the line before dropping at the end. The data is fairly noisy overall speaking to the

minimal CNFs present in the material. With small amounts of CNFs, the network has poor connectivity and hence large resistance and susceptibility to noise.
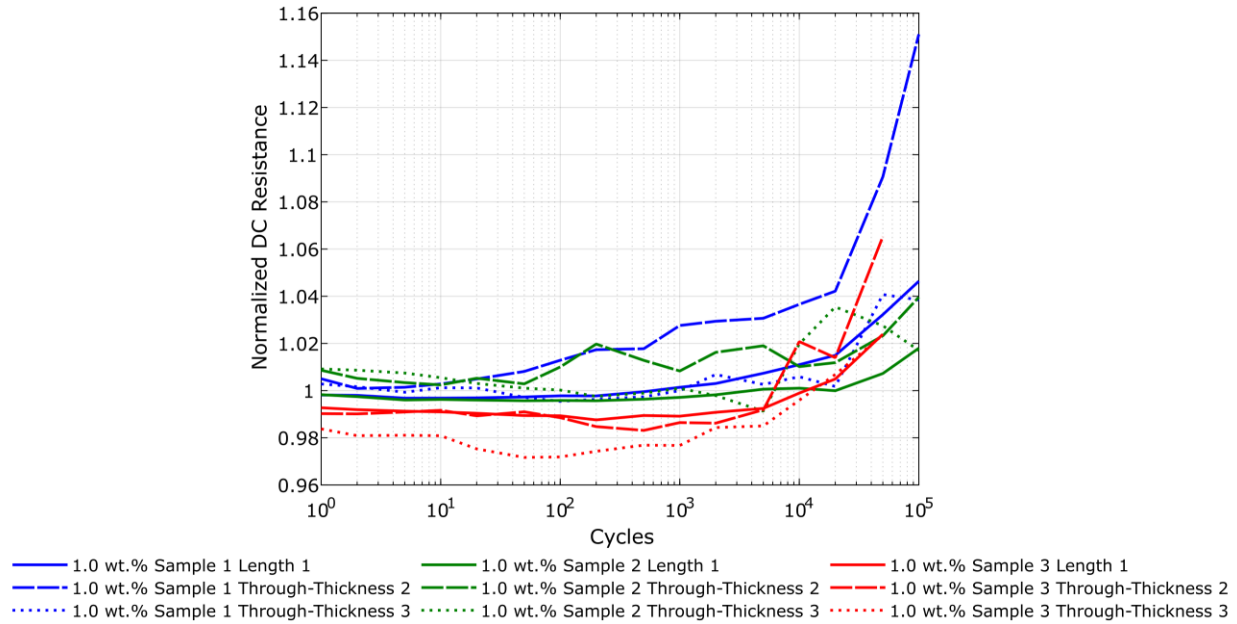


**Figure 5.9:** DC normalized response for the 1.0 wt.% CNF-modified epoxy GFRC specimens. Note that the plotting begins at cycle 1.

Unlike the 0.5 wt.% CNF values where DC resistance gradually decreased, Figure 5.9 shows an increase in DC resistance with increasing fatigue for the 1.0 wt.% CNF specimens. This is most notable in sample 1 through-thickness 2 with a nearly exponential curve present in the DC resistance. Another notable exponential curve is in the specimen 3 length 1 direction. In this plot, there is a consistent increase in DC resistance for all specimens in all three interrogation directions. Furthermore, compared to the 0.5 wt.% CNF data which was quite noisy, this data is rather orderly.
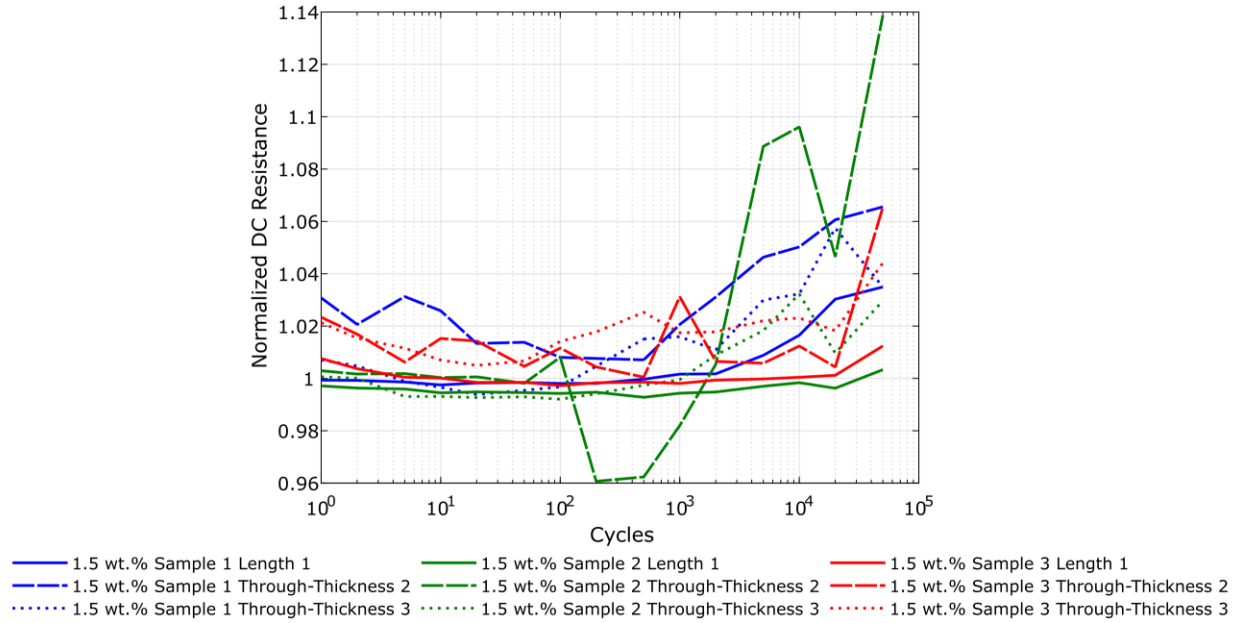
**Figure 5.10:** DC normalized response for the 1.5 wt.% CNF-modified epoxy GFRC specimens. Note that the plotting begins at cycle 1.

The DC resistance response for the 1.5 wt.% CNF data is shown here in Figure 5.10. First off, this DC response shows similar trends to the data shown in Figure 5.9 in that the DC resistance generally increases with increasing cycles. However, an interesting feature of many of the lines is that they are fairly noisy early in the fatigue cycle, but then around the $500^{th}$ cycle increase continuously, e.g. sample 1 through-thickness 2. It is interesting to note in specimen 2 through-thickness 2 the DC response goes through multiple peaks and valleys before reaching a relative value higher than any other DC resistance recorded.

### 5.3 EIS Data versus Cycle

We next consider the AC data. This is first explored through electrical impedance spectroscopy (EIS) analysis. EIS plots are Nyquist plots, parametric relationships of interrogation frequency, with the real part of impedance on the *x*-axis and negative the imaginary part plotted on the *y*-axis. EIS plots allow for easy visualization of how real and complex impedance relate to one another as functions of frequency. For the GFRC with CNF-modified epoxy materials, these plots most often take the form of semicircles with the lowest frequency at the right end and the highest frequency at the left end. These arcs as a function of cycle for the three specimens and three measurement locations for the 0.5 wt.% CNF samples can be seen in Figure 5.11.
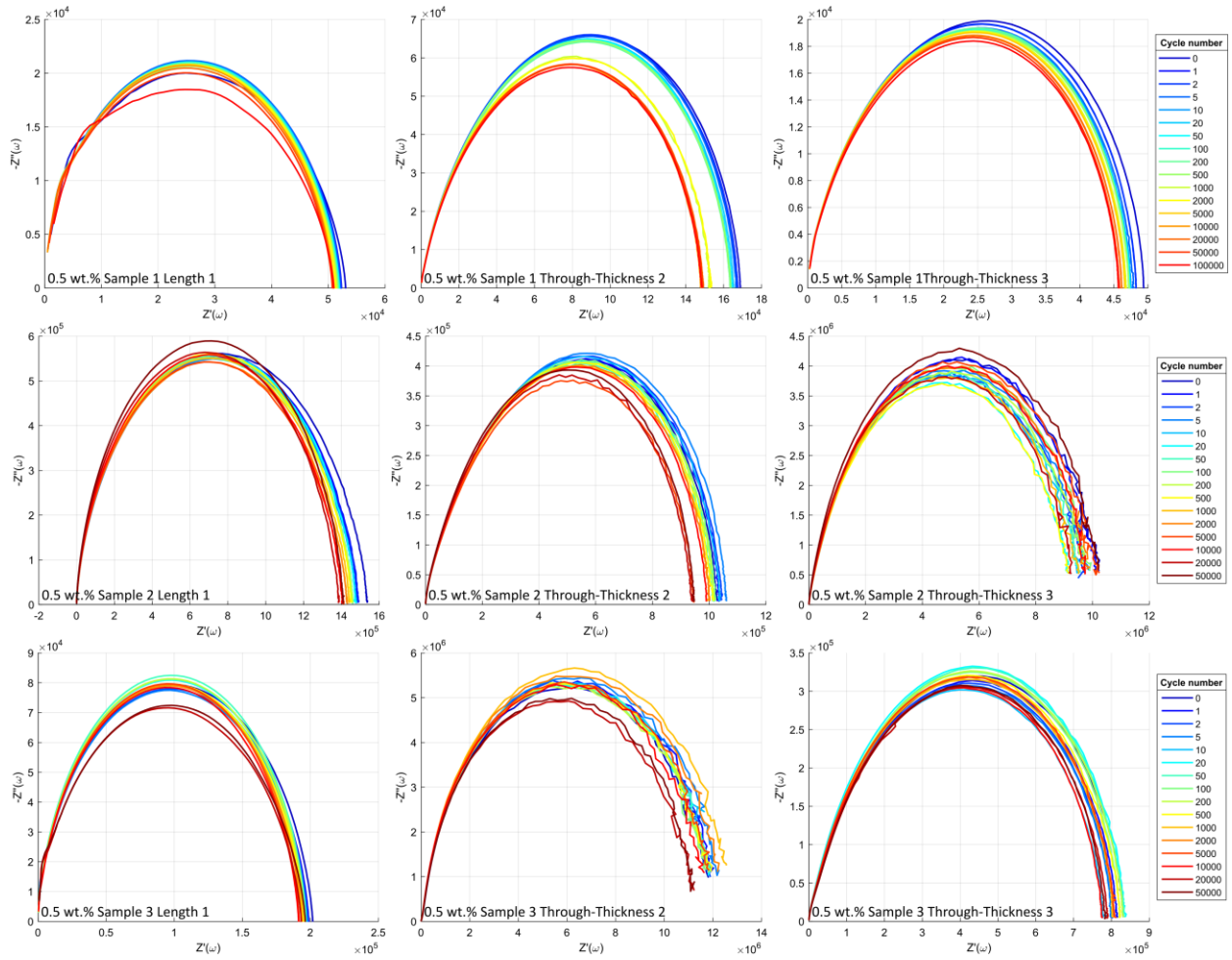
**Figure 5.11:** EIS data for the 0.5 wt.% CNF samples and three interrogation directions. From top-to-bottom, each row corresponds to each one of the three test specimens.

These arcs have some notable characteristics. For one, there seems to be inherent noise present in some of the arcs, e.g. in sample 2 through-thickness 3 and sample 3 through-thickness 2 low-frequency data. Secondly, note that with increasing cycle there seems to be both a decreasing real and imaginary part; meaning the whole arc shifts down and left, becoming smaller with increasing damage. Lastly, the decreasing real component of the impedance as a function of the cycle is indicative of the DC response of the material, verified via Figure 5.8.

With increasing CNF weight fraction, the resulting EIS arcs demonstrate inherently different results. These arcs as a function of cycle for the three specimens and three measurement locations for the 1.0 wt.% CNF samples can be seen in Figure 5.12.
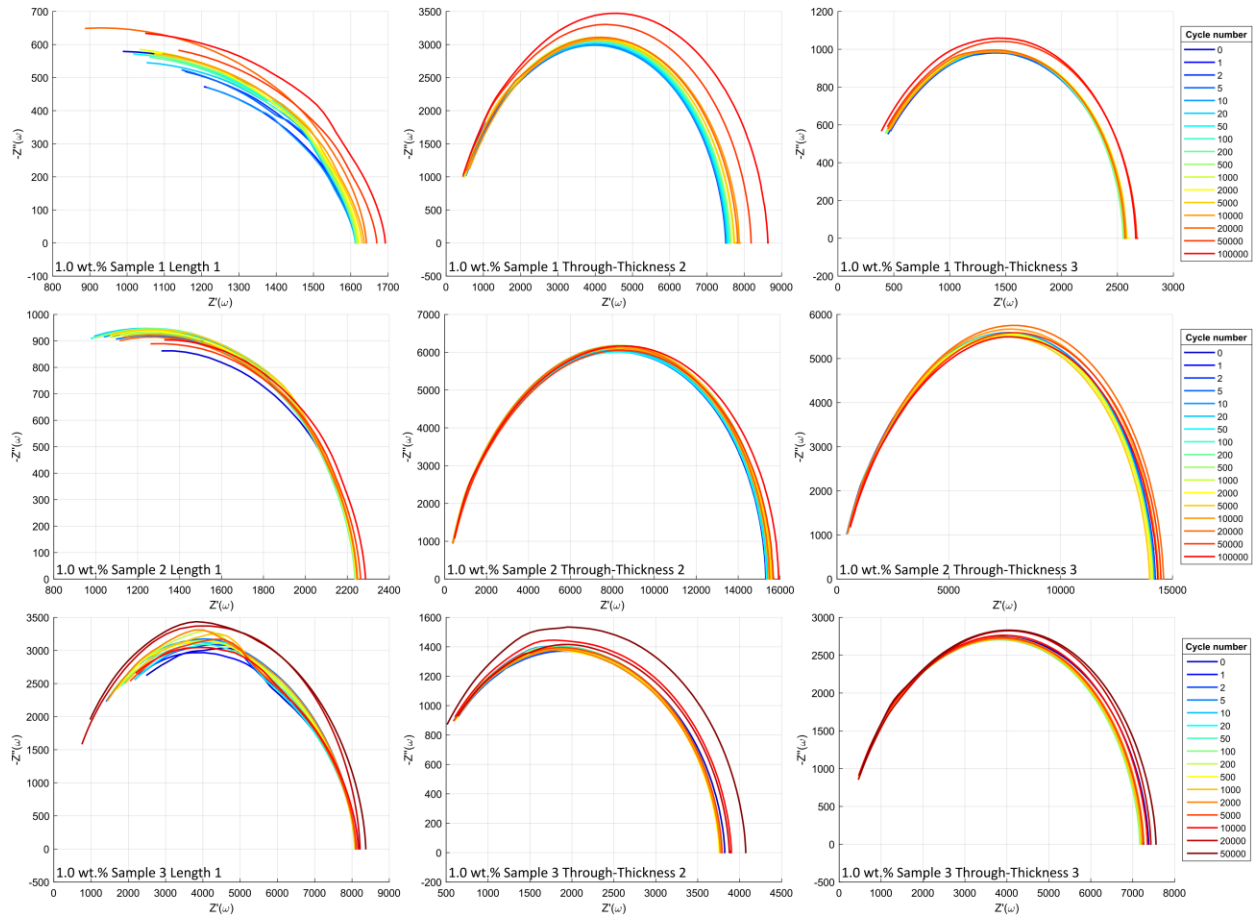


**Figure 5.12:** EIS data for the 1.0 wt.% CNF samples and three interrogation directions. From top-to-bottom, each row corresponds to each one of the three test specimens.

Here, in samples 1 and 3 there is a consistent shift in the positive *x*-direction and the negative *y*-direction. Notice how at higher cycles the arcs shift up and right, opposite the direction of the 0.5 wt.% CNF samples. Next, with sample 2 the same trend of a larger real component of impedance is present with increasing cycles; however, in sample 2 length 1 the imaginary part is more ambiguous in how it changes. Lastly, the real part of the 1.0 wt.% CNF samples increases as a function of cycles (and fatigue damage), similar to the Figure 5.9 data.

With further increasing weight fraction of CNF the resulting EIS arcs demonstrate further different results. These arcs as a function of cycle for the three specimens and three measurement locations for the 1.5 wt.% CNF samples can be seen in Figure 5.13.
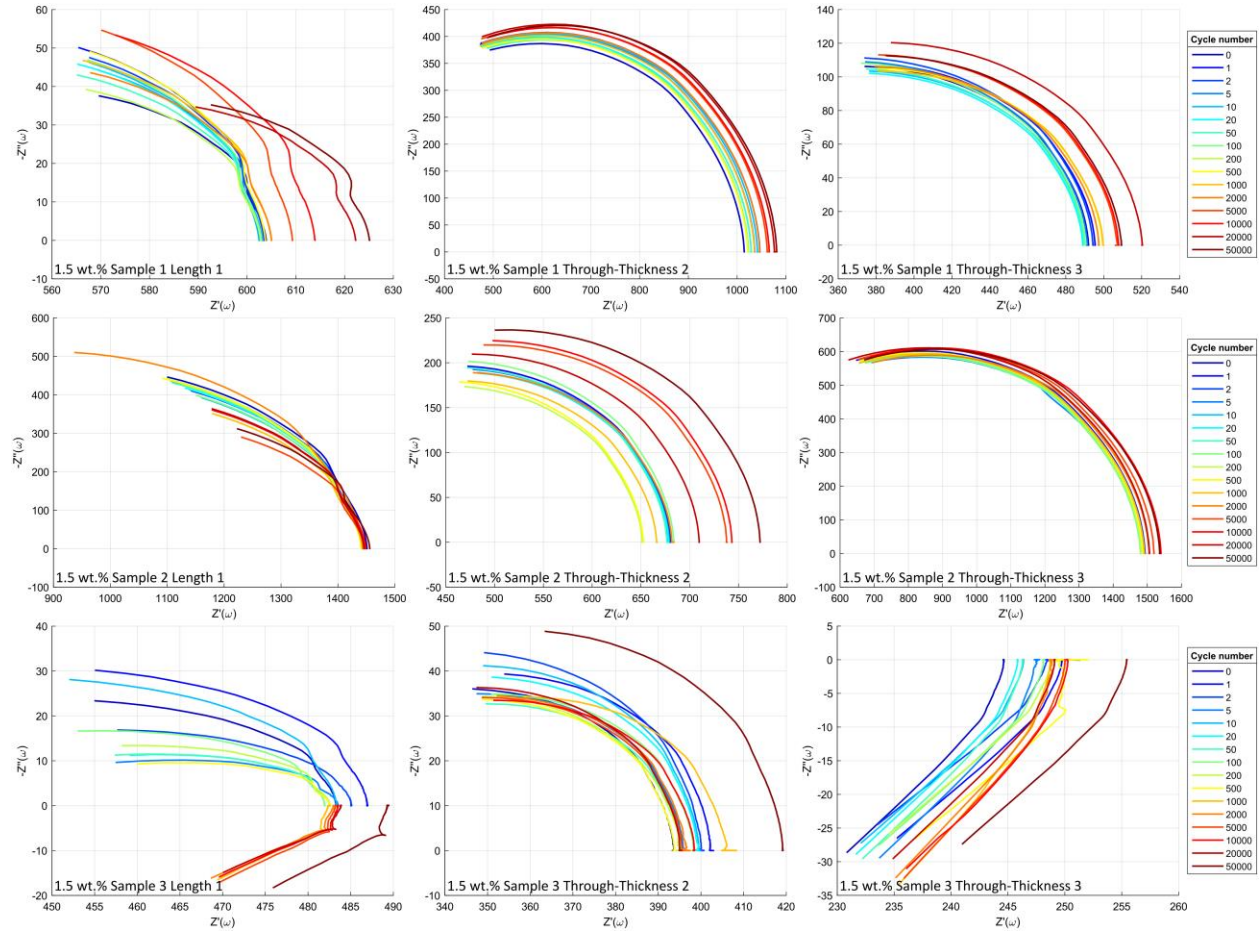


**Figure 5.13:** EIS data for the 1.5 wt.% CNF samples and three interrogation directions. From top-to-bottom, each row corresponds to each one of the three test specimens.

The major observation with these plots is that with increasing cycle there tends to be an increasing real-part and decreasing imaginary-part of impedance similar to the 1.0 wt.% CNF samples. However, this trend is only consistent for the two through-thickness directions. Though in some cases, the imaginary part is ambiguous, e.g. sample 3 through-thickness 2. Notice how at this weight percentage the arc substantially decreases in its breadth. This is an observation that has been made, with higher weight fractions the completeness of the EIS arc shortens [28]. As well, note that in sample 1 length 1 there is a consistent increase in the real and imaginary parts

of complex impedance up till the 20,000$^{th}$ cycle where the last two measurements have much smaller maximum imaginary components of impedance. This same observation can be made for sample 2.

What is most interesting in these EIS plots is sample 3: after the 500$^{th}$ cycle, the imaginary part spans into the positive region for the length 1 direction and is fully positive in the through-thickness 3 direction. Even with this flip, the same observation of a smaller imaginary component (in magnitude) for the length 1 direction like in sample 1 is noted in sample 3. This may be a result of the higher number of CNFs in this material creating a different network of pathways in the material.

## 5.4 Equivalent Circuit Parameter versus Cycle

AC impedance equivalent circuit modeling is well established in literature [31] [35] [36] [37] [38] [56] [57] [58] [59]. The motivation is to establish a relationship between the progression of fatigue damage in the GFRC with CNF-modified epoxy material and a model's circuit parameters. Characterizing damage progression as a function of circuit parameters allows insight into how the pathways through the material change as damage accumulates. These parameters can consequently act as indicators of damage accumulation.

A circuit model for the GFRC with CNF-modified epoxy material was developed through a trial and error process. A key consideration of the circuit model is its capability of modeling the different EIS curves accurately. The EIS curves result in complete arcs (two *x*-intercepts), arcs with the right end above the *x*-axis, arcs with the left end above the *x*-axis, as well as curves where the imaginary component of complex impedance becomes positive.

The circuit model proposed for this material is akin to the circuit model presented by Song with an analogous system of micropore junctions in cementitious materials to the nanofiller networks in polymer mediums in this study [57]. Composite materials with nanofiller-modified polymers always make use of a parallel resistor-capacitor in the circuit to model the semicircular behavior present in the EIS data [31] [35] [36] [39]. Including a series resistor is an important addition. The left *x*-intercept of the EIS curve defines the series resistor which represents the bulk

resistance of the material [56]. The bulk inductor was included to better fit the data considering, especially at higher weight fractions, some inductance is present in the materials indicated by positive imaginary portions of impedance. The circuit model derived can be noted in Figure 5.14. The associated real and imaginary impedance relations are described in equations (5.1) and (5.2) where $\omega$ is the angular frequency.
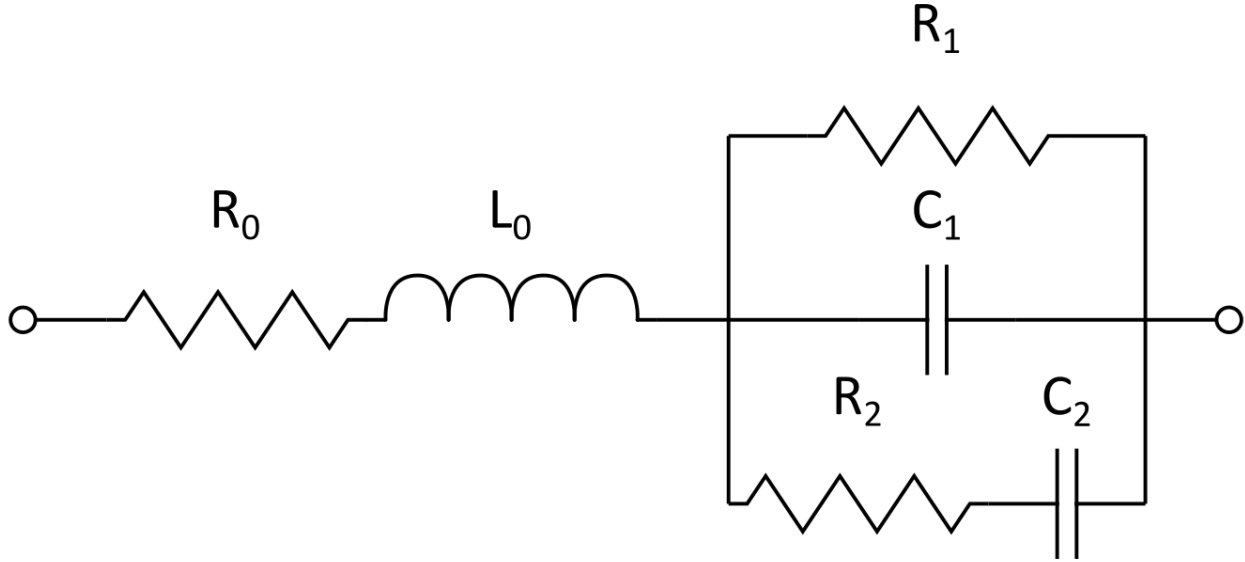


**Figure 5.14:** Equivalent circuit model developed for modeling GFRC with CNF-modified epoxy at the three weight fractions. The circuit is composed of six elements: a series resistor $R_0$, series inductor $L_0$, followed by a parallel portion with a single resistor $R_1$ path, single capacitor $C_1$ path, and a resistor and capacitor in series, $R_2$ and $C_2$. This circuit consists of three frequency-independent elements and three frequency-dependent elements.

$$Z'(\omega) = R_0 + \frac{R_1[(\omega C_2 R_2)^2 + R_1(\omega C_2 R_2)^2 + 1]}{\left[\begin{array}{c}(\omega^2 C_1 C_2 R_1 R_2)^2 + (\omega C_1 R_1)^2 + 2C_1 C_2(\omega R_1)^2 + \\ (\omega C_2 R_1)^2 + 2R_1 R_2(\omega C_2)^2 + (\omega C_2 R_2)^2 + 1\end{array}\right]} \tag{5.1}$$

$$Z''(\omega) = \omega L_0 - \frac{\omega R_1{}^2[C_1(\omega C_2 R_2)^2 + C_1 + C_2]}{\left[\begin{array}{c}(\omega^2 C_1 C_2 R_1 R_2)^2 + (\omega C_1 R_1)^2 + 2C_1 C_2(\omega R_1)^2 + \\ (\omega C_2 R_1)^2 + 2R_1 R_2(\omega C_2)^2 + (\omega C_2 R_2)^2 + 1\end{array}\right]} \tag{5.2}$$

As previously discussed, AC transport is a consequence of the nanofiller network. The CNF-modified epoxy presents an inherent bulk resistance and inductance which is why every interrogation flows through the series resistor $R_0$ and series inductor $L_0$. Following this direction,

the circuit model needs to represent the three major paths through the network: a continuous conductive path, a discontinuous conductive path, and an insulating path. The continuous path of impedance flows through the single resistor, $R_1$. In the instance that the current runs through predominantly capacitive regions (e.g. path dominated by inter-CNF capacitance) the current flows through the single capacitor, $C_1$. The discontinuous conductive path in the material is the pathway through the material that flows through the resistor and capacitor in series, $R_2$ and $C_2$.

The curve fitting was performed using MATLAB's simulated annealing optimization toolbox. Example fits and the normalized $L^1$ norm results between the model and the actual data can be noted in Figure 5.15. This error plot includes an example 'bad' fit (i.e. having a higher normalized error) that demonstrates even these 'bad' fits match their respective data quite well.



| | | |
|---|---|---|
| O | 0.5 wt.% Sample 1 Length 1 | + 1.0 wt.% Sample 1 Length 1 | ✳ 1.5 wt.% Sample 1 Length 1 |
| ✕ | 0.5 wt.% Sample 1 Through-Thickness 2 | ★ 1.0 wt.% Sample 1 Through-Thickness 2 | □ 1.5 wt.% Sample 1 Through-Thickness 2 |
| △ | 0.5 wt.% Sample 1 Through-Thickness 3 | ◇ 1.0 wt.% Sample 1 Through-Thickness 3 | ✮ 1.5 wt.% Sample 1 Through-Thickness 3 |
| O | 0.5 wt.% Sample 2 Length 1 | + 1.0 wt.% Sample 2 Length 1 | ✳ 1.5 wt.% Sample 2 Length 1 |
| ✕ | 0.5 wt.% Sample 2 Through-Thickness 2 | ★ 1.0 wt.% Sample 2 Through-Thickness 2 | □ 1.5 wt.% Sample 2 Through-Thickness 2 |
| △ | 0.5 wt.% Sample 2 Through-Thickness 3 | ◇ 1.0 wt.% Sample 2 Through-Thickness 3 | ✮ 1.5 wt.% Sample 2 Through-Thickness 3 |
| O | 0.5 wt.% Sample 3 Length 1 | + 1.0 wt.% Sample 3 Length 1 | ✳ 1.5 wt.% Sample 3 Length 1 |
| ✕ | 0.5 wt.% Sample 3 Through-Thickness 2 | ★ 1.0 wt.% Sample 3 Through-Thickness 2 | □ 1.5 wt.% Sample 3 Through-Thickness 2 |
| △ | 0.5 wt.% Sample 3 Through-Thickness 3 | ◇ 1.0 wt.% Sample 3 Through-Thickness 3 | ✮ 1.5 wt.% Sample 3 Through-Thickness 3 |

**Figure 5.15:** Simulated annealing fit results; plotted are the normalized (relative to the cycle 0 fit) $L^1$ norm data. The first norm value difference is found between the experimental and simulated impedance data as a function of experimental frequency. The range is a result of the different values of maximum and minimum of the real and imaginary parts of impedance as well as the completeness of the arcs. A 'good' fit (green) and a 'bad' fit (pink) can be noted on the right side of the figure. Even 'bad' fits still match the data quite well.

To monitor fatigue's impact on the equivalent circuit parameters across different interrogation paths and samples, normalized circuit parameters are plotted as a function of the cycle. The 0.5 wt.% CNF circuit parameters can be noted in Figure 5.16. The initial values for all six of the circuit parameters are tabulated in Table 5.3.
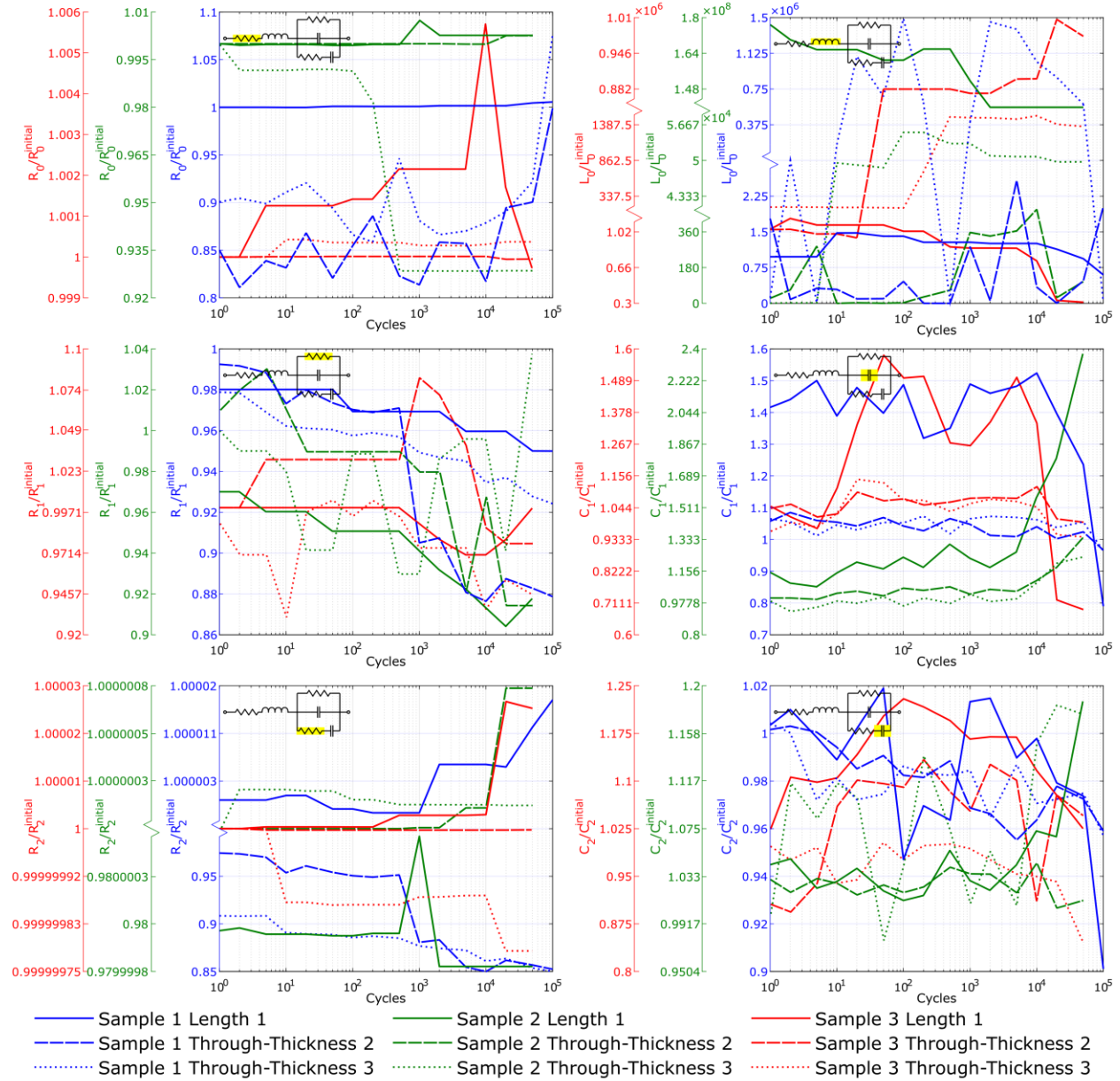


**Figure 5.16:** Normalized circuit parameters versus cycles for 0.5 wt.% CNF samples plotted beginning at cycle 1 (cycle 0 is 1.0 for every data point). Each of the six plots directly associates with the six circuit parameters. On the left side are the three frequency-independent resistors in

the circuit while on the right side or the frequency-dependent elements. The upper right is the inductor while the middle and bottom right are the two capacitors.

**Table 5.3:** This table contains the initial circuit parameters that result from the curve fitting process. 1, 2, and 3 refer to the directions length 1, through-thickness 2, and through-thickness 3. These values serve as the initial values for the normalized data present in Figure 5.16.

| | | $R_0$ [$\Omega$] | $L_0$ [$H$] | $R_1$ [$\Omega$] | $C_1$ [$F$] | $R_2$ [$\Omega$] | $C_2$ [$F$] |
|---|---|---|---|---|---|---|---|
| Sample 1 | 1 | 742.3 | 1.930E-05 | 5.230E+04 | 3.339E-12 | 1.674E+04 | 2.748E-12 |
| | 2 | 406.3 | 6.969E-13 | 1.681E+05 | 1.754E-11 | 1.681E+05 | 1.698E-11 |
| | 3 | 359.0 | 8.038E-13 | 4.896E+04 | 1.164E-11 | 4.896E+04 | 9.150E-12 |
| Sample 2 | 1 | 215.5 | 4.463E-15 | 1.531E+06 | 3.605E-12 | 3.062E+06 | 3.642E-12 |
| | 2 | 285.2 | 1.891E-14 | 1.029E+06 | 1.716E-11 | 1.020E+06 | 1.549E-11 |
| | 3 | 221.5 | 1.161E-11 | 9.596E+06 | 1.835E-11 | 9.960E+06 | 1.217E-11 |
| Sample 3 | 1 | 467.4 | 2.115E-05 | 1.958E+05 | 3.844E-12 | 4.426E+05 | 2.412E-12 |
| | 2 | 359.3 | 3.156E-10 | 1.132E+07 | 3.369E-11 | 1.078E+07 | 1.331E-11 |
| | 3 | 233.1 | 6.827E-10 | 8.241E+05 | 2.497E-11 | 1.649E+06 | 1.918E-11 |

From Figure 5.16, the 0.5 wt.% CNF specimens show notable characteristics in the circuit parameters as a function of fatigue. Most notably, the series resistor, $R_0$, shows a general increase with cycle. However, in specimen 2 through-thickness 3 there is an appreciable drop in resistance with cycles. As well, the lone resistor in the parallel portion of the circuit, $R_1$, shows a decline in its resistance as fatigue damage builds in the material. The series parallel resistor, $R_2$, shows an ambiguous change as cycles increase; it increases in cases like sample 1 length 1 and sample 3 length 1 but decreases in instances like sample 1 through-thickness 2 and sample 3 through-thickness 3. Mostly, $R_2$ holds fairly constant throughout loading for all three samples. Interestingly, amongst all of the resistors, there is a spike around the 10,000[th] cycle possibly suggesting that this is when sizable macroscale damage formed. An interesting note is that the sample 1 through-thickness 2 $R_2$ trend is identical to the sample 1 through-thickness 2 DC trend from Figure 5.8.

The frequency-dependent circuit parameters show even less consistency with the increasing cycle. Firstly, the inductor shows relative change with increasing cycles, but there is no consistency in how it does. It does change by many orders of magnitude throughout the sample lifetime. As well, the two capacitors show similar trends respective of one another. For example, samples 1, 2, and 3 length 1 for both capacitors show identical trends with increasing cycles respective of one another. However, this is less consistent for the through-thickness directions but can be noted in sample 1 through-thickness 3 and sample 3 through-thickness 3.

Table 5.3 has some notable characteristics. Most notable is that in all three samples, the parallel resistors ($R_1$ and $R_2$) and parallel capacitors ($C_1$ and $C_2$) all begin at the same order of magnitude. Furthermore, the most interesting aspect of the capacitors is that in both the lone capacitor, $C_1$, and the series parallel capacitor, $C_2$, the value of the length 1 direction is an order of magnitude smaller than the through-thickness 2 and 3 directions, i.e. $10^{-12}$ F versus $10^{-11}$ F. This speaks to the capacitive path through the materials. In the through-thickness direction, the two electrodes are exactly opposite one another on the material surfaces, so the two electrodes can be visualized as physical capacitors where the dielectric between them is the GFRC with CNF-modified epoxy itself. This results in more capacitive behavior through these interrogation directions because of electrode geometry.

Next, the 1.0 wt.% CNF-modified epoxy curve fits can be seen. The normalized circuit parameters versus cycle can be noted in Figure 5.17. The initial values outputted from the curve fitting process can be found tabulated in Table 5.4.
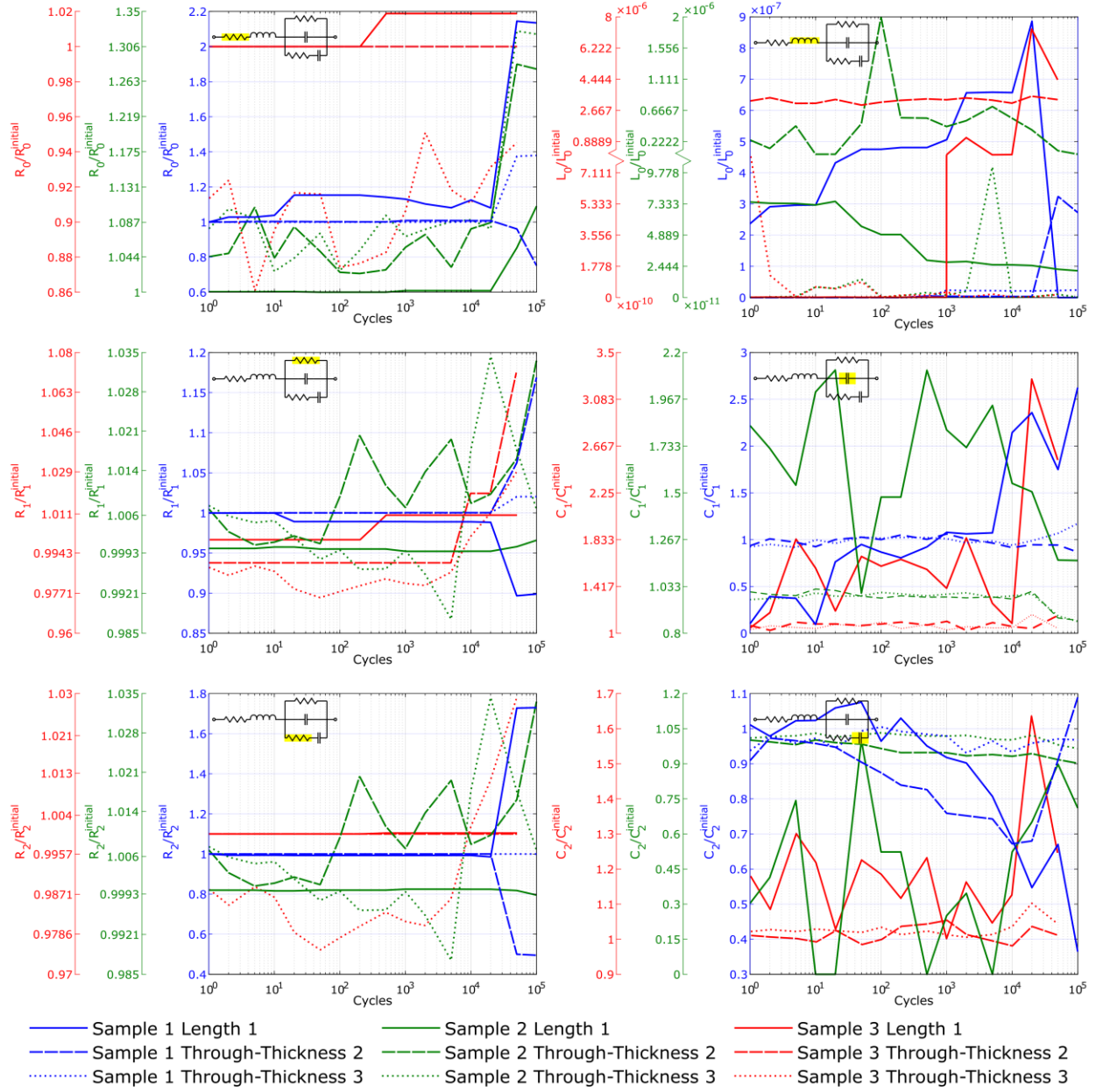
**Figure 5.17:** Normalized circuit parameters versus cycles for 1.0 wt.% CNF samples plotted beginning at cycle. Each of the six plots directly associates with the six circuit parameters.

**Table 5.4:** This table contains the initial circuit parameters that result from the curve fitting process. 1, 2, and 3 refer to the directions length 1, through-thickness 2, and through-thickness 3. These values serve as the initial values for the normalized data present in Figure 5.17.

| | | $R_0$ [$\Omega$] | $L_0$ [$H$] | $R_1$ [$\Omega$] | $C_1$ [$F$] | $R_2$ [$\Omega$] | $C_2$ [$F$] |
|---|---|---|---|---|---|---|---|
| Sample 1 | 1 | 168.6 | 2.369E-07 | 1,450 | 3.659E-12 | 1,006 | 6.220E-12 |
| | 2 | 435.2 | 2.740E-11 | 7,068 | 1.743E-11 | 24,030 | 7.948E-12 |
| | 3 | 197.2 | 6.457E-14 | 2,334 | 2.075E-11 | 3,780 | 1.059E-11 |
| Sample 2 | 1 | 357.2 | 5.459E-11 | 1,870 | 5.627E-12 | 1,769 | 2.927E-12 |
| | 2 | 366.9 | 2.169E-07 | 14,950 | 1.751E-11 | 14,950 | 1.404E-11 |
| | 3 | 443.1 | 1.554E-12 | 13,650 | 1.707E-11 | 13,650 | 1.285E-11 |
| Sample 3 | 1 | 42.95 | 3.391E-13 | 8,062 | 1.968E-12 | 7,839 | 2.793E-12 |
| | 2 | 0.3742 | 3.089E-06 | 3,795 | 1.111E-11 | 9,780 | 1.011E-11 |
| | 3 | 470.2 | 4.803E-10 | 6,912 | 1.568E-11 | 6,912 | 1.344E-11 |

From Figure 5.17, several interesting observations can be made. First off, $R_0$ demonstrates the most uniform trend where the resistance increases as the cycles increase. There is a notable spike between the 20,000[th] and 50,000[th] cycle, again likely indicative of substantial damage growth. Secondly, the $R_1$ value also generally increases throughout specimen lifetime. However, this trend is not as consistent as with the series resistor. There is a general increase in resistance with cycle number, but in some cases (e.g. sample 1 length 1) $R_1$ decreases. As well, sample 2 through-thickness 3 increases and then decreases again before failure. Lastly, $R_2$ demonstrates similar changes to $R_1$. Overall, $R_1$ and $R_2$ follow very similar trends for the three samples tested.

Unlike the resistive parts of the equivalent circuit (and similar to the 0.5 wt.% CNF samples), the frequency-dependent components showed a great deal of inconsistency. First off, $L_0$ shows a relative change to its initial parameters, but there is no agreement with how it changes. Next, consider $C_1$ and $C_2$; in some instances, they increase as the samples near failure and in some cases decrease near failure. The through-thickness capacitance values stay generally uniform with an overall gradual decrease. Most interestingly, the two capacitors show opposite trends relative to one another in all three of the length directions. There are nearly identical opposite trends in every length 1 direction; when one capacitor increases, the other decreases.

Table 5.4 provides insights into initial parameters. Firstly, it is interesting to note that the initial series resistance for $R_0$ in sample 3 direction 2 is quite small. Secondly, the parallel initial parameters have similar patterns as Table 5.3 where in all three samples, the parallel resistors and capacitors all begin at approximately the same order of magnitude. The capacitors, $C_1$ and $C_2$, have the same order of magnitude pattern as the 0.5 wt.% CNF samples. The order of magnitude of the length 1 direction is one order smaller than the through-thickness 2 and 3 directions, at the same $10^{-12}$ F versus $10^{-11}$ F. Overall, this further bolsters the speculation of geometrically induced capacitive behavior for the through-thickness interrogations.

Finally, the 1.5 wt.% CNF-modified epoxy curve fits can be noted. The normalized circuit parameters versus cycle can be noted in Figure 5.17. The initial values outputted from the curve fitting process can be found tabulated in Table 5.5. It should be noted that the circuit successfully and accurately modeled the flip in the sample 3 length 1 direction after the 500$^{th}$ cycle as well as the sample 3 through-thickness 3 all-positive EIS curves.
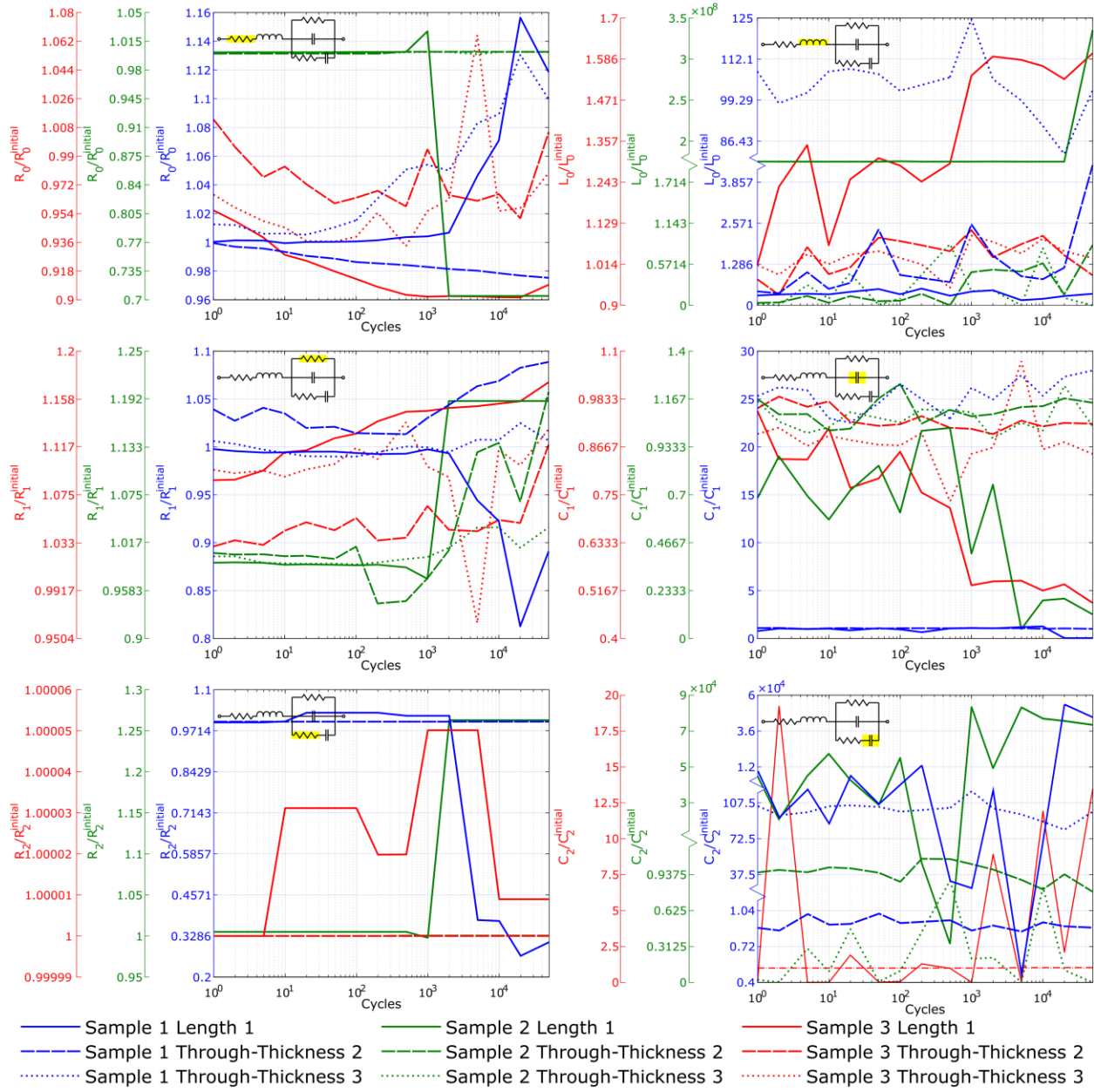
**Figure 5.18:** Normalized circuit parameters versus cycles for 1.5 wt.% CNF plotted beginning at cycle 1. Each of the six plots directly associates with the six circuit parameters.

**Table 5.5:** This table contains the initial circuit parameters that result from the curve fitting process. 1, 2, and 3 refer to the directions length 1, through-thickness 2, and through-thickness 3. These values serve as the initial values for the normalized data present in Figure 5.18.

|  |  | $R_0$ [$\Omega$] | $L_0$ [$H$] | $R_1$ [$\Omega$] | $C_1$ [$F$] | $R_2$ [$\Omega$] | $C_2$ [$F$] |
|---|---|---|---|---|---|---|---|
| Sample 1 | 1 | 382.4 | 6.819E-07 | 221.4 | 3.098E-11 | 47.42 | 7.326E-16 |
| | 2 | 204.3 | 2.959E-08 | 808.5 | 2.015E-11 | 808.1 | 6.293E-12 |
| | 3 | 156.7 | 4.345E-09 | 334.4 | 5.071E-13 | 225.2 | 3.057E-11 |
| Sample 2 | 1 | 576.1 | 3.228E-16 | 873.5 | 1.533E-11 | 819.5 | 7.335E-17 |
| | 2 | 210.8 | 1.973E-07 | 566.7 | 1.422E-11 | 384.6 | 1.491E-11 |
| | 3 | 261.4 | 9.173E-13 | 1,228 | 1.355E-11 | 1,222 | 4.753E-12 |
| Sample 3 | 1 | 294.2 | 6.927E-07 | 189.1 | 3.419E-11 | 12.26 | 7.544E-14 |
| | 2 | 184.2 | 8.393E-07 | 210.9 | 4.110E-11 | 26,810 | 0.08410 |
| | 3 | 140.0 | 1.026E-06 | 105.7 | 5.946E-11 | 10,800 | 0.01184 |

In Figure 5.18, the circuit parameters for the 1.5 wt.% CNF samples can be noted. First off, there is no real consistent trend present with any of the resistor values which is peculiar. For example, in about half the cases $R_0$ increases and in the other half it decreases. Of the resistors, $R_1$ is the most consistent with a general increase in its resistance. Furthermore, $R_2$ has almost no relative change except for in the length 1 directions for all three samples. In sample 1 it drops whereas in sample 2 it increases; in sample 3 there is almost no relative change noted by its *y*-axis. Note, at the 1,000[th] cycle, where the EIS flips from a negative imaginary part of impedance to a positive part, it reaches its relative maximum.

What is most interesting about the 1.5 wt.% CNF samples is the frequency-dependent circuit parameters. Where there had previously been no noteworthy trends there appears to be some agreement across samples. Firstly, the $L_0$ term shows an almost uniform increase in relative inductance for nearly all the samples. Sample 2 length 1 and sample 3 length 1 show the most notable changes. As well, sample 1 through-thickness 2 shows an increase. Furthermore, the capacitor $C_1$ shows agreement in all three samples. The length 1 directions all decrease as the samples near failure. Note the substantial drop in capacitance at the 1,000[th] cycle for sample 3; this is where the EIS plot flips. Overall, $C_2$ shows relative changes most notably in all three

length 1 directions, however, there is no agreement with how this parameter changes. For the 1.5 wt.% CNF samples, it seems frequency dependency plays more of a role.

Table 5.5 shows significant differences to the other initial parameters in Table 5.3 and Table 5.4. In all three samples, the parallel resistors all begin at relatively the same order of magnitude, however, the parallel capacitors now disagree. The inherent trend with length 1 capacitor values being orders-of-magnitude smaller than the through-thickness direction is only apparent for $C_2$. Note how the order of magnitude of $C_2$ in the length 1 direction is multiple orders smaller than the through-thickness 2 and 3 directions – about 5 orders smaller for samples 1 and 2 and 12 orders smaller for sample 3. The geometrically induced capacitive behavior is largely present in only the discontinuous conductive pathway of the material.

# 6. SUMMARY, CONCLUSION, AND FUTURE WORK

## 6.1 Summary

In summary, this thesis was motivated by the increasing role FRCs play in structural engineering due to their excellent specific properties. Fatigue damage progression in composite materials results from complex microstructural failures. Safety-critical composite structures benefit from robust SHM methodologies. Self-sensing materials via the piezoresistive effect have much potential for this. The piezoresistive effect in nanofiller-modified composite materials establishes a relationship between electrical properties and loading, deformation, and damage. Overwhelmingly, piezoresistive research has focused on DC resistance. This is an important limitation as self-sensing SHM has potential but these materials inherently possess AC characteristics. The lack of work to date on AC-focused study drives the need for this research.

GFRC with 0.5 wt.%, 1.0 wt.%, and 1.5 wt.% CNF-modified epoxy specimens were manufactured for tensile fatigue loading. An open-hole was drilled through the specimens to provide the materials with a stress concentration, i.e. a region of interest for damage development. Throughout the loading cycle, stiffness and complex impedance were monitored as the material fatigued. The specimens all showed initial stiffening followed by a gradual decrease in elastic modulus with increasing cycle.

AC impedance and phase were measured during pauses in the fatigue cycle. There were three electrode arrangements: across the length and through-the-thickness on either side of the hole. The DC response of the weight percentages showed that the 0.5 wt.% CNF samples relative resistance decrease with increasing damage. For the 1.0 wt.% and 1.5 wt.% CNF specimens, relative DC resistance increased with fatigue damage. The orders of magnitude show that with increasing weight fraction the resistance to DC flow gets minimized; more CNFs mean more pathways leading to less resistance.

The AC data was fit to an equivalent circuit. There was not a great deal of consistency across all of the samples. First, for the 0.5 wt.% CNF samples it seems in general resistance decreases with

increasing cycles. Next, with 1.0 wt.% CNF samples, resistance increases. With the 1.5 wt.% CNF samples some of the resistance values also increase. This agrees with the DC response of the materials. In the 0.5 wt.% and 1.0 wt.% CNF samples, there is no real trend in the frequency-dependent circuit parameters. In contrast, the 1.5 wt.% CNF samples show trends in the AC parameters; most notably the inductor increases in relative order. Most interesting is the initial capacitance values, which indicate that electrode geometry plays a role in how capacitance surmounts in the samples. When the electrodes are placed just opposite one another, representing a capacitor through the material, there is an increase in capacitance.

## 6.2    Conclusions

From this work, the following conclusions can be drawn. Fatigue loading has an effect on AC transport through the material. As well, a CNF-modified GFRC can be well described using the circuit presented in this experiment. Further, the trends in the circuit parameters are notable. There are trends in the resistor circuit parameters for the 0.5 wt.% and 1.0 wt.% CNF materials. There are some trends for the AC components in the 1.5 wt.% CNF samples. It is speculated that for higher weight fractions more obvious trends in the AC circuit parameters will develop. Presently, the overall results are too inconclusive to draw a definitive conclusion from the AC circuit versus cycle data. More fundamental work needs to be done into macroscale circuit-like behavior of these nanocomposites to extract efficacious information.

## 6.3    Future Work

In light of this work, there are multiple directions this methodology needs to be taken to further develop it for SHM. This work was limited in scope showing that different weight fractions play a role in how FRC fatigue damage develops, but the different regions need to be highlighted. As well, this thesis only developed the concept for GFRC nanofiller-modified materials, extending this to other material systems would show the promise of this methodology.

Nanofiller weight percentages play an important role in how the impedance data arises. Weight percentages affect both frequency independent and dependent circuit parameters. More study into 1.5 wt.% CNF samples and higher CNF weight fractions needs to be done to note how complex impedance goes from negative to positive in its imaginary component. Understanding

the microstructure changes is essential to establishing this methodology for SHM. Microscale modeling of the damage mechanisms is important to determine how macroscale circuit changes can be used to characterize material fatigue. Correlating damage progression with AE can further establish the fatigue mechanisms in these composite materials.

A final principle study to certify this SHM for all FRCs is to use carbon fiber instead of GF as the reinforcing phase. By using carbon fiber, nanofiller modifications do not need to be implemented into the polymer medium. Some work has been done investigating EIS changes as a function of different loading in carbon fiber reinforced composites [63] [64] [65] [66]. Abry et al. implemented equivalent circuit fitting and their model was a simplified parallel resistor-capacitor; they did show an increase in resistance and a decrease in capacitance as a function of flexural strain [65]. Tensile fatigue has been preliminarily studied by Slipher et al. where they looked at electrical impedance data in the cyclic loading of un-notched carbon fiber reinforced polymer. They used five AC interrogation directions. However, a limitation of their study is that they only had two successful samples [66].  Building off this preliminary research, a more established methodology can be developed to implement this SHM for aerospace and automotive industrial applications.

## APPENDIX A: RAW IMPEDANCE DATA

This appendix provides the raw impedance data that was obtained from the impedance analyzer. EIS plots provide the same information as these plots albeit in a different format. Each of the three interrogation directions is grouped per sample per figure. The most notable observation of the raw impedance data is that with increasing CNF weight fraction the phase shift occurs at a higher frequency.
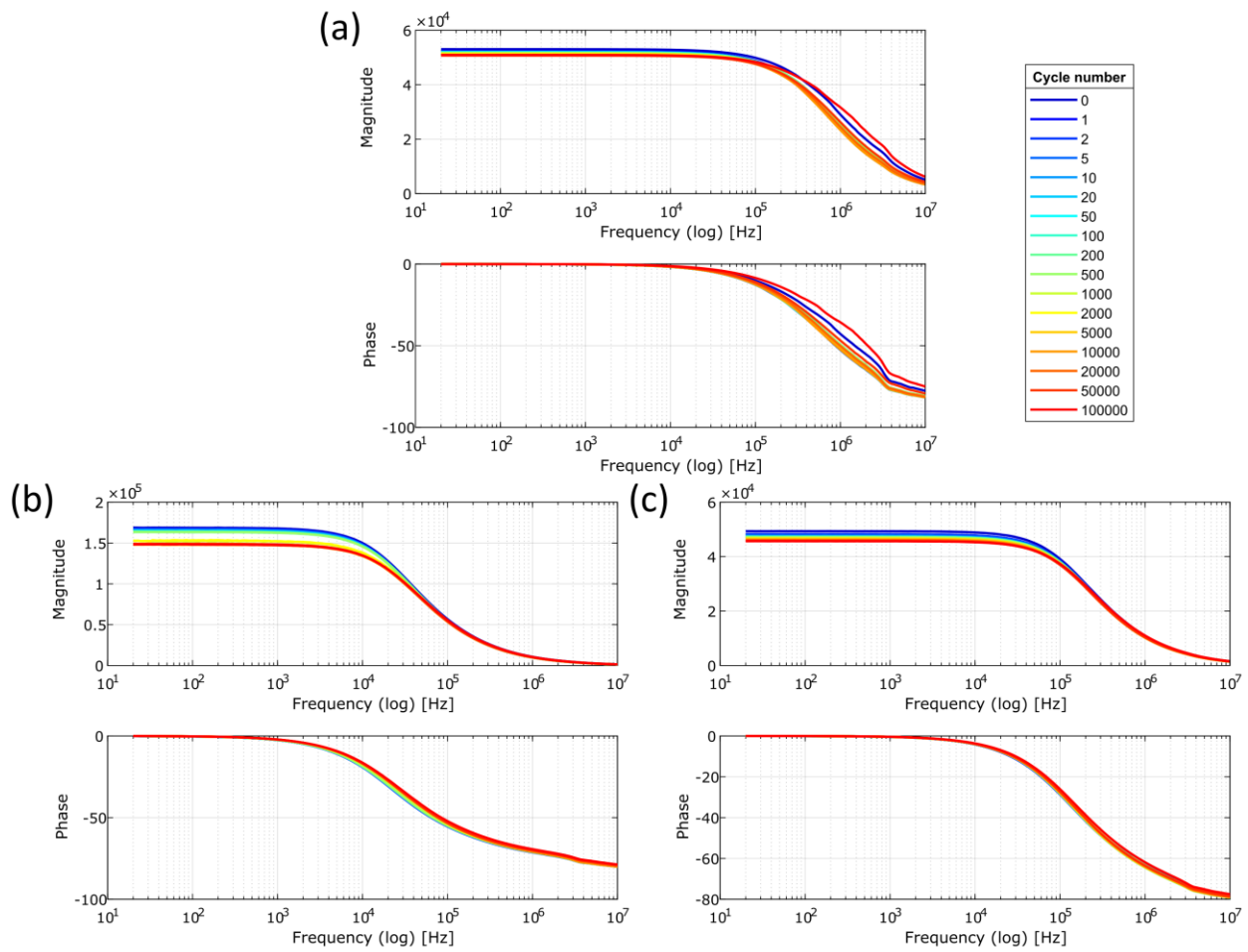


**Figure 0.1:** Raw impedance data for sample 1 of the 0.5 wt.% CNF-modified GFRC. Plot (a) shows the length 1 interrogation direction, plot (b) shows the through-thickness 2 interrogation direction, and plot (c) shows the through-thickness 3 interrogation direction.
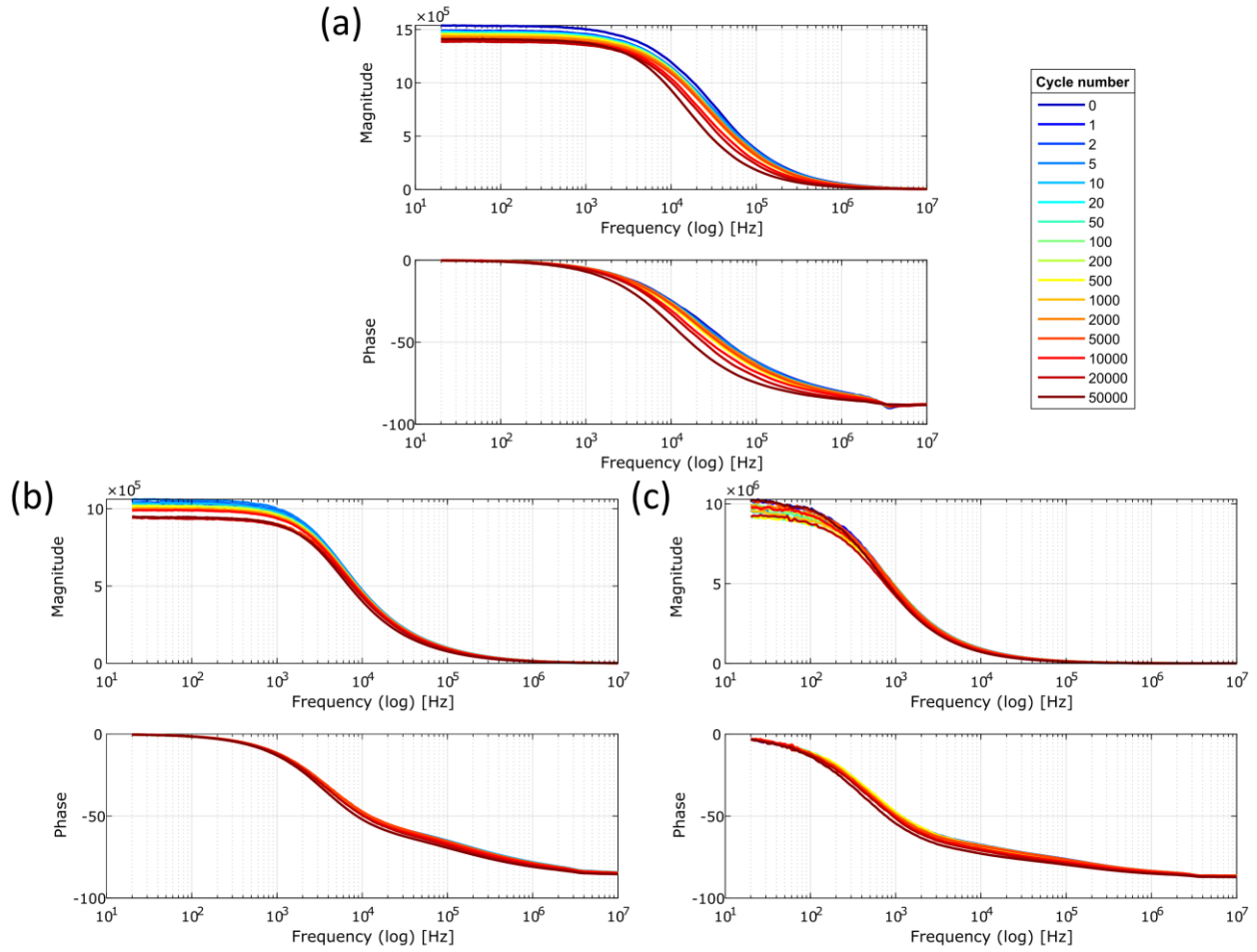
**Figure 0.2:** Raw impedance data for sample 2 of the 0.5 wt.% CNF-modified GFRC. Plot (a) shows the length 1 interrogation direction, plot (b) shows the through-thickness 2 interrogation direction, and plot (c) shows the through-thickness 3 interrogation direction.
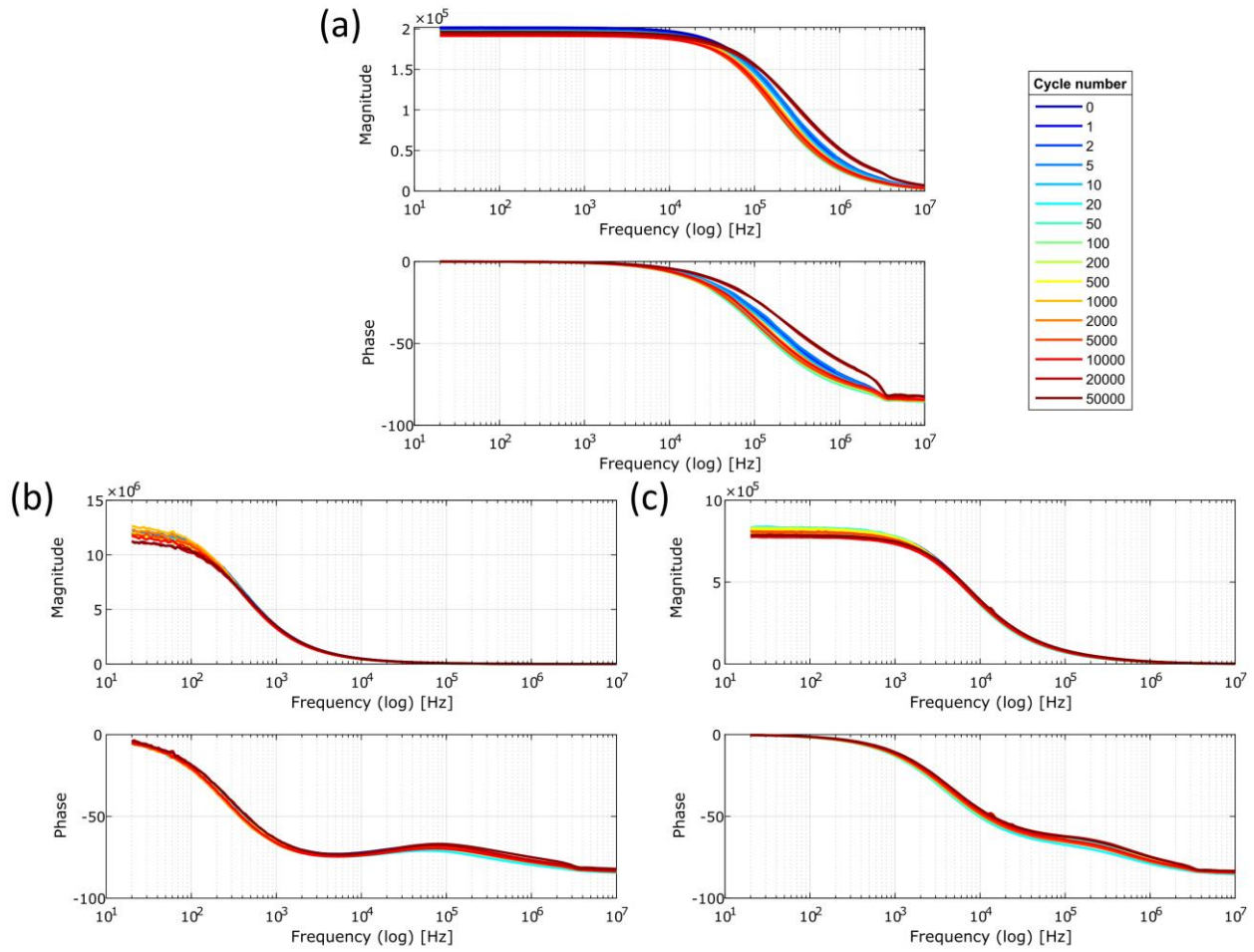
**Figure 0.3:** Raw impedance data for sample 3 of the 0.5 wt.% CNF-modified GFRC. Plot (a) shows the length 1 interrogation direction, plot (b) shows the through-thickness 2 interrogation direction, and plot (c) shows the through-thickness 3 interrogation direction.
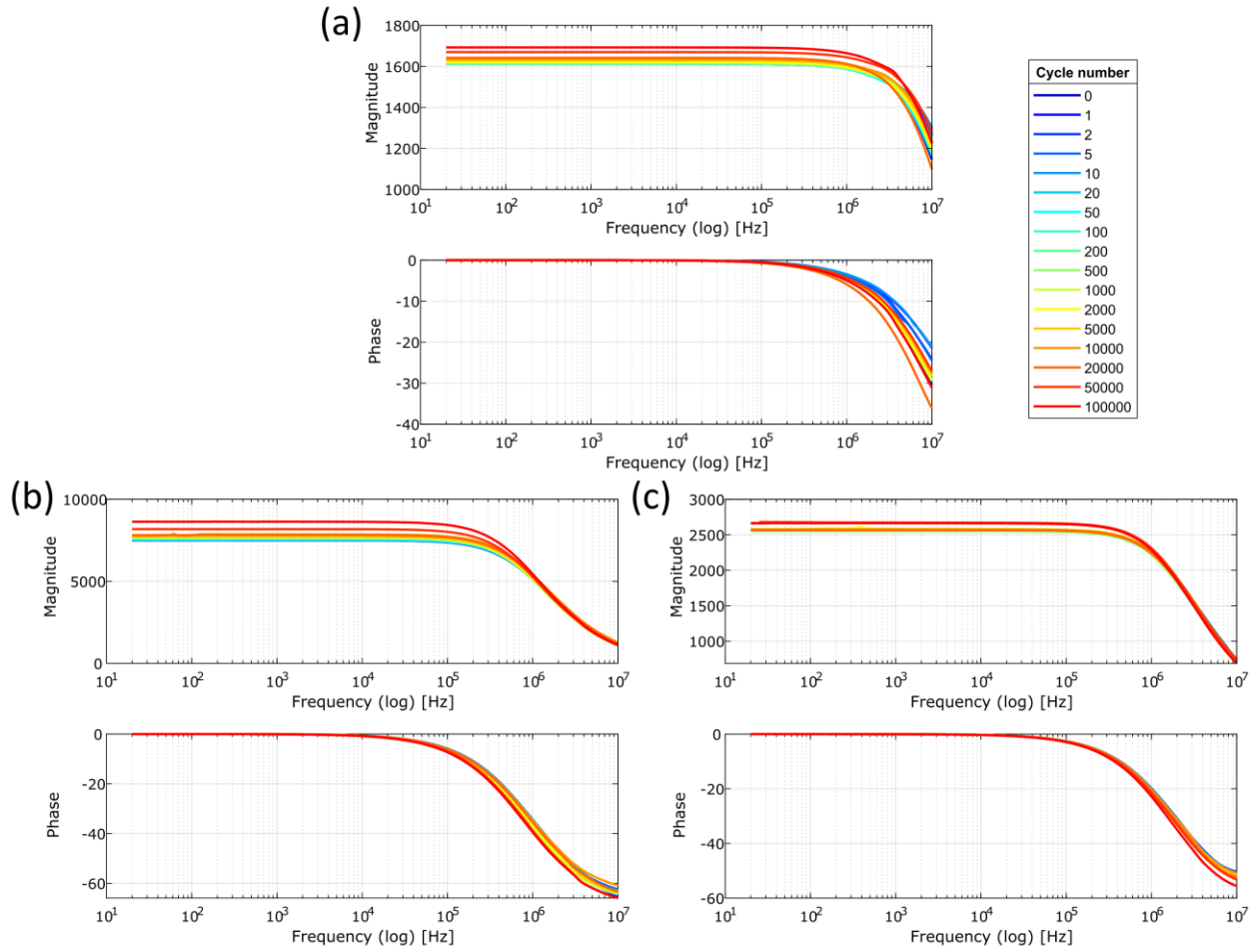
**Figure 0.4:** Raw impedance data for sample 1 of the 1.0 wt.% CNF-modified GFRC. Plot (a) shows the length 1 interrogation direction, plot (b) shows the through-thickness 2 interrogation direction, and plot (c) shows the through-thickness 3 interrogation direction.
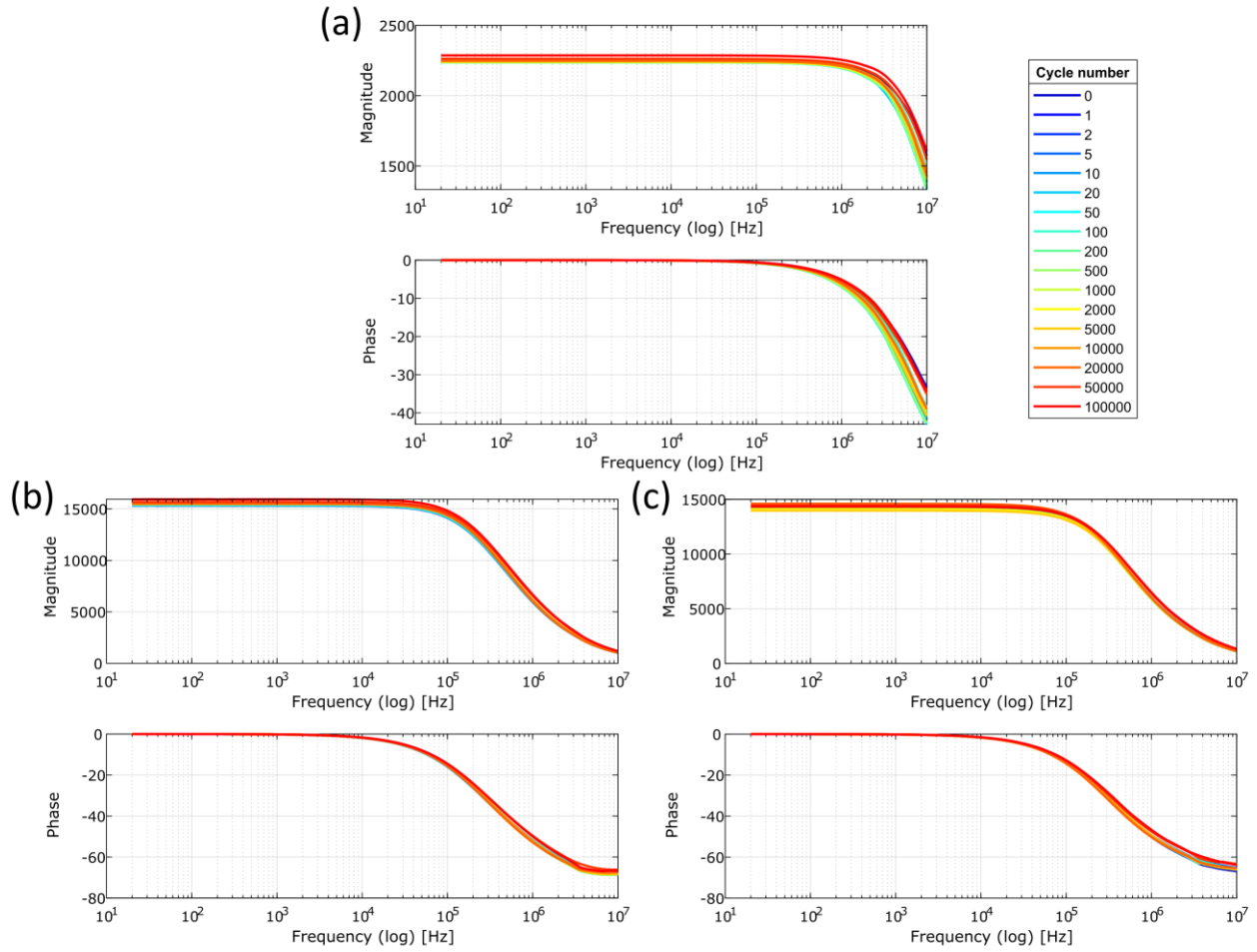
**Figure 0.5:** Raw impedance data for sample 2 of the 1.0 wt.% CNF-modified GFRC. Plot (a) shows the length 1 interrogation direction, plot (b) shows the through-thickness 2 interrogation direction, and plot (c) shows the through-thickness 3 interrogation direction.
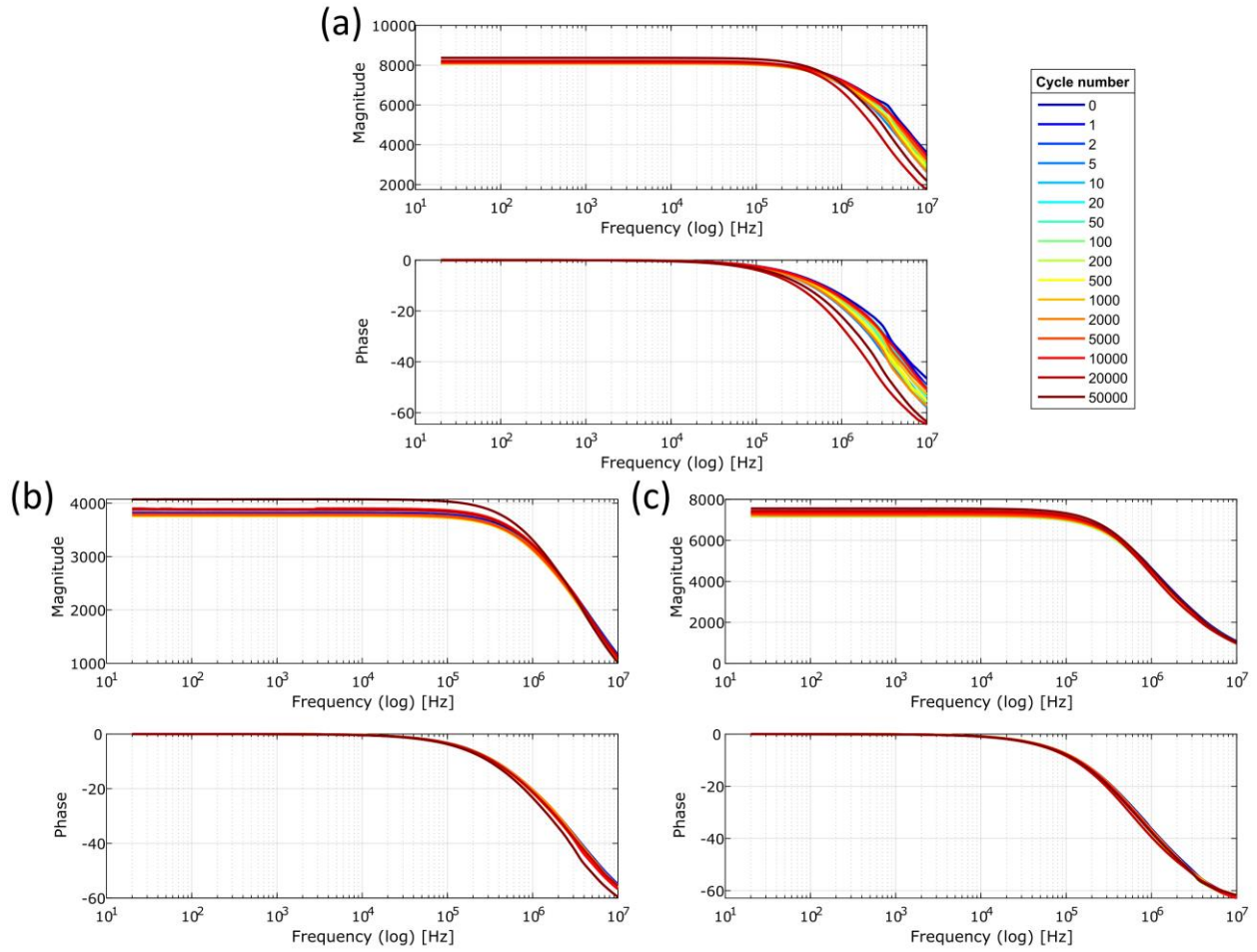
**Figure 0.6:** Raw impedance data for sample 3 of the 1.0 wt.% CNF-modified GFRC. Plot (a) shows the length 1 interrogation direction, plot (b) shows the through-thickness 2 interrogation direction, and plot (c) shows the through-thickness 3 interrogation direction.
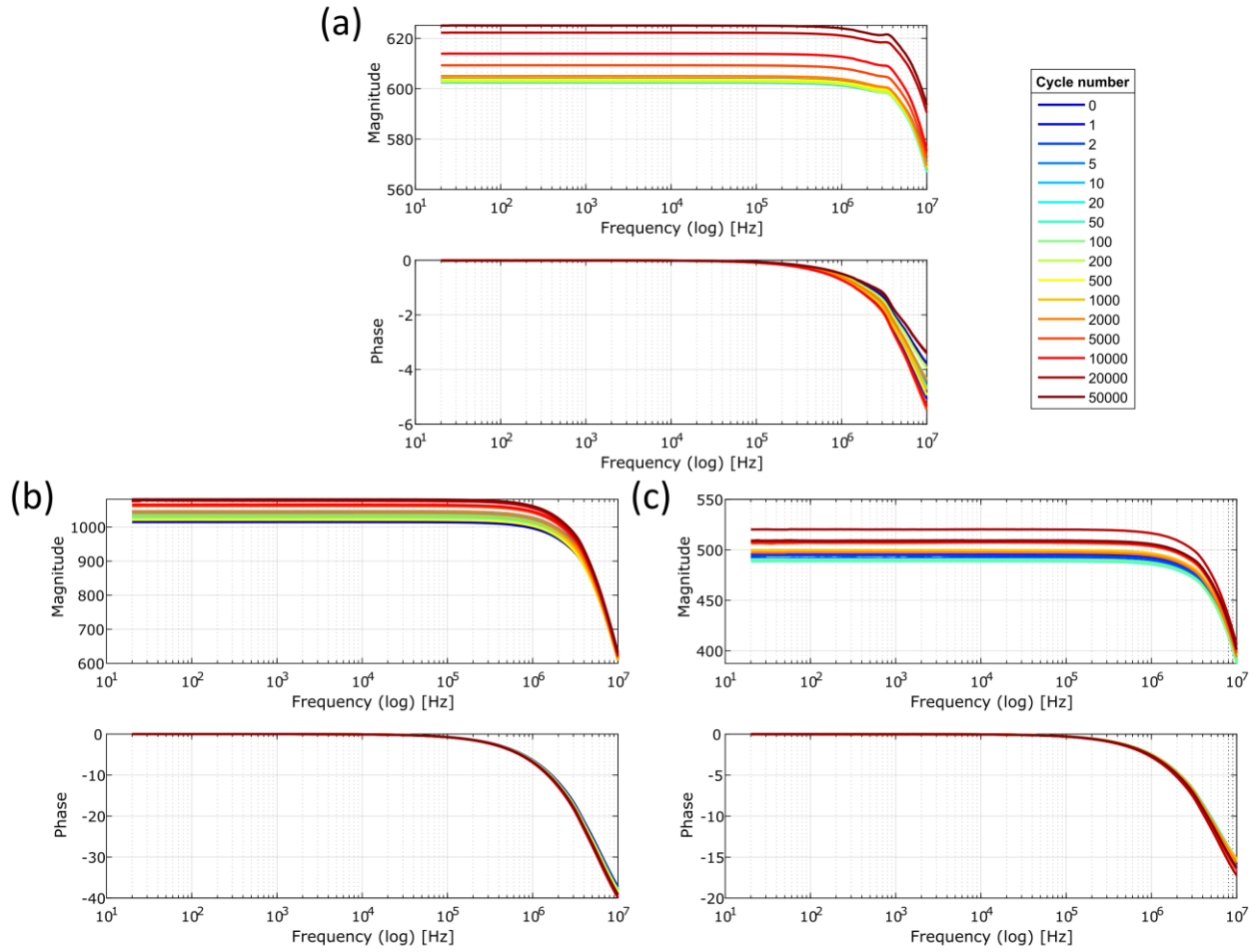
**Figure 0.7:** Raw impedance data for sample 1 of the 1.5 wt.% CNF-modified GFRC. Plot (a) shows the length 1 interrogation direction, plot (b) shows the through-thickness 2 interrogation direction, and plot (c) shows the through-thickness 3 interrogation direction.

**Figure 0.8:** Raw impedance data for sample 2 of the 1.5 wt.% CNF-modified GFRC. Plot (a) shows the length 1 interrogation direction, plot (b) shows the through-thickness 2 interrogation direction, and plot (c) shows the through-thickness 3 interrogation direction.

**Figure 0.9:** Raw impedance data for sample 3 of the 1.5 wt.% CNF-modified GFRC. Plot (a) shows the length 1 interrogation direction, plot (b) shows the through-thickness 2 interrogation direction, and plot (c) shows the through-thickness 3 interrogation direction.
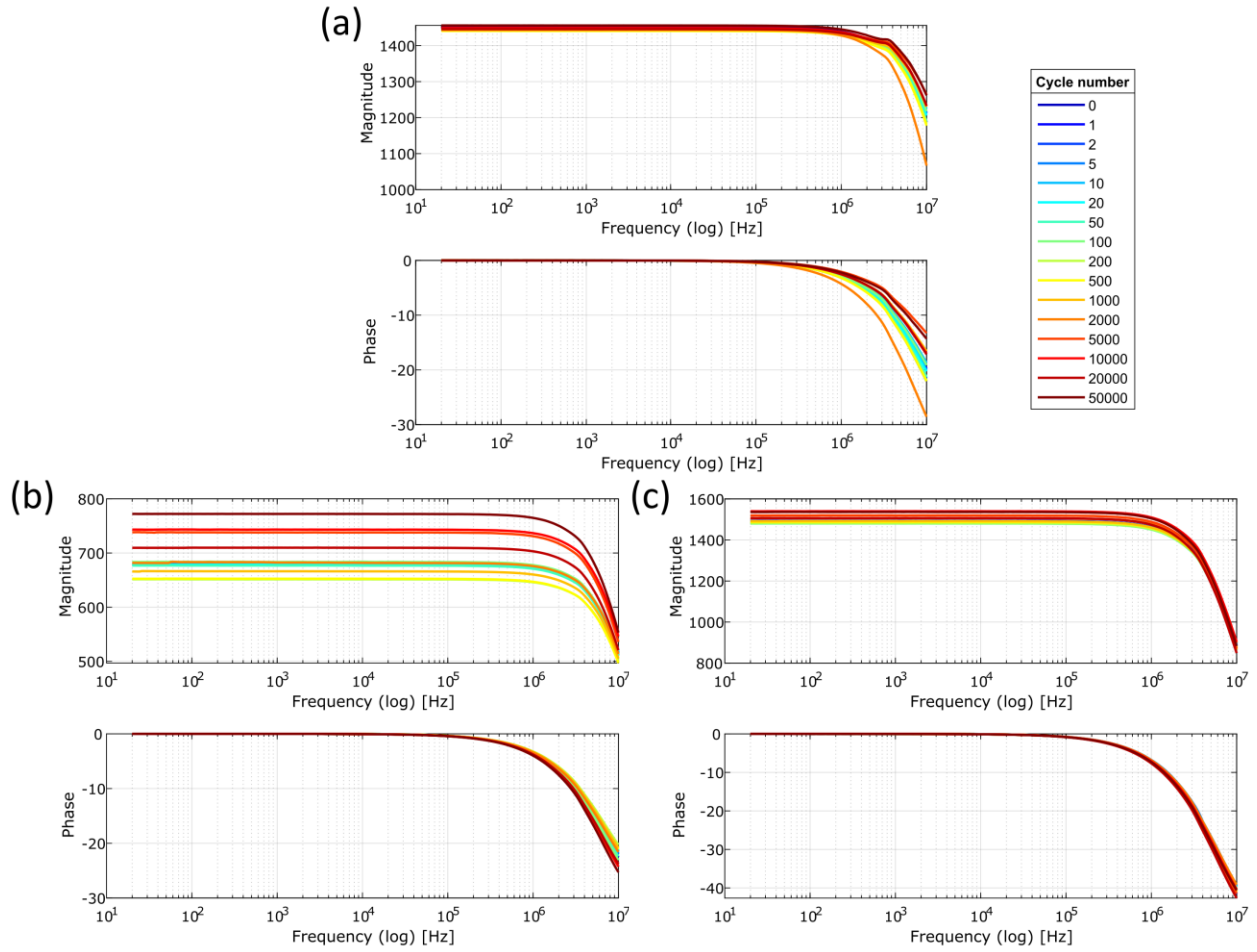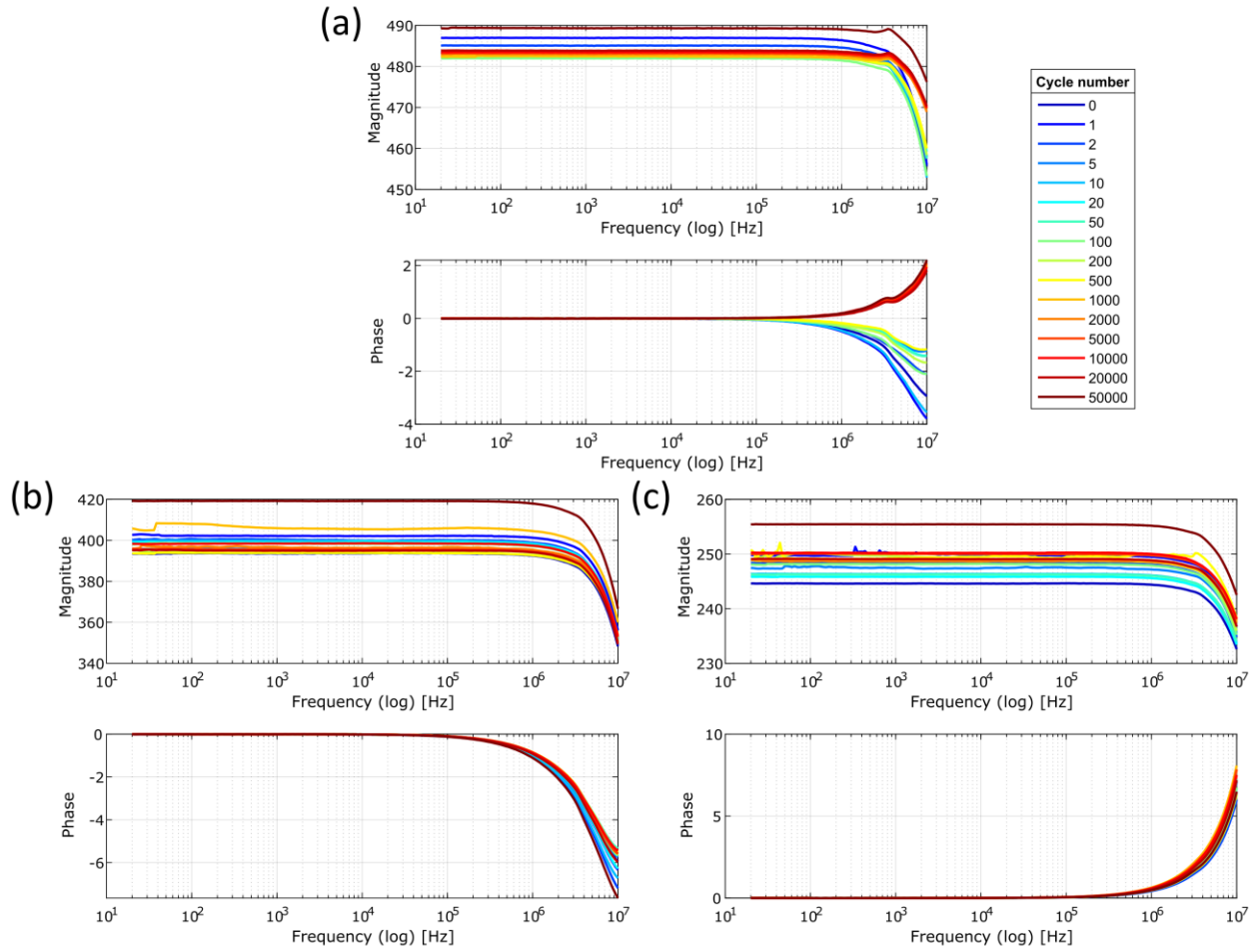
# REFERENCES

[1] V. Giurgiutiu, *Structural health monitoring of aerospace composites*. Academic Press, 2015.

[2] C. Sun, "Mechanics of Composite Materials and Laminates: Lecture Notes for A&AE 555," *Lecture Notes]. Department of Aeronautics and Astronautics. Purdue University, West Lafayette, IN*, 2001.

[3] L. A. Carlsson, D. F. Adams, and R. B. Pipes, *Experimental characterization of advanced composite materials*. CRC press, 2014.

[4] W. W. Stinchcomb and C. E. Bakis, "Fatigue behavior of composite laminates," in *Composite materials series*, vol. 4, Elsevier, 1991, pp. 105–180.

[5] "Carbon Fiber vs. Glass Fiber - Oribi." https://oribimanufacturing.com/knowledge-base-post/carbon-fiber-101-3/ (accessed Apr. 04, 2020).

[6] S. Giancane, F. Panella, R. Nobile, and V. Dattoma, "Fatigue damage evolution of fiber reinforced composites with digital image correlation analysis," *Procedia Engineering*, vol. 2, no. 1, pp. 1307–1315, 2010.

[7] H. Hahn and R. Y. Kim, "Fatigue behavior of composite laminate," *Journal of Composite Materials*, vol. 10, no. 2, pp. 156–180, 1976.

[8] R. Talreja, "Fatigue of composite materials: damage mechanisms and fatigue-life diagrams," *Proceedings of the Royal Society of London. A. Mathematical and Physical Sciences*, vol. 378, no. 1775, pp. 461–475, 1981.

[9] A. F. Grandt Jr, *Fundamentals of structural integrity: damage tolerant design and nondestructive evaluation*. John Wiley & Sons, 2003.

[10] S. C. Garcea, S. M. Spearing, and I. Sinclair, "Exploring the Fundamental of Fatigue in Composites: Opportunities using X-Ray Computed Tomography Imaging," SOUTHAMPTON UNIV (UNITED KINGDOM), 2012.

[11] R. Harrison and M. Bader, "Damage development in CFRP laminates under monotonic and cyclic stressing," *Fibre Science and Technology*, vol. 18, no. 3, pp. 163–180, 1983.

[12] H. Daken and J. Mar, "Splitting initiation and propagation in notched unidirectional graphite/epoxy composites under tension-tension cyclic loading," *Composite structures*, vol. 4, no. 2, pp. 111–133, 1985.

[13] X. Qing, A. Kumar, C. Zhang, I. F. Gonzalez, G. Guo, and F.-K. Chang, "A hybrid piezoelectric/fiber optic diagnostic system for structural health monitoring," *Smart Materials and Structures*, vol. 14, no. 3, p. S98, 2005.

[14] D. Adams, *Health monitoring of structural materials and components: methods with applications*. John Wiley & Sons, 2007.

[15] B. Glisic and D. Inaudi, *Fibre optic methods for structural health monitoring*. John Wiley & Sons, 2008.

[16] V. Giurgiutiu and G. Santoni-Bottai, "Structural health monitoring of composite structures with piezoelectric-wafer active sensors," *AIAA journal*, vol. 49, no. 3, pp. 565–581, 2011.

[17] A. Baker, N. Rajic, and C. Davis, "Towards a practical structural health monitoring technology for patched cracks in aircraft structure," *Composites Part A: applied science and manufacturing*, vol. 40, no. 9, pp. 1340–1352, 2009.

[18] V. Giurgiutiu and C. Soutis, "Enhanced composites integrity through structural health monitoring," *Applied Composite Materials*, vol. 19, no. 5, pp. 813–829, 2012.

[19] T. Dong and N. H. Kim, "Cost-Effectiveness of Structural Health Monitoring in Fuselage Maintenance of the Civil Aviation Industry," *Aerospace*, vol. 5, no. 3, p. 87, 2018.

[20] M. B. Rao, M. Bhat, C. Murthy, K. V. Madhav, and S. Asokan, "Structural health monitoring (SHM) using strain gauges, PVDF film and fiber bragg grating (FBG) sensors: A comparative study," presented at the National Seminar on Non-Destructive Evaluation, NDE 2006, 2006.

[21] S. Takeda, Y. Aoki, T. Ishikawa, N. Takeda, and H. Kikukawa, "Structural health monitoring of composite wing structure during durability test," *Composite structures*, vol. 79, no. 1, pp. 133–139, 2007.

[22] A. Thomas, J. Kim, T. Tallman, and C. Bakis, "Damage detection in self-sensing composite tubes via electrical impedance tomography," *Composites Part B: Engineering*, vol. 177, p. 107276, 2019.

[23] I. Burmistrov *et al.*, "Improvement of carbon black based polymer composite electrical conductivity with additions of MWCNT," *Composites Science and Technology*, vol. 129, pp. 79–85, 2016.

[24] D. Pedrazzoli, A. Dorigato, and A. Pegoretti, "Monitoring the mechanical behavior under ramp and creep conditions of electrically conductive polymer composites," *Composites Part A: Applied Science and Manufacturing*, vol. 43, no. 8, pp. 1285–1292, 2012.

[25] T. N. Tallman, S. Gungor, K. Wang, and C. E. Bakis, "Damage detection via electrical impedance tomography in glass fiber/epoxy laminates with carbon black filler," *Structural Health Monitoring*, vol. 14, no. 1, pp. 100–109, 2015.

[26] D. Baltzis *et al.*, "Multi-scaled carbon reinforcements in ternary epoxy composite materials: Dispersion and electrical impedance study," *Composites Science and Technology*, vol. 153, pp. 7–17, 2017.

[27] C. Viets, S. Kaysser, and K. Schulte, "Damage mapping of GFRP via electrical resistance measurements using nanocomposite epoxy matrix systems," *Composites Part B: Engineering*, vol. 65, pp. 80–88, 2014.

[28] T. N. Tallman and H. Hassan, "A computational exploration of the effect of alignment and aspect ratio on alternating current conductivity in carbon nanofiber–modified epoxy," *Journal of Intelligent Material Systems and Structures*, p. 1045389X19898252, 2020.

[29] T. Tallman, S. Gungor, K. Wang, and C. E. Bakis, "Tactile imaging and distributed strain sensing in highly flexible carbon nanofiber/polyurethane nanocomposites," *Carbon*, vol. 95, pp. 485–493, 2015.

[30] T. Tallman, S. Gungor, K. Wang, and C. E. Bakis, "Damage detection and conductivity evolution in carbon nanofiber epoxy via electrical impedance tomography," *Smart Materials and Structures*, vol. 23, no. 4, p. 045034, 2014.

[31] D. Bekas and A. Paipetis, "Damage monitoring in nanoenhanced composites using impedance spectroscopy," *Composites Science and Technology*, vol. 134, pp. 96–105, 2016.

[32] M. Saafi *et al.*, "Multifunctional properties of carbon nanotube/fly ash geopolymeric nanocomposites," *Construction and Building Materials*, vol. 49, pp. 46–55, 2013.

[33] A. Sanli and O. Kanoun, "Electrical impedance analysis of carbon nanotube/epoxy nanocomposite-based piezoresistive strain sensors under uniaxial cyclic static tensile loading," *Journal of Composite Materials*, vol. 54, no. 6, pp. 845–855, 2020.

[34] S. Nag-Chowdhury, H. Bellégou, I. Pillin, M. Castro, P. Longrais, and J.-F. Feller, "Interfacial nanocomposite sensors (sQRS) for the core monitoring of polymer composites' fatigue and damage analysis," *Nanocomposites*, vol. 4, no. 3, pp. 69–79, 2018.

[35] D. G. Bekas and A. S. Paipetis, "Study of the effect of damage on the electrical impedance of carbon nanotube reinforced epoxy nanocomposites," *Journal of Sensors*, vol. 2015, 2015.

[36] A. Sanli, J. J. Kurian, C. Müller, and O. Kanoun, "Tuning the fabrication parameters of multi-walled carbon nanotubes-epoxy based flexible strain sensitive composites," presented at the 2016 IEEE International Instrumentation and Measurement Technology Conference Proceedings, 2016, pp. 1–5.

[37] K. J. Loh, J. P. Lynch, B. Shim, and N. Kotov, "Tailoring piezoresistive sensitivity of multilayer carbon nanotube composite strain sensors," *Journal of Intelligent Material Systems and Structures*, vol. 19, no. 7, pp. 747–764, 2008.

[38] A. Sanli, C. Müller, O. Kanoun, C. Elibol, and M. F.-X. Wagner, "Piezoresistive characterization of multi-walled carbon nanotube-epoxy based flexible strain sensitive films by impedance spectroscopy," *Composites Science and Technology*, vol. 122, pp. 18–26, 2016.

[39] M. Nofar, S. Hoa, and M. Pugh, "Failure detection and monitoring in polymer matrix composites subjected to static and dynamic loads using carbon nanotube networks," *Composites Science and Technology*, vol. 69, no. 10, pp. 1599–1606, 2009.

[40] J. de J. Ku-Herrera, V. La Saponara, and F. Avilés, "Selective damage sensing in multiscale hierarchical composites by tailoring the location of carbon nanotubes," *Journal of Intelligent Material Systems and Structures*, vol. 29, no. 4, pp. 553–562, 2018.

[41] L. Gao, E. T. Thostenson, Z. Zhang, and T. Chou, "Sensing of damage mechanisms in fiber-reinforced composites under cyclic loading using carbon nanotubes," *Advanced functional materials*, vol. 19, no. 1, pp. 123–130, 2009.

[42] Q. An, S. Tamrakar, J. W. Gillespie Jr, A. N. Rider, and E. T. Thostenson, "Tailored glass fiber interphases via electrophoretic deposition of carbon nanotubes: Fiber and interphase characterization," *Composites Science and Technology*, vol. 166, pp. 131–139, 2018.

[43] Q. An, A. N. Rider, and E. T. Thostenson, "Electrophoretic deposition of carbon nanotubes onto carbon-fiber fabric for production of carbon/epoxy composites with improved mechanical properties," *Carbon*, vol. 50, no. 11, pp. 4130–4143, 2012.

[44] B. R. Loyola, Y. Zhao, K. J. Loh, and V. La Saponara, "The electrical response of carbon nanotube-based thin film sensors subjected to mechanical and environmental effects," *Smart materials and structures*, vol. 22, no. 2, p. 025010, 2012.

[45] Q. Zhao, M. D. Frogley, and H. D. Wagner, "The use of carbon nanotubes to sense matrix stresses around a single glass fiber," *Composites science and technology*, vol. 61, no. 14, pp. 2139–2143, 2001.

[46] P. Bertasius *et al.*, "Fine Tuning of Electrical Transport and Dielectric Properties of Epoxy/Carbon Nanotubes Composites via Magnesium Oxide Additives," *Polymers*, vol. 11, no. 12, p. 2044, 2019.

[47] T. Tallman and K. Wang, "An arbitrary strains carbon nanotube composite piezoresistivity model for finite element integration," *Applied Physics Letters*, vol. 102, no. 1, p. 011909, 2013.

[48] J. G. Simmons, "Generalized formula for the electric tunnel effect between similar electrodes separated by a thin insulating film," *Journal of applied physics*, vol. 34, no. 6, pp. 1793–1803, 1963.

[49] T. Tallman and K. Wang, "The influence of nanofiller alignment on transverse percolation and conductivity," *Nanotechnology*, vol. 26, no. 2, p. 025501, 2014.

[50] H. Hassan, F. Semperlotti, K.-W. Wang, and T. N. Tallman, "Enhanced imaging of piezoresistive nanocomposites through the incorporation of nonlocal conductivity changes in electrical impedance tomography," *Journal of Intelligent Material Systems and Structures*, vol. 29, no. 9, pp. 1850–1861, 2018.

[51] A. Naghashpour and S. Van Hoa, "A technique for real-time detection, location and quantification of damage in large polymer composite structures made of electrically non-conductive fibers and carbon nanotube networks," *Nanotechnology*, vol. 24, no. 45, p. 455502, 2013.

[52] L. Böger, M. H. Wichmann, L. O. Meyer, and K. Schulte, "Load and health monitoring in glass fibre reinforced composites with an electrically conductive nanocomposite epoxy matrix," *Composites Science and Technology*, vol. 68, no. 7–8, pp. 1886–1894, 2008.

[53] T. Tallman, "Damage Detection in Nanofiller-Modified Composites With External Circuitry via Resonant Frequency Shifts," presented at the ASME 2018 Conference on Smart Materials, Adaptive Structures and Intelligent Systems, 2018.

[54] C. Tsonos, "Comments on frequency dependent AC conductivity in polymeric materials at low frequency regime," *Current Applied Physics*, vol. 19, no. 4, pp. 491–497, 2019.

[55] R. Nave, "Complex Impedance," *HyperPhysics*, Mar. 28, 2020. http://hyperphysics.phy-astr.gsu.edu/hbase/electric/impcom.html (accessed Mar. 28, 2020).

[56] B. R. Loyola, V. La Saponara, and K. J. Loh, "In situ strain monitoring of fiber-reinforced polymers using embedded piezoresistive nanocomposites," *Journal of materials science*, vol. 45, no. 24, pp. 6786–6798, 2010.

[57] G. Song, "Equivalent circuit model for AC electrochemical impedance spectroscopy of concrete," *Cement and concrete research*, vol. 30, no. 11, pp. 1723–1730, 2000.

[58] P. J. Burke, "An RF circuit model for carbon nanotubes," *IEEE Transactions on Nanotechnology*, vol. 2, no. 1, pp. 55–58, 2003.

[59] H. Li, W.-Y. Yin, K. Banerjee, and J.-F. Mao, "Circuit modeling and performance analysis of multi-walled carbon nanotube interconnects," *IEEE Transactions on electron devices*, vol. 55, no. 6, pp. 1328–1337, 2008.

[60] P. D. Fazzino, K. L. Reifsnider, and P. Majumdar, "Impedance spectroscopy for progressive damage analysis in woven composites," *Composites Science and Technology*, vol. 69, no. 11–12, pp. 2008–2014, 2009.

[61] H. Hassan and T. N. Tallman, "Failure prediction in self-sensing nanocomposites via genetic algorithm-enabled piezoresistive inversion," *Structural Health Monitoring*, p. 1475921719863062, 2019.

[62] O. Nixon-Pearson, S. Hallett, P. Withers, and J. Rouse, "Damage development in open-hole composite specimens in fatigue. Part 1: Experimental investigation," *Composite Structures*, vol. 106, pp. 882–889, 2013.

[63] K. Almuhammadi, T. K. Bera, and G. Lubineau, "Electrical impedance spectroscopy for measuring the impedance response of carbon-fiber-reinforced polymer composite laminates," *Composite Structures*, vol. 168, pp. 510–521, 2017.

[64] T. K. Bera *et al.*, "Electrical impedance spectroscopy for electro-mechanical characterization of conductive fabrics," *Sensors*, vol. 14, no. 6, pp. 9738–9754, 2014.

[65] J. Abry, Y. Choi, A. Chateauminois, B. Dalloz, G. Giraud, and M. Salvia, "In-situ monitoring of damage in CFRP laminates by means of AC and DC measurements," *Composites Science and Technology*, vol. 61, no. 6, pp. 855–864, 2001.

[66] G. A. Slipher, R. A. Haynes, and J. C. Riddick, "Electrical impedance spectroscopy for structural health monitoring," in *Experimental and Applied Mechanics, Volume 6*, Springer, 2015, pp. 1–11.